

**Polyvinylidene Fluoride -Based MEMS Tactile Sensor for  
Minimally Invasive Surgery**

**Mohammad Ameen Yousef Qasaimeh**

A Thesis

In

The Department

of

Mechanical and Industrial Engineering

Presented in Partial Fulfillment of the Requirements

For the Degree of Master of Applied Science (Mechanical Engineering) at

Concordia University

Montreal, Quebec, Canada.

November, 2007

© Mohammad Ameen Qasaimeh, 2007



Library and  
Archives Canada

Published Heritage  
Branch

395 Wellington Street  
Ottawa ON K1A 0N4  
Canada

Bibliothèque et  
Archives Canada

Direction du  
Patrimoine de l'édition

395, rue Wellington  
Ottawa ON K1A 0N4  
Canada

*Your file* *Votre référence*  
*ISBN: 978-0-494-40920-6*  
*Our file* *Notre référence*  
*ISBN: 978-0-494-40920-6*

**NOTICE:**

The author has granted a non-exclusive license allowing Library and Archives Canada to reproduce, publish, archive, preserve, conserve, communicate to the public by telecommunication or on the Internet, loan, distribute and sell theses worldwide, for commercial or non-commercial purposes, in microform, paper, electronic and/or any other formats.

The author retains copyright ownership and moral rights in this thesis. Neither the thesis nor substantial extracts from it may be printed or otherwise reproduced without the author's permission.

**AVIS:**

L'auteur a accordé une licence non exclusive permettant à la Bibliothèque et Archives Canada de reproduire, publier, archiver, sauvegarder, conserver, transmettre au public par télécommunication ou par l'Internet, prêter, distribuer et vendre des thèses partout dans le monde, à des fins commerciales ou autres, sur support microforme, papier, électronique et/ou autres formats.

L'auteur conserve la propriété du droit d'auteur et des droits moraux qui protègent cette thèse. Ni la thèse ni des extraits substantiels de celle-ci ne doivent être imprimés ou autrement reproduits sans son autorisation.

---

In compliance with the Canadian Privacy Act some supporting forms may have been removed from this thesis.

Conformément à la loi canadienne sur la protection de la vie privée, quelques formulaires secondaires ont été enlevés de cette thèse.

While these forms may be included in the document page count, their removal does not represent any loss of content from the thesis.

Bien que ces formulaires aient inclus dans la pagination, il n'y aura aucun contenu manquant.

■ ■ ■  
**Canada**

## **ABSTRACT**

# **Polyvinylidene Fluoride -Based MEMS Tactile Sensor for Minimally Invasive Surgery**

**Mohammad Ameen Qasaimeh**

Minimally invasive surgery (MIS) procedures have been growing rapidly for the past couple of decades. In MIS operations, endoscopic tools are inserted through a small incision on human's body. Although these procedures have many advantages such as fast recovery time, minimum damage to human body and reduced post operative complications, it does not provide any tactile feedback to the surgeon.

This thesis reports on design, finite element analysis, fabrication and testing of a micromachined piezoelectric endoscopic tactile sensor. Similar to the commercial endoscopic graspers, the sensor is teeth like in order to grasp slippery tissues. It consists of three layers; the first layer is a silicon layer of teeth shapes on the top and two supports at the bottom forming a thin plate and a U-Channel. The second layer is a patterned Polyvinylidene Fluoride (PVDF) film, and the third layer is a supporting Plexiglas. The patterned PVDF film was placed on the middle between the other two layers. When a concentric load is applied to the sensor, the magnitude and the position of the applied load are obtained from the outputs of the sensing elements which are sandwiched between the silicon supports and the Plexiglas. In addition, when a soft object/tissue is place on the sensor and load is applied the degree of the softness/compliance of the object

is obtained from the outputs from the middle PVDF sensing elements, which are glued to the back of the thin silicon plate. The outputs are related to the deformation of the silicon plate which related to the contacting object softness.

The sensor has high sensitivity and high dynamic range as a result it can potentially detect a small dynamic load such as a pulse load as well as a high load such as a firm grasping of a tissue by an endoscopic grasper. The entire surface of the tactile sensor is also active, which is an advantage in detecting the precise position of the applied point load on the grasper. The finite element analysis and experimental results are in close agreement with each other. The sensor can potentially be integrated with the gasper of a commercially available endoscopic grasper.

**Dedicated to My Parents**

## **ACKNOWLEDGEMENT**

My great thanks go to Almighty Allah (God), whom I submit my continuous gratitude, and hope to be accepted.

I wish to thank my supervisors for their invaluable support, time, patience and the smooth guidance. In addition, I would like to acknowledge NSERC, and the Faculty of Engineering and Computer Science for their financial supports.

My great love and warm feelings are submitted to my parents; who are my source of love, strength, and the deep vision. I need to spend hundreds of years to award them.

To the spirits of my late grandfather and my late aunt; who left quickly while I was pursuing my research on this thesis. They were the warm source of love, smile, and the gentle encouragement. May god bless both of them and make them home on Paradise.

My virtual love is conveyed to my entire family members in Jordan and Canada; who supported me during hard times, and shared me the fun times with big smile. Moreover, my special appreciation expressed to all of my friends in Jordan and Montreal. Without whom, I was not able to carry on. Thanks for the pleasant time we had, and for the continuing help and supports.

I have been lucky to join the research groups of tactile sensing and medical robotics laboratory, and MEMS and NanoDevices laboratory. I would like to express my sincere feelings to the all members of both groups for their enjoyable time and friendly assistants.

# TABLE OF CONTENTS

<b>LIST OF FIGURES</b>	<b>XII</b>
<b>LIST OF TABLES</b>	<b>XIX</b>
<b>SYMBOLS</b>	<b>XX</b>
<b>CHAPTER 1 - INTRODUCTION AND LITERATURE REVIEW</b>	<b>1</b>
1.1 MINIMALLY INVASIVE SURGERY .....	2
1.2 TACTILE SENSING .....	5
1.3 MICRO-ELECTRO-MECHANICAL SYSTEMS (MEMS) .....	8
1.4 MEMS MICROFABRICATION TECHNIQUES .....	11
1.4.1 Surface Micromachining	11
1.4.2 Bulk Micromachining	12
1.4.3 Silicon Wafers	13
1.4.4 Photolithography Process	14
1.5 TACTILE SENSOR TECHNOLOGIES .....	16
1.5.1 Optical Sensors	16
1.5.2 Strain Gauge Sensors	17
1.5.3 Capacitive Sensors	18
1.5.4 Magnetic Based Sensor	19
1.5.5 Piezoelectric Sensors	20
1.5.6 Comparison among the Different Technologies	21
1.6 LITERATURE REVIEW .....	22
1.7 OBJECTIVES AND SCOPE OF THIS RESEARCH.....	30

<b>CHAPTER 2 – SENSOR DESIGN</b>	<b>33</b>
2.1 TOOTH-LIKE SILICON LAYER .....	33
2.2 SENSING ELEMENTS .....	36
2.3 THE SENSOR ASSEMBLY .....	39
2.4 CLOSED FORM ANALYSIS OF THE SENSOR.....	40
2.4.1 Sensing Elements at Supports	41
2.4.2 Sensing Elements at Middle	43
2.5 SUMMARY .....	52
 <b>CHAPTER 3 – FINITE ELEMENT ANALYSIS OF THE SENSOR</b>	 <b>53</b>
3.1 SENSOR MODELING .....	53
3.2 PARAMETRICAL ANALYSIS .....	56
3.3 GEOMETRICAL ANALYSIS OF THE SENSOR.....	61
3.3.1 Teeth Arrangements	62
3.3.2 Sensing Elements Arrangements	66
3.4 HIDDEN FEATURES INSIDE GRASPED OBJECTS.....	70
3.5 SENSOR SIMULATIONS.....	74
3.4.1 Point Load at the Center	77
3.4.2 Point Load in XY Plan	79
3.4.2.1 Point Load Moves Along Y-Direction	80
3.4.2.2 Point Load Moves Along the X-Direction	83
3.4.3 Contacting Object and a Distributed Load	87
3.5 SUMMARY .....	92
 <b>CHAPTER 4 – SENSOR MICROFABRICATIONS AND ASSEMBLY</b>	 <b>94</b>

4.1 SILICON LAYER MICROFABRICATIONS .....	94
4.1.1 Silicon Oxidizations	95
4.1.2 Photoresist Deposition and Soft Baking	97
4.1.3 Masks Design and the Ultra-Violet (UV) Exposition	99
4.1.4 Photoresist Developing, and Hard Baking	102
4.1.5 Silicon Oxide Etching	103
4.1.6 TMAH Silicon Etching	104
4.2 PVDF LAYER MICROFABRICATIONS .....	109
4.2.1 Sample Preparations	110
4.2.2 Photoresist Deposition and Soft Baking	111
4.2.3 Applied UV, PR Developing, and Hard Baking	112
4.2.3 Aluminum Etching	113
4.3 SENSOR ASSEMBLING .....	115
4.4 SUMMARY .....	119
<b>CHAPTER 5 – EXPERIMENTAL RESULTS AND CHARACTERIZATIONS</b>	<b>120</b>
5.1 EXPERIMENTAL SET-UP .....	120
5.2 EXPERIMENTAL TESTS .....	122
5.2.1 Sensor Calibrations	123
5.2.2 Position Detection of the Applied Concentric Load	125
5.2.2.1 Concentric Load Moves Along Y – Direction	125
5.2.2.2 Load Moves Along the X-Direction	126
5.2.3 A Distributed Load Applied on the Contact Object	129
5.3 SUMMARY .....	134

<b>CHAPTER 6 – DISCUSSION, CONCLUSIONS, AND FUTURE WORK</b>	<b>135</b>
6.1 DISCUSSION.....	136
6.3 FUTURE WORK.....	142
<b>BIBLIOGRAPHY</b>	<b>146</b>
<b>A1. APPENDIX – 1</b>	<b>159</b>
PIEZPELECTRIC EFFECT .....	159
A1.1 PIEZOELECTRIC MATERIALS .....	160
A1.2 PIEZOELECTRIC COEFFICIENTS.....	162
A1.2.1 D – Coefficients	163
A1.2.2 E – Coefficients	163
A1.2.3 G – Coefficients	163
A1.2.4 Dielectric Constants	164
A1.2.5 Capacitance	164
A1.2.6 Young’s Modulus	164
A1.2.7 Density	165
A1.2.8 Curie temperature	165
A1.2.9 Pryoelectricity	165
A1.3 ANALYTICAL APPROACH.....	166
<b>A2. APPENDIX – 2</b>	<b>168</b>
LIST AND SPECIFICATIONS OF THE EQUIPMENT USED FOR RUNNING THE EXPIREMENTS .....	168
<b>A3. APPENDIX – 3</b>	<b>170</b>

EQUIVALENT CIRCUIT OF THE MEASUREMENT SETUP .....	170
A3.1 EQUIVALENT CIRCUIT OF A PIEZO-FILM .....	170
A3.1.1 Effect of Input Resistance	171
A3.1.2 Effect of Input Capacitance	172
A3.1.3 Equivalent Circuit of the Measurement Setup	173

## LIST OF FIGURES

FIGURE 1.1 - TYPICAL MINIMALLY INVASIVE SURGERY TOOLS [6].....	4
FIGURE 1.2 - A TYPICAL ENDOSCOPIC SURGERY SCENE [7] .....	4
FIGURE 1.3 - A CONVENTIONAL LAPAROSCOPIC MINIMALLY INVASIVE SURGERY OPERATIONS [18] .....	7
FIGURE 1.4 - ROBOTICS AND TELE-OPERATORS APPLICATION IN SURGERY [19].....	7
FIGURE 1.5 - (A) MEMS ACCELEROMETERS DEVICES USED IN AN AUTOMOBILE AIRBAG [22] .....	9
FIGURE 1.5 - (B) A LAB-ON-A-CHIP DEVICE WHICH USED IN BIOMEDICAL APPLICATIONS [23] .....	10
FIGURE 1.6 - PROCESS OF SURFACE MICROMACHINING [26].....	12
FIGURE 1.7 - PROCESS OF SILICON ANISOTROPIC WET MICROMACHINING [21].....	13
FIGURE 1.8 - PLANES OF SILICON DIAMOND STRUCTURE [27].....	14
FIGURE 1.9 - SEQUENCE OF PHOTOLITHOGRAPHY PROCESS.....	15
FIGURE 1.10 - THE BASIC PRINCIPLE OF OPTICAL SENSORS.....	17
FIGURE 1.11 - THE BASIC PRINCIPLE OF STRAIN GAUGE SENSORS. [34] .....	18
FIGURE 1.12 - THE BASIC PRINCIPLE OF A CAPACITIVE SENSOR.....	19
FIGURE 1.13 - THE BASIC PRINCIPLE OF A PIEZOELECTRIC SENSOR.....	21
FIGURE 2.1 - THE MICROMACHINED SILICON LAYER .....	35
FIGURE 2.2 - DIMENSIONS OF THE SILICON LAYER .....	35
FIGURE 2.3 - THE MICROFABRICATED SILICON LAYER SPECIFICATIONS.....	36
FIGURE 2.4 - THE MAIN THREE DIRECTIONS OF A UNIAXIAL PVDF FILM.....	37

FIGURE 2.5 - A CROSS-SECTIONAL VIEW OF THE ASSEMBLED SILICON AND PVDF LAYERS	38
FIGURE 2.6 – CROSS-SECTION OF THE PROPOSED TACTILE SENSOR .....	39
FIGURE 2.7 - ENDOSCOPIC GRASPER INTEGRATIONS WITH THE PROPOSED SENSOR.....	40
FIGURE 2.8 - A SIMPLE FIXED-FIXED BEAM WITH POINT LOAD APPLICATION .....	41
FIGURE 2.9 - REACTION MAGNITUDES AS A FUNCTION OF THE POINT LOAD LOCATION .....	42
FIGURE 2.10 - A SIMPLIFIED MODEL OF THE SENSOR CONSISTS OF A SIMPLE BEAM AND CONTACTING TISSUE .....	45
FIGURE 2.11 - GEOMETRY OF THE MODEL WHILE DEFLECTION CAUSED BY A LOAD ACTION .....	45
FIGURE 2.12 - THE EQUIVALENT COMPOSITE BEAM.....	48
FIGURE 2.13 - DEFLECTION OF THE BEAM VERSUS THE OBJECT SOFTNESS .....	51
FIGURE 3.1 - SEQUENCE OF ANSYS STEPS .....	54
FIGURE 3.2 - SEQUENCE OF PREPROCESSOR STEPS .....	54
FIGURE 3.3 - FINITE ELEMENT MESHING OF THE SENSOR.....	57
FIGURE 3.4 – THE SIMPLE PLATE WHICH USED IN THE PARAMETRICAL STUDY .....	58
FIGURE 3.5 - DEFLECTIONS OF THE SILICON PLATE IN Y-DIRECTION VERSUS PLATE LENGTH .....	59
FIGURE 3.6 - DEFLECTIONS OF THE SILICON PLATE IN Y-DIRECTION VERSUS PLATE WIDTH	60
FIGURE 3.7 - DEFLECTIONS OF THE SILICON PLATE IN Y-DIRECTION VERSUS PLATE THICKNESS .....	60
FIGURE 3.8 - DIFFERENT DIMENSIONS OF THE SENSOR FOR THE SAME LOADING RANGE.....	62
FIGURE 3.9 - THE PROPOSED SHAPES OF THE MICROFABRICATED SILICON LAYER .....	63
FIGURE 3.10 - DEFORMATIONS OF THE PROPOSED SHAPES .....	64

FIGURE 3.11 - DEFORMATION CURVES IN THE Z-DIRECTION WHILE A CASE OF POINT LOAD AT THE CENTER .....	65
FIGURE 3.12 - DEFORMATION CURVES IN Z-DIRECTION WHILE A CASE OF DISTRIBUTED PRESSURE LOAD .....	65
FIGURE 3.13 - THE OUTPUT VOLTAGES ON SUPPORTS PVDF LAYERS UNDER POINT LOAD AT THE CENTER OF THE SENSOR ( $D_{31}$ ORIENTED WITH Y-DIRECTION) .....	67
FIGURE 3.14 - THE OUTPUT VOLTAGE ON MIDDLE PVDF LAYER UNDER POINT LOAD AT THE CENTER OF THE SENSOR ( $D_{31}$ ORIENTED WITH Y-DIRECTION) .....	68
FIGURE 3.15 - DISTRIBUTION'S OF THE ACTIVE SENSING ELEMENTS AT EACH PVDF LAYER .....	68
FIGURE 3.16 - THE OUTPUT VOLTAGE ON SUPPORTS PVDF LAYERS UNDER POINT LOAD AT THE CENTER OF THE SENSOR ( $D_{31}$ ORIENTED WITH X-DIRECTION) .....	69
FIGURE 3.17 - THE OUTPUT VOLTAGE ON MIDDLE PVDF LAYER UNDER POINT LOAD AT THE CENTER OF THE SENSOR ( $D_{31}$ ORIENTED WITH X-DIRECTION) .....	69
FIGURE 3.18 - THE FINITE ELEMENT MODEL OF THE SOFT OBJECT WITH AN EMBEDDED LUMP .....	71
FIGURE 3.19 - THE FINITE ELEMENT MODEL OF THE SOFT OBJECT WITH AN EMBEDDED VOID .....	72
FIGURE 3.20 - THE NORMAL STRESS DISTRIBUTION AT THE CONTACT SURFACE, WHEN A PULSATING FEATURE IS EMBEDDED IN THE TISSUE IS CALCULATED.....	73
FIGURE 3.21 - ANSYS MODEL SOLUTION STEPS .....	74
FIGURE 3.22 - THE VOLTAGE COUPLING BOUNDARY CONDITION WHICH APPLIED ON THE BOTTOM OF PVDF LAYERS .....	75

FIGURE 3.23 - NOTATIONS OF THE PVDF SENSING ELEMENTS .....	76
FIGURE 3.24 – TOP VIEW OF THE MESHED SENSOR SHOWING A POINT LOAD APPLICATION AT THE CENTER .....	77
FIGURE 3.25 - OUTPUT VOLTAGES AT THE PVDF SENSING ELEMENTS WHEN A POINT LOAD IS APPLIED AT THE CENTER OF THE SENSOR .....	78
FIGURE 3.26 - OUTPUT VOLTAGES ON PVDF LAYERS VERSUS THE DIFFERENT LOAD MAGNITUDES.....	79
FIGURE 3.27 – POSITION OF THE POINT LOAD APPLICATION ALONG Y- DIRECTION .....	80
FIGURE 3.28 - OUTPUT VOLTAGES AT THE SENSING ELEMENTS WHEN A POINT LOAD IS APPLIED ALONG Y- DIRECTION .....	81
FIGURE 3.29 - THE DIFFERENCE BETWEEN OUTPUT VOLTAGES AT THE SENSING ELEMENT SUPPORT12 (V1) AND THE SENSING ELEMENT SUPPORT22 (V2).....	82
FIGURE 3.30 - SUMMATION OF OUTPUT VOLTAGES AT THE SENSING ELEMENTS SUPPORT12 (V1) AND THE SENSING ELEMENT SUPPORT22 (V2).....	83
FIGURE 3.31 - POSITION OF THE POINT LOAD APPLICATION ALONG X- DIRECTION.....	84
FIGURE 3.32 - OUTPUT VOLTAGES AT THE SUPPORTS PVDF SENSING ELEMENTS WHEN A POINT LOAD IS APPLIED ALONG X- DIRECTION .....	84
FIGURE 3.33 – OUTPUT VOLTAGES AT THE MIDDLE PVDF SENSING ELEMENTS WHEN A POINT LOAD IS APPLIED ALONG X- DIRECTION .....	85
FIGURE 3.34 - AN ELASTIC OBJECT/ TISSUE IS ADDED AND MODELED WITH THE SENSOR....	87
FIGURE 3.35 - FINITE ELEMENT MESHING OF THE SENSOR WITH THE CONTACTING OBJECT/ TISSUE.....	88

FIGURE 3.36 - DEFLECTION OF THE SENSOR WHEN A DISTRIBUTED LOAD IS APPLIED ON TOP OF THE OBJECT .....	89
FIGURE 3.37 - OUTPUT VOLTAGE AT THE MIDDLE PVDF SENSING ELEMENTS .....	90
FIGURE 3.38 - OUTPUT VOLTAGES AT THE MIDDLE PVDF SENSING ELEMENTS VERSUS DIFFERENT OBJECT/ TISSUE STIFFNESSES AT 5 N GRASPING LOAD .....	91
FIGURE 3.39 – OUTPUT VOLTAGES AT THE MIDDLE PVDF SENSING ELEMENTS VERSUS DIFFERENT OBJECT/ TISSUE STIFFNESSES AT DIFFERENT GRASPING LOADS .....	91
FIGURE 4.1 – OXIDATION FURNACE SET-UP .....	96
FIGURE 4.2 – SAMPLES ARE VERTICALLY POSITIONED USING A QUARTZ HOLDER .....	96
FIGURE 4.3 – PHOTORESIST DEPOSITION ON THE SAMPLE BY SPINNING .....	98
FIGURE 4.4 – BAKING OVEN.....	98
FIGURE 4.5 – THE FIRST LIGHT FIELD MASKS FOR TEETH MICROFABRICATIONS .....	100
FIGURE 4.6 – DETAILS OF THE CONVEX CORNER COMPENSATION METHOD .....	100
FIGURE 4.7 – SILICON MASKS EDGES ARE ALIGNED WITH THE WAFER FLAT .....	101
FIGURE 4.8 – QUINTEL DOUBLE-SIDED MASK ALIGNER.....	101
FIGURE 4.9 – THE SECOND LIGHT FIELD MASKS FOR SUPPORTS MICROFABRICATIONS.....	102
FIGURE 4.10 – PROCEDURES OF THE SILICON OXIDE WET ETCHING .....	104
FIGURE 4.11 – THE TMAH BATH SET-UP.....	105
FIGURE 4.12 – TOP VIEW OF THE SAMPLE SHOWING THE TEETH SHAPES.....	107
FIGURE 4.13 – THE BOTTOM VIEW OF SILICON SHOWING THE CHANNEL AND SUPPORTS...	107
FIGURE 4.14 – THE <111> SIDE WALLS AND THE COMPENSATED CONVEX CORNERS OF THE MICROFABRICATED TEETH .....	108

FIGURE 4.15 – UPPER AND LOWER E EDGES OF THE TOOTH SIDE WALL WHICH IS USED TO VERIFY THE TOOTH HEIGHT .....	108
FIGURE 4.16 – CROSS SECTIONAL VIEW OF THE MICROFABRICATED SILICON SHOWING A TOOTH CROSS-SECTION .....	109
FIGURE 4.17 – A TYPICAL METALIZED PVDF SAMPLE OF 25 $\mu\text{M}$ THICKNESS.....	110
FIGURE 4.18 – THE LIGHT FIELD MASKS WHICH IS USED FOR PATTERNING THE PVDF SAMPLE .....	112
FIGURE 4.19 – THE PVDF SAMPLE AFTER HARD BAKING.....	113
FIGURE 4.20 – THE PATTERNED PVDF FILM.....	114
FIGURE 4.21 – FIRST STEP OF THE SENSOR ASSEMBLY.....	115
FIGURE 4.22 – SECOND STEP OF THE SENSOR ASSEMBLY.....	116
FIGURE 4.23 – DETAILS OF THE OUTPUT TERMINAL PREPARATIONS.....	117
FIGURE 4.24 – BOTTOM VIEW OF THE ASSEMBLED PATTERNED PVDF AND MICROFABRICATED SILICON .....	117
FIGURE 4.25 – SIDE VIEW OF THE COMPLETE SENSOR ASSEMBLY.....	118
FIGURE 4.26 – TOP VIEW OF THE MICROFABRICATED SENSOR.....	118
FIGURE 5.1 - THE EXPERIMENTAL SET-UP.....	121
FIGURE 5.2 - PHOTOGRAPH OF THE COMPLETE SETUP .....	122
FIGURE 5.3 - THE PROBE WHILE APPLYING A CONCENTRIC LOAD AT THE CENTER OF THE SENSOR .....	123
FIGURE 5.4 - THE CALIBRATION CURVES.....	124
FIGURE 5.5 - OUTPUT VOLTAGES AT THE SENSING ELEMENTS WHEN A CONCENTRIC LOAD IS APPLIED ALONG Y- DIRECTION .....	126

FIGURE 5.6 - THE DIFFERENCE BETWEEN OUTPUT VOLTAGES AT THE SENSING ELEMENT SUPPORT12 (V1) AND THE SENSING ELEMENT SUPPORT22 (V2) .....	127
FIGURE 5.7 - OUTPUT VOLTAGES AT THE SUPPORTS SENSING ELEMENTS VERSUS X- LOCATION OF THE LOAD .....	128
FIGURE 5.8 - OUTPUT VOLTAGES AT THE MIDDLE SENSING ELEMENTS VERSUS X- LOCATION OF THE LOAD .....	129
FIGURE 5.9 - ELASTOMERS WITH DIFFERENT STIFFNESSES WHICH USED ON THE EXPERIMENT .....	130
FIGURE 5.10 - A UNIFORM DISTRIBUTED LOAD APPLIED ON THE TOP OF CONTACTING TISSUE (ELASTOMER) .....	131
FIGURE 5.11 - OUTPUT VOLTAGES AT THE MIDDLE PVDF SENSING ELEMENTS VERSUS DIFFERENT TISSUES (ELASTOMERS) STIFFNESSES AT 5 N GRASPING LOADS .....	132
FIGURE 5.12 - OUTPUT VOLTAGES AT THE MIDDLE PVDF SENSING ELEMENTS VERSUS A DIFFERENT TISSUES (ELASTOMERS) STIFFNESSES AT DIFFERENT GRASPING LOADS...	133
FIGURE A1.1 - PIEZOELECTRIC IN IONIC CRYSTALS SUCH AS QUARTZ, ION POSITION IN QUARTZ LATTICE WITH AND WITHOUT APPLIED STRESS.....	160
FIGURE A1.2 - VOLTAGE GENERATION BY PIEZOELECTRIC SUBSTANCE .....	166
FIGURE A2.1 – SOME OF THE USED PROBES IN EXPERIMENTS.....	169
FIGURE A3.1 - PIEZO-FILM ELEMENT AS A SIMPLE VOLTAGE GENERATOR .....	171
FIGURE A3.2 - THE MEASUREMENT CIRCUIT MODELED AS A VOLTAGE DIVIDER .....	172
FIGURE A3.3 - EQUIVALENT CIRCUIT OF A SENSING ELEMENT CONSIDERING THE INPUT CAPACITANCE .....	173

## **LIST OF TABLES**

Table 2.1	Material properties of Silicon wafer	34
Table 2.2	Material properties of Polyvinylidene fluoride (PVDF) film	38

## Symbols

$[k]$	Element Stiffness Matrix
$\{d\}$	Element Nodal Displacement Vector
$\{D\}$	Electric Flux Density ( $C/m^2$ )
$\{E\}$	Electric Field Vector ( $V/m$ )
$\{F\}$	Force Vector for System
$\{F^{ac}\}$	Force Vector Due to Acceleration Effects
$\{F^{nd}\}$	Applied Nodal Force Vector
$\{F^{th}\}$	Thermal Strain Force Vector
$\{F^{pr}\}$	Pressure Load Vector
$\{L^{nd}\}$	Applied Nodal Charge Vector
$\{L^c\}$	Charge Density Load Vector
$\{L^{sc}\}$	Surface Charge Density Load Vector
$\{S\}$	Strain Vector (Dimensionless)
$\{T\}$	Stress Vector ( $N/m^2$ )
$\{U\}$	Displacement Vector for System
$\{V\}$	Electric Potential Vector
$[C]$	Structural Damping Matrix
$[K]$	Structural Stiffness Matrix
$[M]$	Structural Mass Matrix
$[K^d]$	Dielectric Coefficient Matrix
$[K^z]$	Piezoelectric Stiffness Matrix

3-D	Three Dimensional
$Al$	Aluminum
A/D	Analog to digital
B	Beam and the Contacting Tissue Width
C	Capacitance
$d_{31}$ , $d_{32}$ , and $d_{33}$	Piezoelectric constants
DAQ	Data Acquisition system
DC	Direct current
E	Piezoelectric Coefficient ( $C/m^2$ )
E	Modulus of Elasticity
$E_b$	Beam Modulus of Elasticity
$E_t$	Contacting Tissue Modulus of Elasticity
$E_{eq}$	Modulus of Elasticity of the Equivalent Beam
$g_{31}$ , $g_{32}$ , and $g_{33}$	Piezo-Coefficients Related to the Voltage ( $V\cdot m/N$ )
GPa	Giga-Pascal
Hz	Hertz
$I_{eq}$	The Second Moment of Inertia of the Equivalent Beam
IC	Integrated Circuit
$l$	Length
M	Bending Moment
MEMS	Micro Electro Mechanical Systems
MIS	Minimal Invasive Surgery
MPa	Mega-Pascal

MR	Magneto-Resistive
MST	Micro-Systems Technology
N	Newton
N.A.	Neutral Axis
pC	Pico- Coulomb
PR	Photoresist Material
PVDF	Polyvinylidene Fluoride Polymer
Q	Charge
R	Radius of Curvature
$t_b$	Beam Thickness
$t_t$	Contacting Tissue Thickness
UV	Ultra-Violet Light
V	Voltage
E	Strain
$\mu\text{m}$	Micro-Meter
$\Omega$	Ohms
$\delta\ell$	Elongation
$\sigma$	Mechanical Stress
$\Omega$	Distributed Load
C°	Degree Celsius

## **Chapter 1 - Introduction and Literature Review**

Our sense of touch indicates the shape, size, quality and temperature of objects and is one of the most important contributions to our brains for decision making. Interaction between humans and the surrounding environment during different manual tasks supplies useful information. This thanks to the mechanoreceptors cells inside our hands which provide us with the ability of discriminating among surface grains, distinguishing between the size and quality of different objects and differentiating between hard and soft items. Mechanoreceptors are very precise within wide ranges of applications and are effective on static, dynamic and temperature excitations. By using sense of touch, we can perform many precise tasks with our hands. Were we to be deprived of this feeling, the story will be complicated, and our ability will be limited with poor precision [1]. That is exactly the case with many applications in our everyday lives, making it a significant impetus for scientific thinking. Recently, many efforts of research around the world are focused on solving and improving the subject of tactile sensing in many fields such as manipulators, virtual reality, and more generally for medical applications [2].

This thesis introduces a novel multifunctional micromachined tactile sensor. The contribution of this research is to bring the level of feel of touch and the precise sensitivity of the human finger to the manipulators and other medical applications especially in minimally invasive surgical operations such as endoscopic surgeries.

## **1.1 Minimally Invasive Surgery**

A few years ago, some special surgical procedures called Minimally Invasive Surgery (MIS) using specialized tools was introduced [3]. In the beginning, MIS applications were limited to specific kinds of operations such as cholecystectomy surgery [4]. Nowadays, MIS has become a standard surgical procedure, widely used and replacing most of the traditional open surgery procedures. MIS has become widely accepted and recommended because of its benefits over traditional open surgeries. The drawback to open surgeries is that most require large single incision in order to give the surgeon enough space to see the operation site and to perform his actions using fingers or instruments [5]. In most cases, damage occurs to skin, muscle, connective tissue, and bone to reach the region of interest and can even cause much greater injuries than the therapeutic procedure itself. This results in more pain to the patient, longer recovery time, and difficulties due to surgical ordeal [3, 5]. The current trend is accelerating toward safer and more accurate surgery with reduced operating time. MIS operations, therefore, are becoming more common and are replacing most of the traditional surgeries. MIS reduces the unnecessary suffering caused by conventional surgical procedures because of the reduced incision size [5]. Mainly, most of incisions associated with MIS are less than about 1 cm, which is enough for inserting the MIS tool, such as; catheters, endoscopes, laparoscopies tools, and other tubular structures [3].

The first gallbladder removal, a cholecystectomy, using MIS and an endoscopic tool was performed in 1987. Gallbladder removals, along with appendectomies, are some of the most common minimally invasive procedures in practice. Many companies have

designed a number of different endoscopes for different specific operations. The laparoscope, for example, is used for surgery in the abdomen and the thoracoscope is a tool which used by heart surgeons to examine the internal chest [4].

Generally, MIS can be defined as a procedure carried out by a specialist surgeon through a small opening in the body, using specialized tools and with the help of other visualization techniques or haptic interfaces which do not require any direct access [3]. MIS operations utilize small incisions through which cameras and instruments are passed to accomplish the operation from within a body cavity whereas the conventional open surgical approaches use large incisions to provide the maximum exposure of the operative site [5]. The MIS approach offers several advantages over the conventional one. Skilled and specialist surgeons regularly perform MIS operations as quickly as they perform equivalent open operations [3]. Some of the minimally invasive surgical tools which are currently used during many of the minimal invasive surgical operations are shown in Figure 1.1; most of them are of long tube structure with small diameter to be inserted through small hall in the patient body. Some of them are graspers and others with different shapes for different tasks. A typical endoscopic MIS surgery operation is shown in Figure 1.2.

The general advantages and benefits of minimally invasive surgeries as opposed to conventional open surgeries include smaller incisions, less pain during the recovery period, reduced blood loss and scarring, faster recovery time, shorter hospitalization, fewer complications due to infection, better prognosis and finally reduced overall costs [3].

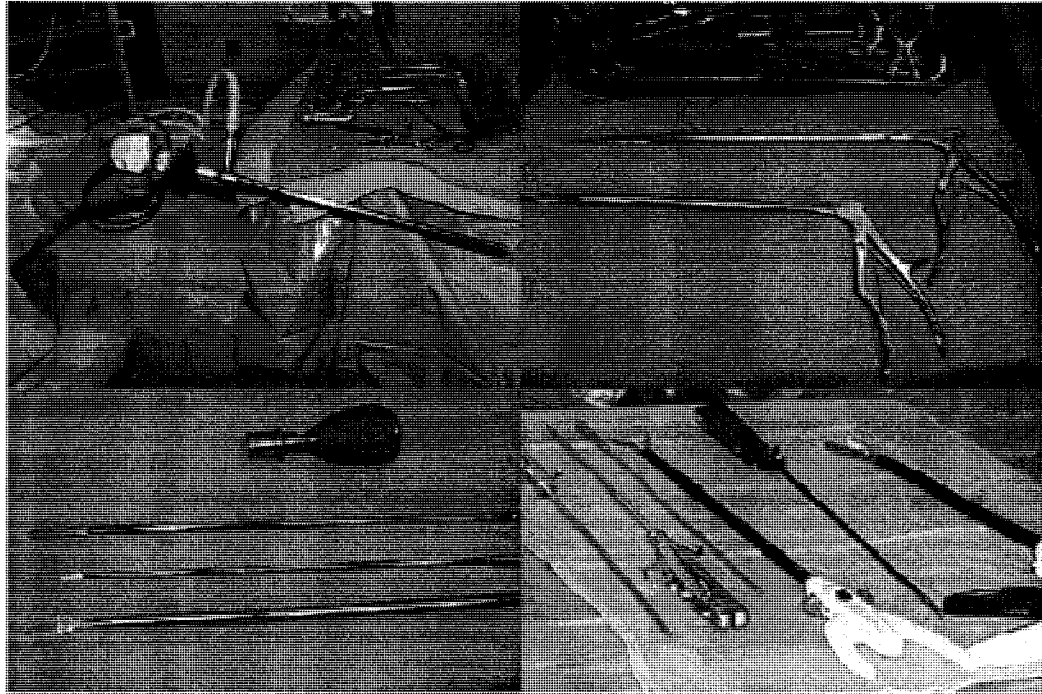


**Figure 1.1 - Typical minimally invasive surgery tools [6]**

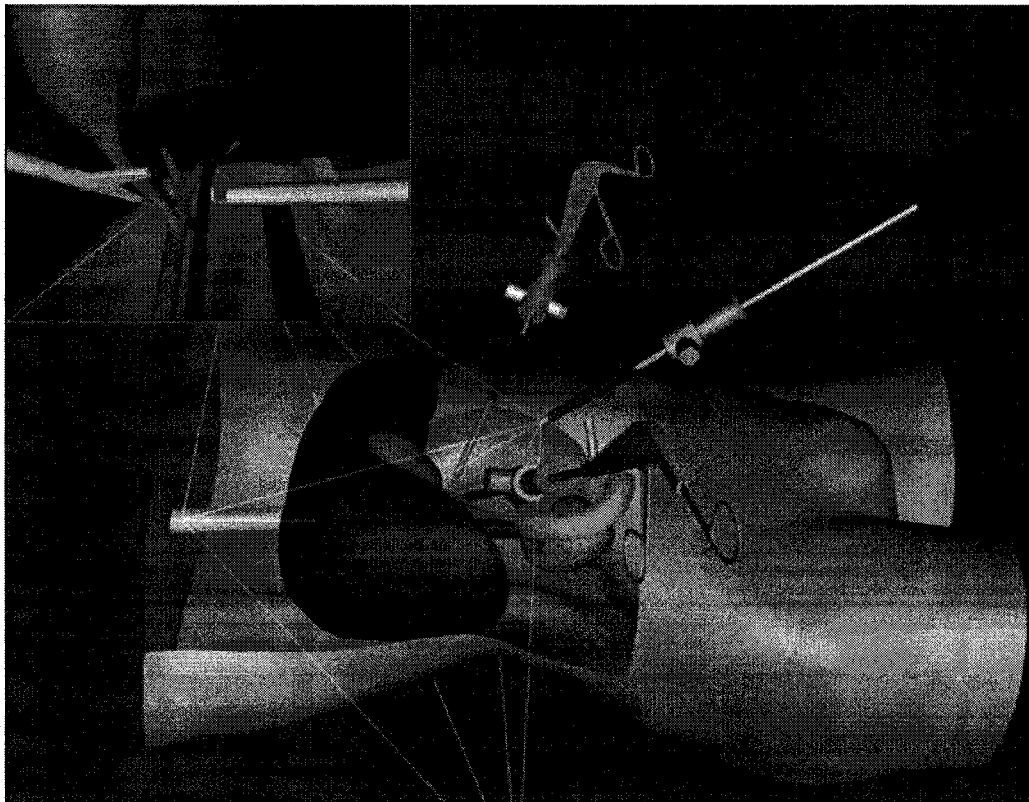


**Figure 1.2 - A typical endoscopic surgery scene [7]**

One of the major drawbacks of current minimally invasive surgeries is the lack of tactile feedback, reduced location perception, the reduced dexterity due to restricted vision, difficulty in handling the instruments and very restricted mobility [8, 9]. During most of the surgeries, the tissues under operation are very soft and sensitive to any excessive force. They are also hidden and located at awkward locations make the surgery more difficult and sensitive. In such situations a serious challenge faces the surgeon and improved tactile sensing of tissues properties is required [9, 10]. It is necessary to direct a feedback signal to the surgeon which supplies information as to the properties of the grasped tissues and to indicate the precise magnitudes and locations of the applied forces during the surgical procedure [9-11]. Because of this missing information, the surgeon will not be able to discern important properties of the grasped tissues such as its softness, compliance, and the surface texture at the site of operation [9, 10, 12]. This lack of information currently poses a serious challenge to the surgeon since it renders MIS less precise and harmful.

## **1.2 Tactile Sensing**

Tactile sensing is defined as the continuous sensing of variable contacting forces such as the sensing ability of the human finger [11]. These sensations can be concluded as the sense of force, softness, temperature, and the roughness of the object [11, 13]. One of the most exciting and quickly rising areas where the tactile sensing is really important is in robotics surgery applications. That is because soft tissue can only be properly checked-up and recognized by evaluating its softness, viscosity, and elasticity properties [12, 13]. One of the highly evaluated procedures in the decision making during surgery is

palpation of tissues and organs where it is an essential step for any surgical process [2, 14-17].

To perform MIS more effectively, the surgeon should be able to feel the tissue, sense the pressure of blood vessels and ducts during the procedure [2, 12, 14-17]. This ability is of great use during manipulation tasks such as when grasping internal organs, gentle load transfer during lifting, and suturing and removing the tissues [13]. The need of feeling the tissue and its softness is particularly important during surgical operations.

In laparoscopy, long slender tools are inserted through small openings on the human body wall. Then the surgeon uses a range of tips mounted on instruments guided by video feedback images. As the instruments are rigid rods and effectively have fixed pivots at the entry points, the available degrees of freedom are restricted and therefore demand extra operator expertise. It is clear that tactile sensing is greatly needed in this area [4, 8, 13]. Conventional Laparoscopic MIS operation is shown in Figure 1.3.

In MIS surgery, stereoscope vision and tactile information about tissue consistency are no longer available to the surgeon. To compensate for these sensory deficits, various tissues can be characterized with an electromechanical sensor that records their properties. In future, these sensors will be integrated into surgical instruments, providing the surgeon with information about tactile properties of tissue [4, 12, 20]. Development of these sensors will improve MIS and robotics surgery as well. Robotics and tele-operator surgery operations with the support of tactile feedback are becoming more important and are opening the door for a promising future for safer surgery [4, 12]. Figure 1.4 describes Robotics and tele-operator surgery operations.

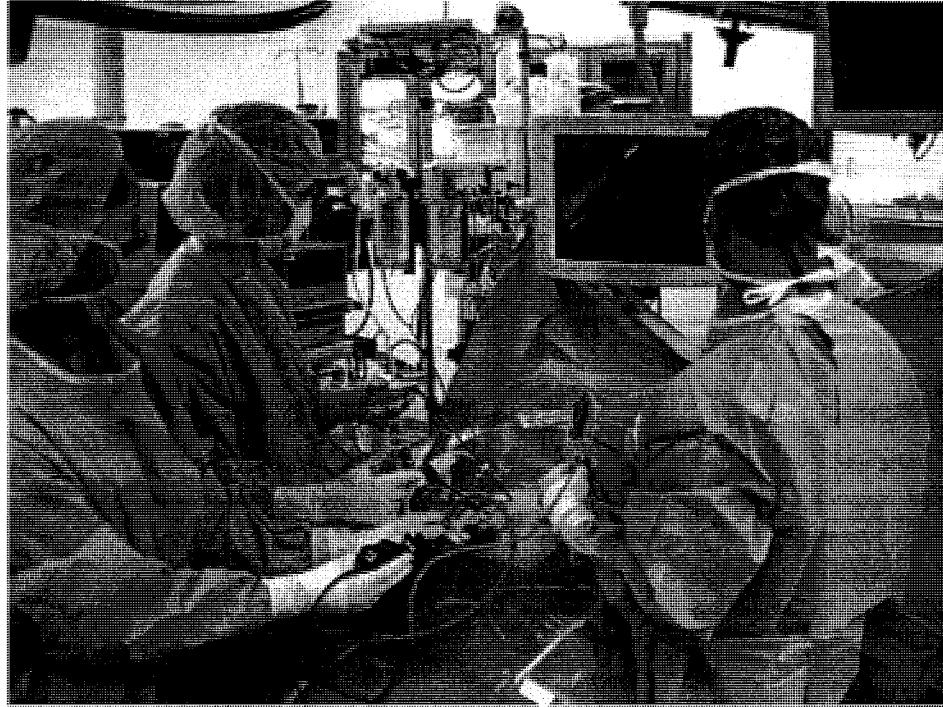


Figure 1.3 - A conventional laparoscopic minimally invasive surgery operations [18]

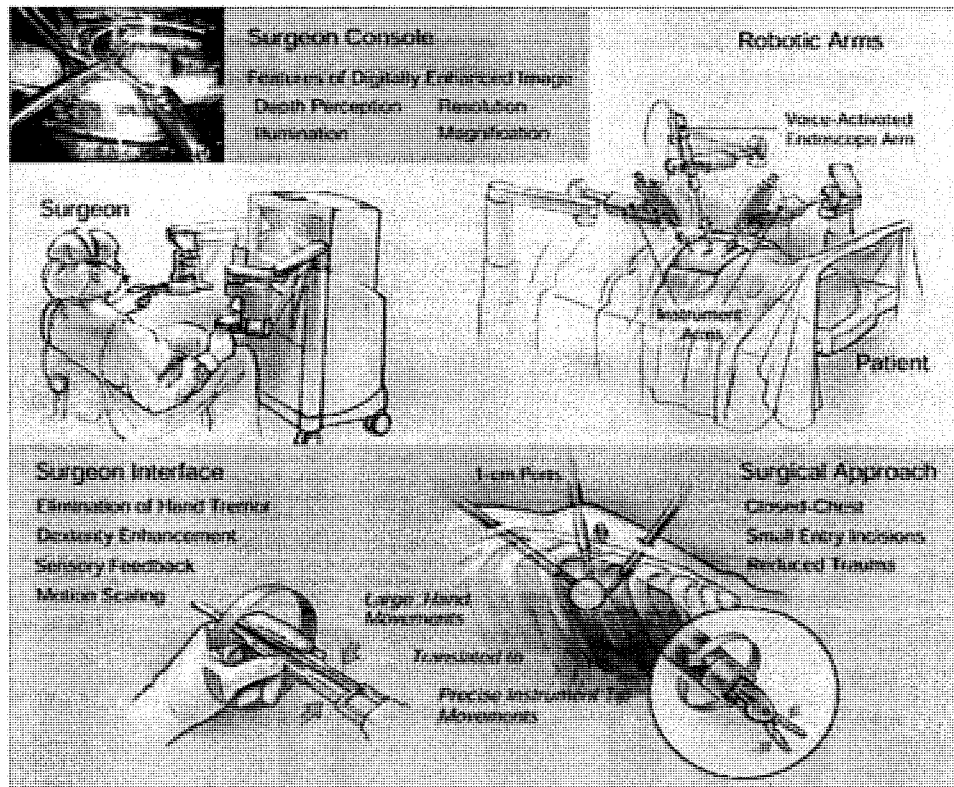


Figure 1.4 - Robotics and tele-operators application in surgery [19]

Because MIS is a precise procedure, the associated staff, tools, and sensors have therefore also to be precise and accurate with high sensitivity [10]. The necessary precision range of the associated tactile sensing lies in the range of microns to a few millimeters [12]. The typical tactile sensors which are recommended for use during MIS operations have to be small in size, highly sensitive, have low manufacturing and integrations cost, and finally the possibility of being disposable after surgery [5, 10, 12]. Combining all of these features with MIS is leading the research spot to the integration and utilization of the microfabrication and MEMS in the field of tactile sensing and MIS. Merging these three fields is opening a new future for safer and less invasive surgery.

### **1.3 Micro-Electro-Mechanical Systems (MEMS)**

The Micro-Electro-Mechanical System (MEMS) is a group of sensors, actuators and micro-machines that are physically small in size ranging from sub-micrometers to millimeters. A MEMS device can be any number of components, ranging from few parts to millions. These systems have electrical and/or mechanical components that are dependent on each other and are fabricated on a single common substrate [21].

MEMS, sometimes called Micro-Systems-Technology (MST), is growing rapidly and is becoming more important in the commercial marketplace [21]. MEMS is being applied to many other fields as the technologies for microfabrication and miniaturization are continually being developed and improved. Many major commercial applications and markets for MEMS are available nowadays – such as computer storage systems, biomedical devices, Micro-fluidics, Lab-On-A-Chips, automobiles, and genetic engineering – to name but a few. Many predict that the biomedical industry will be the

major user of Microsystems after the automotive industry [21]. The term Bio-MEMS has been used extensively by the MEMS industry and in the academic field in recent years [12]. Two examples in which MEMS is applied on different fields are shown in Figure 1.5 (a) and Figure 1.5 (b).

The core element in MEMS generally consists of two principal components namely the sensing element (or an actuating element) and a signal processing unit. Micro sensors are built to sense the existence and the intensity of certain physical, chemical, or biological quantities such as temperature, pressure, force, sound, light and chemical compositions. Micro sensors have the advantage of being sensitive and accurate with minimal amount of required sample substance and can be mass-produced [21].

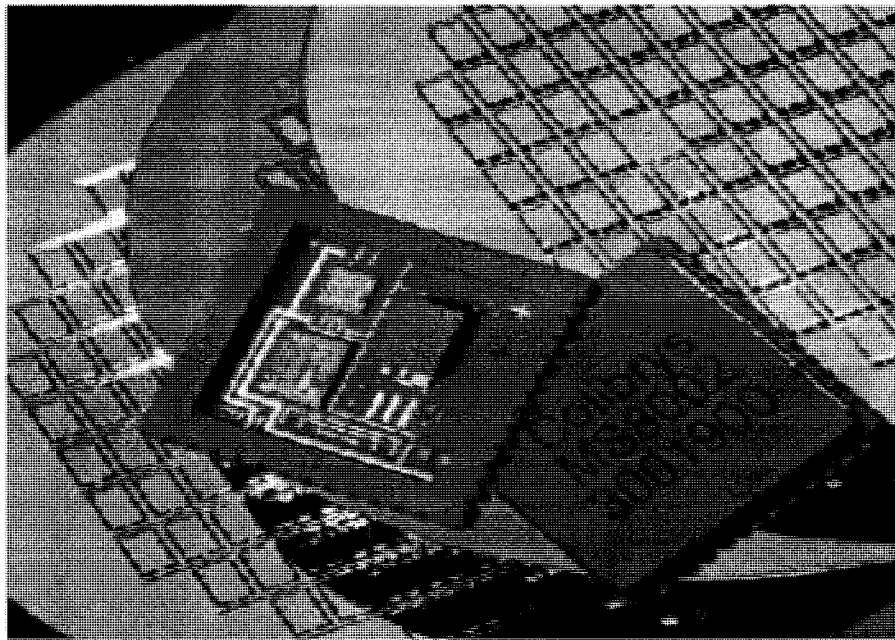


**Figure 1.5 - (a) MEMS accelerometers devices used in an automobile airbag [22]**

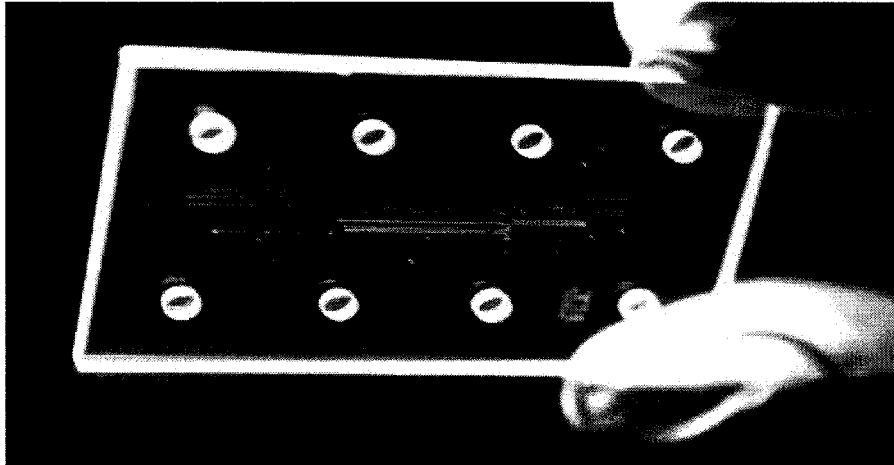


**Figure 1.5 - (b) A Lab-On-A-Chip device which used in biomedical applications [23]**

There are many types of micro sensors developed for different applications and widely used in industry today [21] including biosensors, chemical sensors, optical sensors, thermal and pressure sensors. Biosensors, and the recently developed biomedical sensors, will have a significant share in the micro sensors market in the near future [12]. Micro biomedical sensors, which are mainly used for diagnostic analysis, require only a minute amount of sample yet produce significant results faster than traditional biomedical instruments [12, 21].

MEMS fabrication technology can also be used in the MIS tactile sensing field in order to manufacture very small micro-tactile sensors which can be custom-made to the surgeon's requirements [12]. These microfabricated tactile sensors are creating a revolution in the field of Minimally Invasive Endoscopic Surgery (MIES) [8, 11, 12, 24]. The advantages of miniaturization of the sensors include improved dexterity of the surgical tools. In addition, because these sensors can be manufactured and produced in large batches, the

resulting low unit cost also allows for their disposability [11, 12] which obviates the necessity for cleaning thereby cutting costs and provide for safer surgery [8, 9].

## **1.4 MEMS Microfabrication Techniques**

The fabrication of MEMS devices is usually done by surface micromachining and/or bulk micromachining [21, 25].

The most important material used in most of devices for many applications is silicon wafers of which there are a number of different types commercially available depending on the structure required [21, 25]. The following sections briefly introduce micromachining methods and silicon wafer structure.

### **1.4.1 Surface Micromachining**

Surface micromachining is based on the deposition and etching of different structural layers built on the surface of substrate. The substrate could be silicon wafer, glass, plastic, or many others. For this micromachining technique, the first step is to deposit layers on top of the silicon wafer or any other chosen substrate. These layers are later selectively etched by photolithography using either a wet etching involving an acid or a dry etching involving an ionized gas, or plasma. Surface micromachining can involve as many layers as is needed, with a different mask producing a different pattern on each layer [21, 25]. The process of the surface micromachining is illustrated in Figure 1.6.

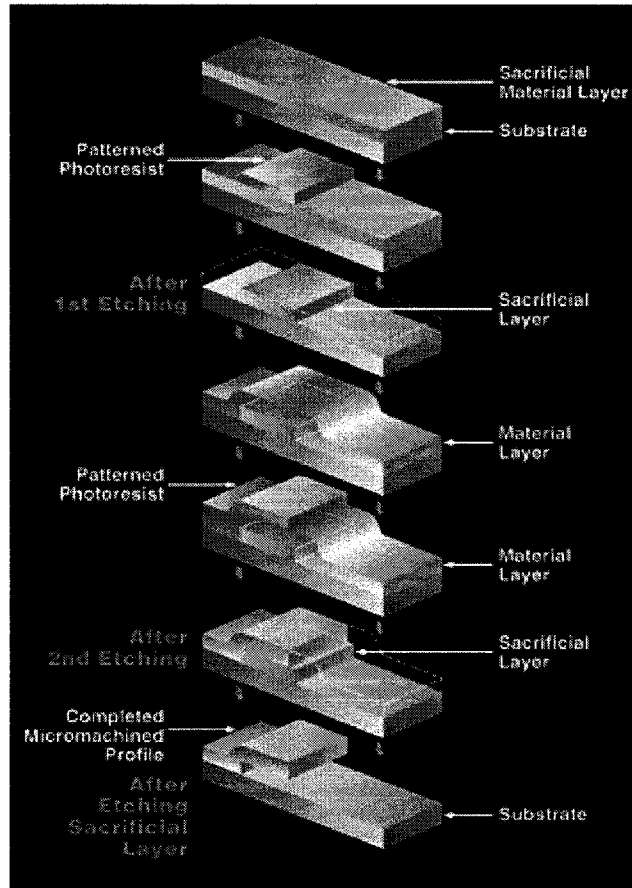


**Figure 1.6 - Process of surface micromachining [26]**

### 1.4.2 Bulk Micromachining

Bulk micromachining creates new structures by selectively etching into the substrate. In general, the silicon wafers are preferably used as the substrates of bulk micromachining because of its anisotropic properties. Bulk micromachining starts with a silicon wafer or other substrates and, using photolithography, will selectively etch inside the substrate. Photolithography is used to transfer a pattern from a mask to the surface of the substrate. Bulk micromachining, as well as surface micromachining, can be done using either wet etching or dry etching. The most common bulk etching method, when using silicon, is

anisotropic wet etching because it takes advantage of the silicon crystal structure [21, 25].

The process of anisotropic wet micromachining is illustrated in Figure 1.7.

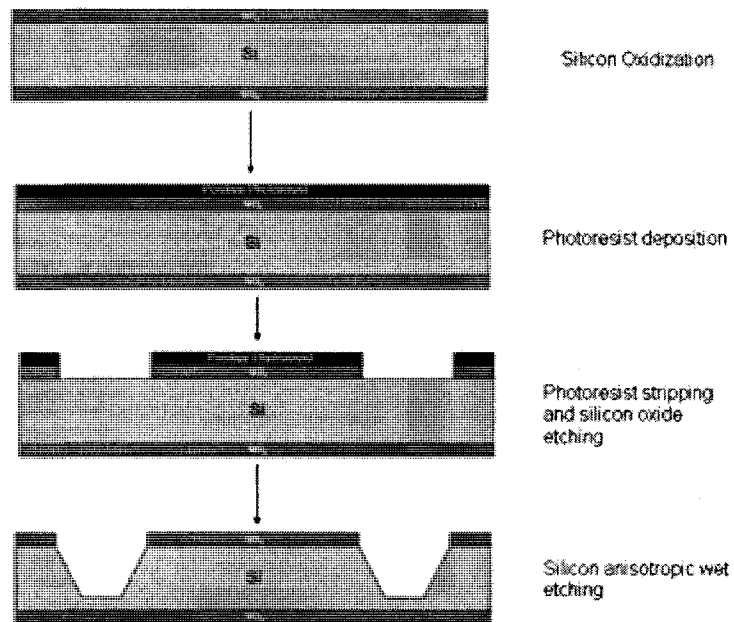


**Figure 1.7 - Process of silicon anisotropic wet micromachining [21]**

### 1.4.3 Silicon Wafers

Silicon wafers have specific crystal orientations in which each crystal is built-up from atoms arranged periodically in lines and planes. Certain planes have weaker bonds and are more susceptible to etching. In cavities having angled walls, the etch results for the angle is a function of the crystal orientation of the substrate. Silicon has a diamond structure of the atoms arrangements forming the unit cell and its planes are shown in Figure 1.8.

Silicon anisotropic wet etching is generally carried out using alkaline liquid solvents, such as potassium hydroxide (KOH) or tetramethylammonium hydroxide (TMAH).

Using these solvents, silicon regions which have been left exposed by the photolithography masking step is dissolved and etched out. These alkali solvents etch the silicon in a highly anisotropic way, with some crystallographic orientations dissolving up to 1000 times faster than others. Such an approach is often used with very specific crystallographic orientations in the raw silicon to produce a unique structures and features on the wafer, these features can be atomically smooth if the etch is carried out correctly with dimensions and angles being extremely accurate [21, 28, 29].

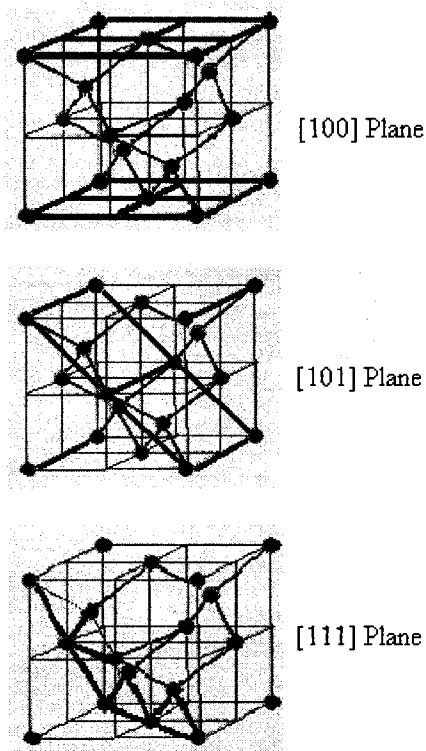


**Figure 1.8 - Planes of silicon diamond structure [27]**

#### **1.4.4 Photolithography Process**

Photolithography plays a key role in fabrication of all Micro-Electro-Mechanical devices. During fabrication, it is important to select a portion of the sample to be applied to the

variety of fabrication steps, and leave the rest of the sample intact. Photolithography offers the flexibility of this selectivity. Patterning of geometry with extremely high precision has been a major challenge for engineers. Photolithography has been the only possible solution for producing the desired high precision patterns on substrates at the micro-scale level [29].

Photolithography is conducted in a room illuminated by a yellow light to reduce the adverse effects of light on the photosensitive resist material. In this process, photoresist (PR) is applied on a wafer by spin coating. The coated wafer is then dried in an oven, exposed to UV light, and then developed using a developer. The two kinds of Photoresist are positive PR, and negative PR. With positive PR, the exposed regions will be etched out in the developer, but the unexposed regions will remain. The opposite will happen with the negative PR [28]. The process of photolithography with positive photoresist is shown in the Figure 1.9.

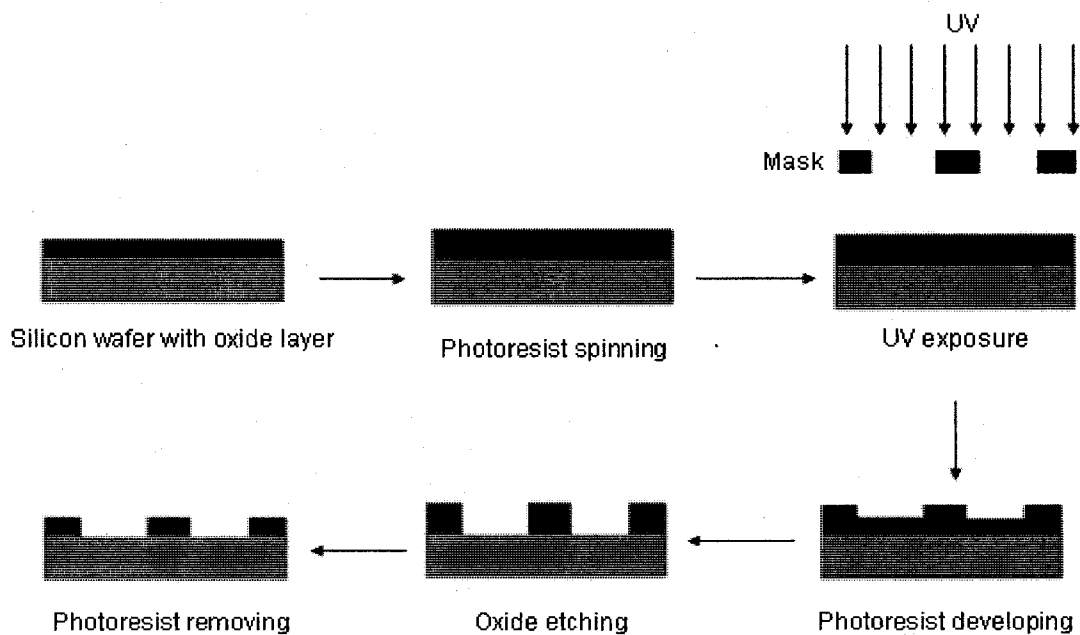


**Figure 1.9 - Sequence of photolithography process**

## **1.5 Tactile Sensor Technologies**

With the rapid growth of different technologies, many available principles can be exploited for the development of tactile sensors. For each application there is a preferable kind of tactile sensor principle depending on the required accuracy, operation conditions and manufacturing costs. Many sensor principles could be used but we will talk in brief about the major principles which are used most frequently in tactile sensory applications such as optical sensors, strain gauge sensors, capacitive sensors, magnetic based sensors, and finally, perhaps the most frequently used, piezoelectric sensors [30].

### **1.5.1 Optical Sensors**

Recently, development in the optical technology field has grown rapidly leading to the application of this technology to a wide range of tactile sensors. Optical-based sensors is highly recommended because their advantages over conventional models such as its immunity to electromagnetic interference, resistance to harsh environment, capability for multiplexing, high potential of miniaturization, flexibility, lightness, dielectricity, and the low light power usage [10]. The operating principles of optical-based sensors are well known and are divided into two classes namely Intrinsic and Extrinsic. In the Intrinsic type, the optical phase, intensity, or polarization of transmitted light, are modulated without interrupting the optical path. In the Extrinsic type, the physical stimulus interacts with the light external to the primary light path [31]. The principle of the optical fiber tactile sensor is shown in Figure 1.10.

One of the major disadvantages associated with the optical-based tactile sensors is the sensitivity to vibration, and the difficulties in meeting the requirements of light emitters and receivers [10, 31].

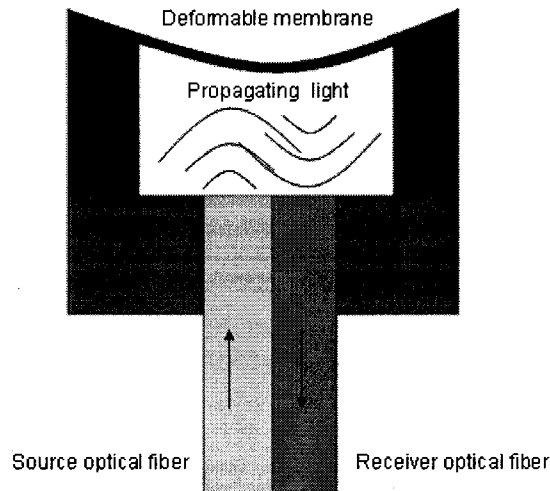


**Figure 1.10 - The basic principle of optical sensors**

### **1.5.2 Strain Gauge Sensors**

In general, the term strain is defined as the amount of deformation which is caused by stressful affects on the body as a result of physical actions from external forces [30, 31].

There are several methods of measuring this strain, but the most common method is the use of strain gauge which is a device whose electrical resistance varies in proportion to the amount of strain in the device. The most widely used gauge is the bonded metallic strain gauge [32] which consists of a very fine wire or metallic foil arranged in a grid pattern. The strain gauge is connected directly to the deformable face where the strain experienced by the test specimen is transferred directly to the strain gauge [32]. Due to that transferred strain, the strain gauge responds with a linear change in its electrical resistance. When a constant current passes through the strain gauge, the change in

resistance can be read by measuring the voltage across its terminals [33]. The strain gauge with its conditioning circuit is shown in Figure 1.11.

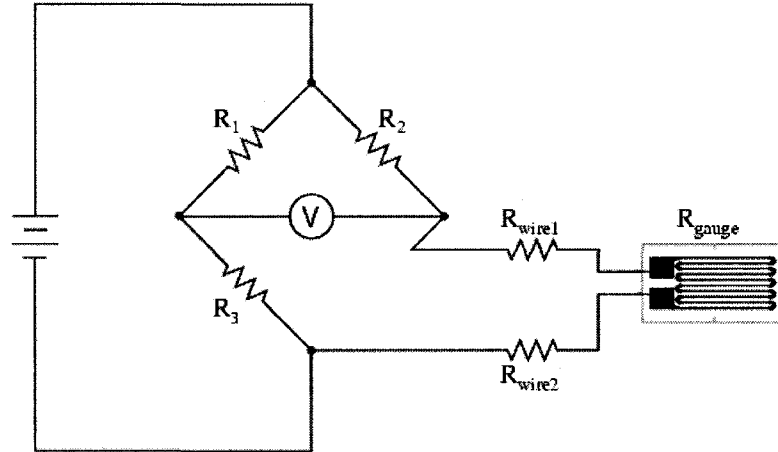


**Figure 1.11 - The basic principle of strain gauge sensors. [34]**

Strain gauges sensors have many of advantages such as reliability, high accuracy, good static and dynamic response, together with its resistance to shock and vibration. Its major disadvantages are low stability, limited range and nonlinearity [33, 35, 36].

### 1.5.3 Capacitive Sensors

Capacitive sensors simply consist of two separated thin plates, usually manufactured from metal or metal-coated quartz. The plates are exposed to the process pressure on one side and to a reference pressure on the other side. The plate deflects when a pressure is applied and alters the distance between the two plates. This translates directly to a change in capacitance which, in turn, can be related to the measurement of the pressure exerted on plate [35, 36]. The structure of a simple capacitive sensor structure is shown in Figure 1.12.

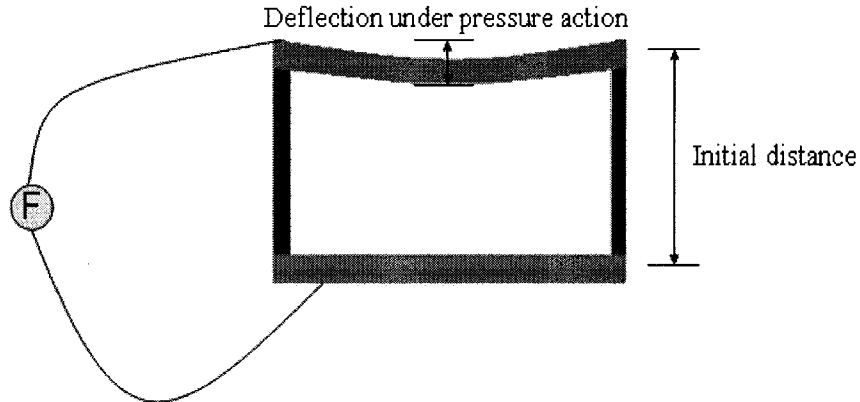


**Figure 1.12 - The basic principle of a capacitive sensor**

Capacitive sensors are a good choice because of its simple construction, compact size and mass, and its active response due both static and dynamic load. The limitations are its high impedance, temperature drift and the required complicated conditioning circuit [35].

#### **1.5.4 Magnetic Based Sensor**

This kind of sensor comprises special magneto resistive material. With this kind of material, the magnetic characteristics change with any externally applied force. There are two approaches when designing tactile sensors using this kind of material. The first method is based on the principle that the movement of a small magnet by an applied force will cause a change in the flux density at the point of measurement and this observed change can then be measured using the Hall effect or by a magneto resistive device. The second method involves fabrication of the core of a transformer or inductor from a magneto resistive material that will become deformed under action of the pressure causing the magnetic coupling between the transformer windings to change. If a very small permanent magnet is held above the detection device by a compliant medium, the

change in flux caused by the magnet's movement due to an applied force can be detected and measured. Magneto resistive sensors have a number of advantages such as high sensitivity the dynamic range. Its major disadvantage is the nonlinearity [36].

### **1.5.5 Piezoelectric Sensors**

A Piezoelectric material may be defined as the material which produces charges when subjected to a mechanical deformation caused by mechanical stresses. It can also be defined as the material which undergoes a mechanical deformation when it is subjected to an electrical input. Any polymeric material that exhibits such piezoelectric properties is appropriate for use in tactile sensors [35-37].

Most Piezoelectric materials exhibit high stiffness comparable to steel. Therefore; deformations of sensing elements in the piezoelectric force sensors will be much smaller than in other measuring systems. Some of the properties of the piezoceramics are found in Piezo-electric polymers [35, 37]. One of the most popular piezoelectric polymers used in such applications with low dynamic operation is Polyvinylidene fluoride (PVDF). This is an ideal sensing material because of its responsiveness to a wide range of frequencies, relatively high mechanical strength, and its high sensitivity [8, 35, 37].

PVDF is available in sheets that range in thickness between 6 microns to 2 mm. Metallization is used to apply a thin layer of metal on both sides of the PVDF sheet to form electrodes and collect the accumulated charges. As previously mentioned, deformation caused by an external force results in an electrical charges which proportional to the applied force. This charge results in a voltage  $V= Q/C$ , where Q is the

output charge, and  $C$  is the capacitance [37]. A simple piezoelectric sensor structure is shown in Figure 1.13.

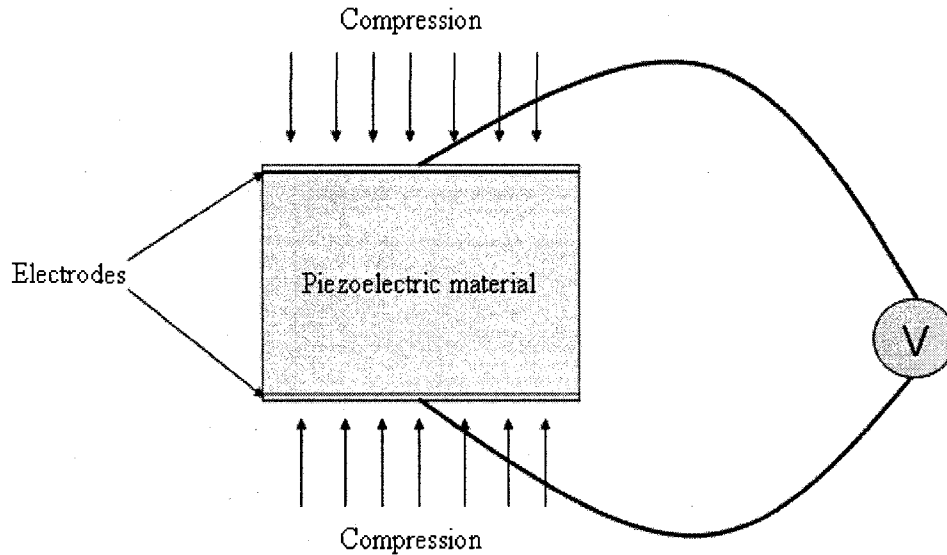


**Figure 1.13 - The basic principle of a piezoelectric sensor**

### **1.5.6 Comparison among the Different Technologies**

Optical technology exhibits many of the requirements of ideal tactile sensors, such as high resolution, high sensitivity, and immunity to electromagnetic radiation. But they suffer of some serious problems such as being very brittle and sensitive to vibrations in addition to the complicated associated signal processing.

Strain gauges have many of advantages as force sensors but their nonlinearity, instability and limited range does not make it an ideal choice for a tactile sensor, Moreover, silicon strain gauges are fragile and are difficult to align while gluing.

Capacitive sensors have a high level of sensitivity, compact size and mass and it is active on both static and dynamic loads but it displays a noise problem, has high impedance and temperature drift.

Magnetic sensors have high sensitivity and wide dynamic response range, but the complicated structure and its nonlinearity do not make it an ideal choice.

Piezoelectric technology utilizing PVDF film possesses several advantages over the other sensing technologies. PVDF film is light, rugged, and potentially low in cost. It can be prepared between 6 $\mu$ m to 2 mm in thickness and be formed into complex surfaces. PVDF exhibits an extremely large piezoelectric response, making it attractive for the design of highly sensitive sensors for use in a wide variety of applications. Recent state-of-the-art surveys suggest that piezoelectric principles have been the most attractive amongst researchers in the field of tactile sensors. PVDF films do not require any activation current which is evidently highly undesirable in medical applications. Piezoelectric polymers present an interesting avenue for the development of a tactile sensing system that could mimic the skin response of a human hand.

From the above comparison between various technologies, piezoelectric polymers appear to afford the best opportunity for the development of a competent tactile sensor displaying many of tactile information and mimicking the human skin. It is sufficient to say at this stage that piezoelectric polymers appear to offer many advantages over some of the other technologies.

## **1.6 Literature Review**

The field of this thesis is a combination of many fields. The research scope combines MIS sensory systems, tactile sensors in general and the micro-tactile sensors fabricated using MEMS technology. Many researches were proposed on the goal of improvement of each field, but there was less study that concentrated on integrating of all these three fields together to take full advantage of the scientific advances that have been made. The

following is a summary and discussion of previous works on the scope of integration of tactile sensing and MEMS technology in the field of MIS applications.

Bicchi et al. [38] have discussed capacitive tactile sensor with associated tactile display unit for use in MIS. By correlating force against deformation, the system was able to identify five objects of different elastic properties.

A series of designs for endoscopic and laparoscopic tools are discussed by Cohn et al. [39] who intend incorporating their tactile telepresence apparatus. An interesting idea raised here is the possibility of using the capacitive tactile sensor, not to measure applied force, but to detect the varying dielectric permittivity of different tissue. The study suggested that water, fat, blood vessels, and cancerous tissue might all be discriminated by this means.

An experiment with a sensor for laparoscopic attachment has been described by Fischer et al. [40]. A 64 point sensor of area  $1 \text{ cm}^2$  was connected to a fingertip vibrotaction display.

Silva et al. [41] developed a strain gauge type tactile sensor for measuring finger force. It was constructed using metallic strain gauges. It is rugged, has a linear response, good repeatability, resolution of 0.3 N, low hysteresis and sensitivity of 0.12 V/N.

Qasaimeh et al. [8] proposed a micromachined micro-tactile sensor. The sensor designed based on anisotropically etched silicon layer with tooth shape, and a microfabricated PVDF layer is sandwiched underneath. The sensor succeeded in finding the magnitude and the precise location of the contacting forces. It was also able to find the pressure distribution but it was unable to find out the contacting object's softness and was not adequately able to indicate any presence of embedded lumps.

Dargahi et al. [42] developed the prototype of tactile sensing system with only three sensing element “PVDF”. Magnitude and position of the applied force is obtained by using the triangulation approach combined with membrane stresses. The lack of agreement between theoretical and experimental results could be attributed both to the experimental errors and assumptions in the theoretical analysis.

Gray and Fearing et al. [43] had reported an array of micro-tactile capacitive sensors. The sensor was proposed for use on endoscopic-surgery tele-manipulator, and for the small-scale organic tissue sensing. The 8×8 tactile capacitive array sensors were used for detection of sub-millimeter features and objects, where the entire sensor array is smaller than the normal human spatial resolution of 1mm. The sensor has the capability of detecting mN’s force with good interpolation between elements. Although the sensors had no detectable proximity effects, they did have severe Hysteresis problems rendering the results unreliable.

Manish et al. [44] designed and fabricated a capacitive micromachined endoscopic tooth-like pressure sensor but it only measures a few grams of the applied force and was unable to measure the compliance of tissue.

Dargahi et al. [45] designed and fabricated a micromachined robust piezoelectric endoscopic tooth-like tactile sensor with good linearity and high dynamic response. The sensor, however, was unable to adequately indicate the presence of blood vessels, embedded lumps and the softness of grasped organs.

Reston and Kolesar [46] had constructed a 5×5 robotic tactile sensor based on piezoelectric Polyvinylidene fluoride (PVDF) film and coupled to an integrated circuit.

Although the array provided good linear output, its limited range and inability to measure contacting objects softness makes it a poor choice for a finger mount tactile sensor.

Germagnoli et al. [47] developed a finger tip  $8 \times 6$  array sensor sensitive to all six independent stress tensors by a careful orientation of the PVDF sensing elements. The sensor sensitivity is low and requires amplification close to the sensor to achieve an adequate signal-to-noise ratio.

Narayanan et al. [48] presented an interesting tactile sensor for use in endoscopic surgery. Sensing parts of the sensor was fabricated from PVDF layers. The sensing elements are sandwiched under two different kinds of coaxial cylinders. The first cylinder was rigid and surrounded by the second cylinder which is soft. The sensor has a good output and able to recognize the contacting tissues softness. But considering its several parts and the hard aligning and assembling, it is not considered a good candidate for batch manufacturing and commercial use. Moreover, the sensor is active just on the teeth regions; the other regions are inactive. The sensor failed to recognize loading with low magnitudes comparable to blood vessels pulse.

Dizaji et al. [49] developed a new cancer diagnostic approach by ultrasonic imaging of tissues, in which the tissue elasticity is measured and compared with the elasticity of normal tissues. The results of displacement estimation of normal and abnormal breast tissues under external stress are calculated using image registration technique. The work estimates not only the translation, but also the rotation and scaling parameters. The Young's modulus, calculated from displacement values, was then used to identify tissue characterization. The work also showed that the above-mentioned procedure can successfully detect abnormal tissues.

Obana et al. [50] designed a semiconductor strain gauge tactile transducer. It was designed with the goal of measuring finger force without affecting the hand dexterity. A semiconductor strain gauge was used because of its small size and high sensitivity, but it is also sensitive to high temperature. The transducer has both dynamic and static responses in which the Hysteresis is negligible and linearity is good. With a force sensitivity of 0.05 V/N, this sensor is ideal for measuring the force applied on the tissue but the problem is to find out the softness of tissue and to avoid tissue damaging.

Shinoda et al. [51] designed acoustic sensing matrixes which are placed face-to-face. The sensor used for mounting on robots finger with 5-D deformation. Sensor measured 10 $\mu$ m displacement by 18.5 mm cell height and 0.001 rad change in surface inclination. This sensor can measure contact force and as well as the slip of grasped object.

Ohka et al. [52] developed an optical tactile sensor equipped with optical wave guide plate and mounted on a robot manipulator. The experimental results confirmed that the tactile sensor is capable of detecting the distribution of a three axis force and both the calculated and experimental results coincide well. This tactile sensor comprised a CCD camera, light source, an acrylic board and a silicon rubber sheet that are assembled into casing so the feasibility of its being miniaturized is very low. Another new problem to overcome is to provide a light source with the endoscope.

An interesting work was presented recently by Sokhanvar et al. [53, 54]. A sensor of multifunction for minimally invasive surgery use was presented. The sensor was designed based on PVDF as the sensing material. An array of flexible beams was glued to a supporting channel. And the PVDF layers were attached to the beams and another were sandwiched between the beams and the channel. The sensor was able to detect the

applied force and position. The designed sensor succeeded in indicating the stiffness of the contacting object. The sensor alignments and assembling do not make it an ideal candidate for batch manufacturing and commercial use. The sensing range was restricted to Newtons which make it unable to detect the low magnitude contacting forces comparable to the blood vessels pulse. Moreover, the presented sensor is active only on the tooth shapes, and the other regions are inactive areas and cannot detect any tactile property.

Howe et al. [55] designed a capacitive tactile array sensor which is based on an earlier design of Fearing [56]. This device measures the pressure distribution at the contact between the robot hand and the grasped object. Experiments confirm the system's ability to convey significant contact information.

Payandeh et al. [57] designed a haptic interface for endosurgery. The design consists of tunable spring based on the haptic and surgical requirements. Simulation and experimental results demonstrated the practicality of such design concept.

Petter et al. [58] developed a new tactile measurement system, which is capable of differentiating between the hardness of various soft materials such as living tissues by measuring the mechanical frequency response of the tissue. It is intended to integrate this "vibrotactile sensor" inside the top of a tactile rod for endoscopic surgery in order to provide the surgeon with a substitute for the missing tactile feeling since locating arteries hidden beneath superficial tissue is a difficult task in MIS.

A membrane-based tactile sensor had been proposed by Golpaygani et al. in [24]; design and analysis of a tactile sensor for MIS applications was presented. Analysis of the design showed a relation between the applied load and the membrane deflection; also the

relation between contacting object stiffness and the deflection is derived. Study did not propose any kind of sensing criteria (such like piezoelectric or piezoresistive etc). Moreover; the designed sensor is active just on the mesa points, and the other points are dead and can not measure contacting objects properties and contacting forces. In addition; the presented sensor is not of a tooth shape, and unable to handle the soft slippery internal organs.

Ryan et al. [59] developed a system which can find the paths of arteries using tactile sensing in MIS. The surgeon begins by using the surgical robot to place the tactile sensor instrument on a known artery location. Signal processing algorithms locate the artery from it's pulsate pressure variation. The problems with compliance in the system result in occasional loss of the artery path. To perform MIS effectively, surgeons should be familiar with the quantitative assessment of the biomedical properties of soft tissues. Many different layouts were proposed and designed for examining the tissue behavior while performing minimal invasive surgery.

Yong ping et al. [60] developed an ultrasound indentation system with a pen-size hand held probe that is used to obtain the indentation responses of lower limb soft tissues. A linear elastic indentation solution was used to extract the effective Young's modulus that ranged from 10.4 to 89.2 kPa for soft tissues. The Young's modulus determined was demonstrated to be significantly dependent on site, posture, subject and gender. No significant correlation was established between the effective Young's modulus and the thickness of entire soft tissue layers.

A surgical instrument was recently presented by Dargahi et al. in [61], the instrument based on a former sensor design [48]. Microfabrications of the instrument and the

experimentations were presented. A graphical display method was used to detect embedded lumps inside tissues while surgery operations. The same disadvantages associated with [48] are associated with this medical instrument as well.

Recent studies have focused on the development and control of a micro-gripper based on flexure joints, fabricated by LIGA and instrumented with semiconductor strain gauge force sensors [62]. Strain gauge sensors located at the tip of the micro-gripper provide useful information for force control of the micro-gripper in biomedical applications.

Atkinson et al. [63] have fabricated a MEMS tactile sensor using a novel high temperature piezoelectric polyimide material which can measure the tactile information over a non-planar geometry. These devices have the potential to offer high temperature tactile sensor performance than that of a conventional fabricated sensor.

Tao Mei et al. [64] have developed a robust MEMS integrated three-dimensional tactile sensor with soft contact surface and large force range. The sensor uses an over-stop design to increase the robustness for overloading and has CMOS integrated piezoresistive sensing elements and on-chip data-reading circuitry to reduce total sensor volume.

The majority of tactile sensor technologies have focused on silicon based sensors that use piezoresistive [65, 66] or capacitive sensing [67, 68] and polymer-based approaches that use piezoelectric polymer films [48, 69] or strain gauges [70] for sensing.

Shinoda et al. [71] have developed ultrasonic emission tactile sensor that is capable of quick localization of touch and removal from touch, sensation of texture under movement and detection of precursor.

The Lord Industrial Automation (Covy, NC) [72] sensor is a commercially available optical force sensor. However, the sensors are too thick (28.4 mm) to be useful in finger-mounted applications.

Qasaimeh et al. [10] presented an optical tactile sensor based on optical fibers. Thin membranes deflected under action of contacting tissues which is then measured using optical method of reflections. The designed sensor was able to find the contacting forces magnitude, the pressure distribution, and the contacting objects softness. Because the sensor is based on optics, an optical source and receiver is required. Moreover, multiplexer and complicated computer processing is also required.

Suzuki et al. [73] developed a silicon tactile imager based on an array of capacitive cells. Samaun et al. [74] developed an early piezoresistive-pressure sensor which could be catheter mounted. Lee and Wise [75] developed a silicon capacitive pressure sensor. Tanigawa et al. [76] developed a silicon pressure sensor with on-chip signal processing. Kane and Kovacs report a tactile sensor capable of high-resolution imaging. The sensor uses a CMOS compatible process and can resolve both normal and shear stress. However, all of these sensors have a thin diaphragm and most target the problem of tactile imaging and are, therefore, unsuitable for measuring finger and hand forces in clinical applications.

## **1.7 Objectives and Scope of this Research**

As discussed earlier; during most MIS operations, the organs under surgery are soft and sensitive to any excessive force [8, 12]. Any undue force could be harmful and seriously damage the target organs and/or the surrounding tissues. The applied forces during the

surgery (such as grasping forces, cutting forces, palpation forces etc) must be monitored and controlled in a suitable safe range [10].

Palpation is a main step associated with any surgery. Generally, a surgeon will palpate organs to detect any abnormality and this plays a key role in any decision that the surgeon may make. With palpation, the surgeon will be able to recognize the softness of organs to determine any abnormal stiffness which could indicate the existence of tumors, the type of tumor (i.e. cancerous cells), and the value of this tumor contagion [2, 9, 12, 14-17]. During MIS operation with the tools inserted, palpation is not possible and the surgeon interacts with unknown objects. It makes the surgery more difficult and potentially more harmful [2, 9, 12]. To make the operation less invasive and minimize danger, the grasped organs softness has to be estimated and the abnormality must be detected.

Palpation is also important in order to detect embedded lumps which are the abnormal growth of some cells inside the organ and could be an indicator of disease. In general, embedded lumps are harder to detect than determining organ tissue stiffness [14-17]. While grasping organs, the embedded lump reaction on graspers is acting as a concentric force, and the rest of organ reaction will act as small uniform pressure distributions on the grasper [77]. For that reason, the MIS tools should be able to find out the precise position of any concentric load while grasping the organ.

Blood vessels inside snatched organs can cause significant problems during surgery because of bleeding that could occur during cutting or hard grasping. Locating the vessels and arteries inside an organ to determine pulsating rate is important for the surgeon [2, 15] who would, therefore, be appreciative if the inserted graspers are also able to detect the blood vessels pulse.

For gentle loading on the tissues while grasping, and for appropriate handling ability of slippery soft tissues while grasping, lifting, and twisting, a tooth like grasper must be considered. Since most tactile sensors are integrated with the grasper jaws, and come into direct contact with internal objects, the sensor itself has to have a corrugated shape [8, 19, 45]. In the case of a soft slippery grasped tissue, a high grasping force is forbidden, but twisting while grasping in some cases could be required in which case it is preferred that the corrugated shape be on both the width and length of the sensor.

In conclusion, the objectives of this research are to investigate a new tactile sensor for MIS applications which has cheap manufacturing costs, biocompatibility, and the ability to integrate with the available commercial endoscopies. The desired properties of the ideal sensor are:

1. Ability of finding magnitude of the distributed grasping forces.
2. Ability of estimating the grasped organs softness.
3. Ability to detect the presence of any embedded lumps.
4. Ability of blood vessels pulse detection.
5. A tooth-like shape of the sensor on both directions; the length and the width.

The following chapters are introducing the tactile sensor design, analyzing and simulating the sensor using Finite Element method software (ANSYS 10), addressing and discussing the sensor microfabrications and assembly, and finally the sensor is experimentally characterized and the results are reported.

## **Chapter 2 – Sensor Design**

One of the major goals of this research is to put forward a good sensor with cheap costs and simple structure. Cheap cost makes it a disposal part of the MIS tools [9], and its simple structure enables simple batch fabrications, commercial use and simple data processing.

Silicon is a good choice for such a desired application. Using MEMS technology, it is simple to fabricate in batches which reduces manufacturing costs, it is biocompatible with internal organs, and it is a very good material in compression [12, 53]. Moreover, a thin silicon layer is deformable with good strength.

PVDF is a known sensing element in the tactile sensing field. It is cheap compared to other piezoelectric materials; it is biocompatible and is well-matched with the MEMS technology to fabricate electrodes for charge collecting [53].

The proposed sensor is assembled using three layers. The first layer is micromachined from a silicon wafer. The second layer is the sensing element and it is fabricated from Polyvinylidene fluoride (PVDF). Finally all of the structure is supported by a third layer of Plexiglas. The following sections present the design details of each layer and the sensor sensing principle.

### **2.1 Tooth-Like Silicon Layer**

The first layer is a layer of micromachined silicon wafer and is microfabricated to form the required teeth shapes on the top, to form a deformable base plate on the middle, and finally to form a U-Channel shape with two supports on the bottom. All of those features

are fabricated in one step and on one silicon layer. The designed teeth on the top are necessary for object grasping associated with any grasper. The middle base plate is designed to give a deformation under grasping action, and the supports hold the base plate and give a suitable gap which is necessary for the plate deflection. Structure of the micromachined silicon layer is shown in Figure 2.1. Properties of the silicon wafer which is used on this sensor design are discussed on Table 2.1.

**Table 2.1 - Properties of Silicon wafer [78]**

Property	Value
Type	n- type (100)
Young's Modulus (GPa)	130
Density (g/cm <sup>3</sup> )	2.34
Poissons Ratio	0.28
Thickness (mm)	0.5

The silicon layer is 30 mm in length with a width of 15 mm and the supports width is 2.5 mm for each. The thickness of the base plate is 100  $\mu\text{m}$ , and the height of the supports is 200  $\mu\text{m}$  making a gap of the same height for deflections. These dimensions are shown in Figure 2.2.

Each Tooth has a uniform trapezoidal shape with a height of 200  $\mu\text{m}$ . The top of the trapezoid is a square of 2 mm on each side. The other dimensions of the trapezoid are restricted by the previous two dimensions and the specifications of the silicon planes. For the microfabricated silicon layer, the planes  $\{111\}$  are oriented to be on the side wall of

the trapezoidal shapes, each plane {111} has an incline of  $54.74^\circ$  with the XY plane. The dimensional specifications of the microfabricated silicon layer are shown in Figure 2.3.

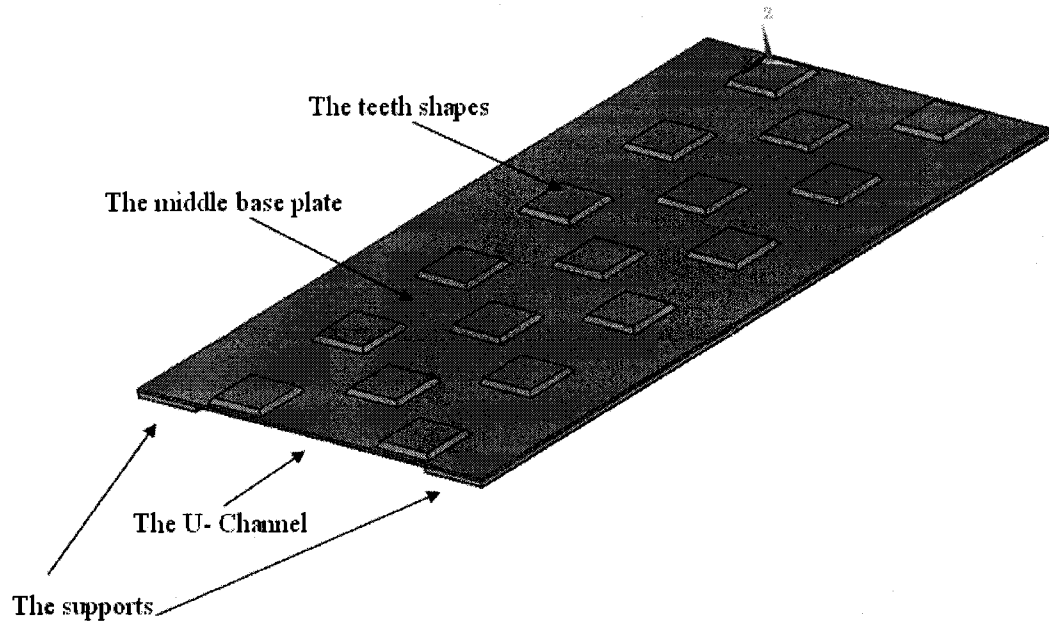


**Figure 2.1 - The micromachined silicon layer**

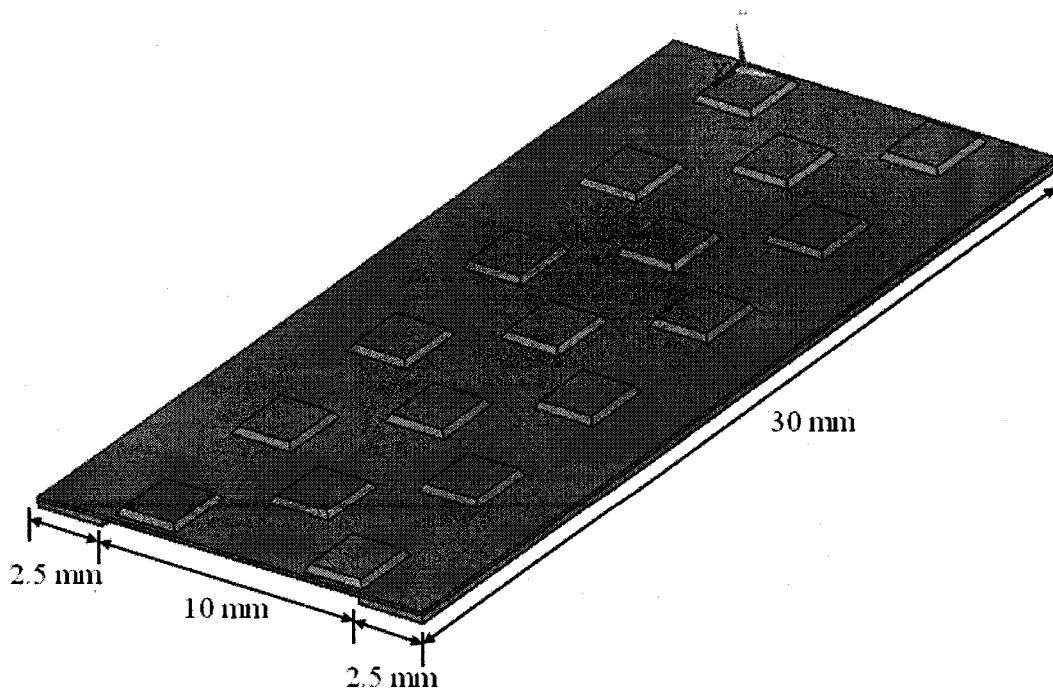


**Figure 2.2 - Dimensions of the silicon layer**

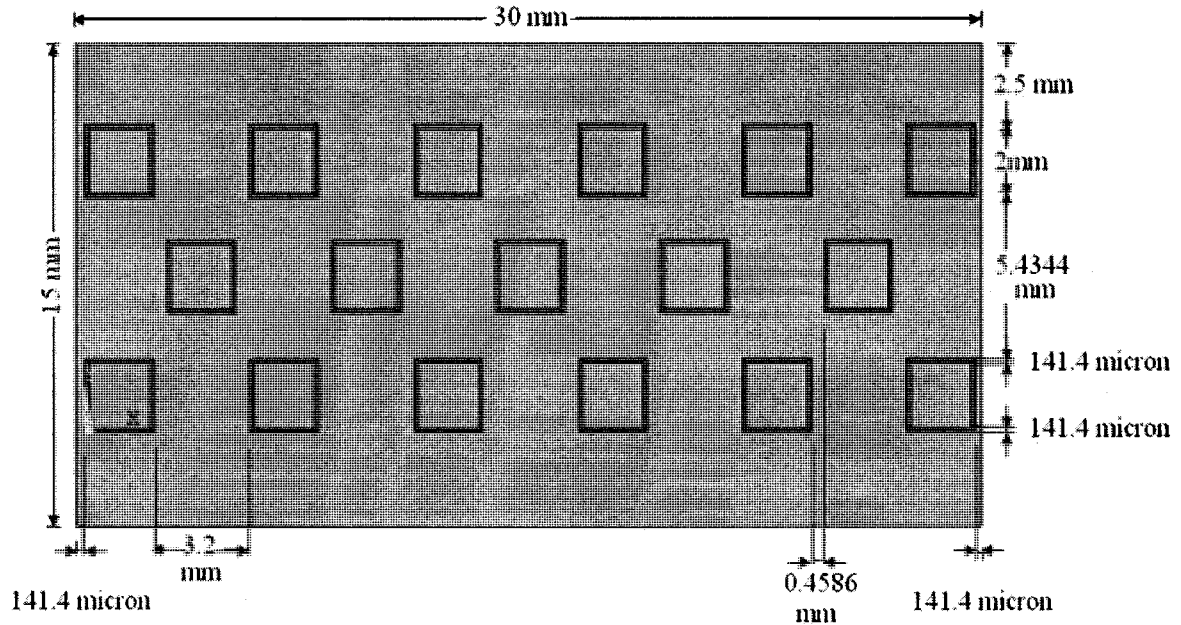


**Figure 2.3 - The microfabricated silicon layer specifications**

## 2.2 Sensing Elements

As mentioned previously, the second layer of the sensor is microfabricated from PVDF films to create the sensing elements of the sensor. PVDF layers used in this sensor design are metalized and poled piezoelectric PVDF film with a thickness of 25  $\mu\text{m}$ . The used PVDF film is a uniaxial PVDF film; the uniaxial film is the result of mechanical drawing of the film in one direction. This direction is called the drawn direction or referred to as the 1-axis which has the highest piezoelectric coefficient. The three perpendicular directions 1, 2 and 3 which are called drawn, transverse and thickness directions, respectively, are shown in Figure 2.4.

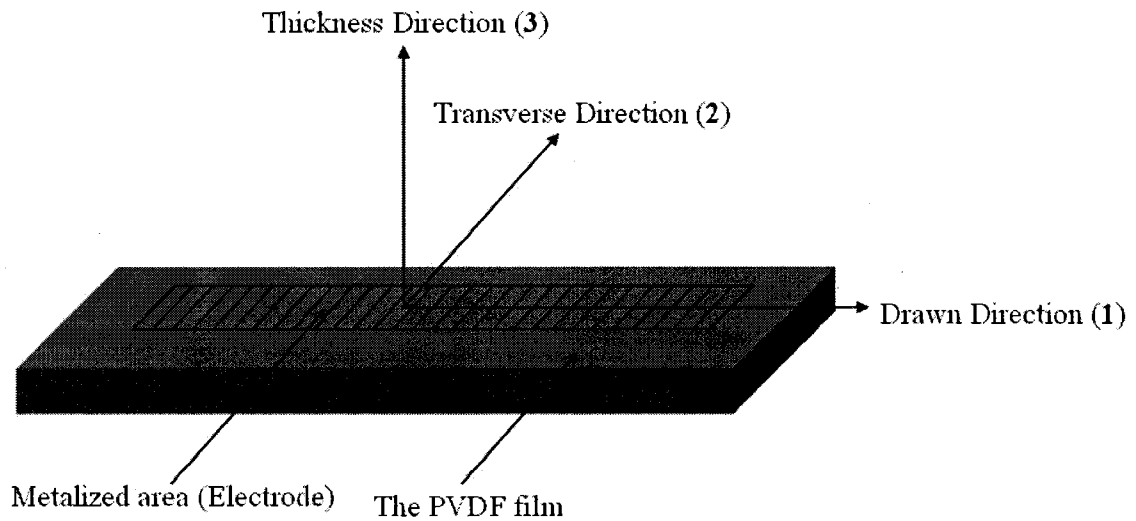


**Figure 2.4 - The main three directions of a uniaxial PVDF film**

The details of the piezoelectricity property are discussed in Appendix A1 at the end of this thesis. Table 2.2 discusses the property of the PVDF films used in this sensor design. The first part of the PVDF works on the extensional mode and is glued to the back of the base plate on the bottom of the U- Channel. In the case of plate deflection, the glued PVDF will stretch and produce an output voltage. The second part of the PVDF works on the thickness mode and is sandwiched between the two supports of the silicon and the supporting Plexiglas layer. When any force is exerted on the silicon layer, the PVDF will compress and produce an output voltage.

A cross-sectional view (not to scale) of the first two layers assembly in Figure 2.5 shows the PVDF layers locations at middle and supports. The middle PVDF layer is  $30 \times 10 \text{ mm}^2$  in length and width respectively and the PVDF layers at supports are each  $30 \times 2.5 \text{ mm}^2$  in length and width respectively. At the microfabrication stage, both middle PVDF layers

and supports will be microfabricated from one PVDF layer with a single common electrode and special pattern. These issues are discussed in following chapters.

**Table 2.2 - Properties of Polyvinylidene fluoride (PVDF) Film [78]**

Property	Value
Young's Modulus (GPa)	3
Density ( $\text{g/cm}^3$ )	1.76
Poissons Ratio	0.35
Thickness ( $\mu\text{m}$ )	25
Piezo Coefficient – d31 (pC/N)	18-20
Piezo Coefficient – d32 (pC/N)	2
Piezo Coefficient – d33 (pC/N)	$\approx -18$
Piezo Coefficient – g31 (Vm/N)	0.15
Piezo Coefficient – g32 (Vm/N)	0.015
Piezo Coefficient – g33 (Vm/N)	$\approx -0.15$

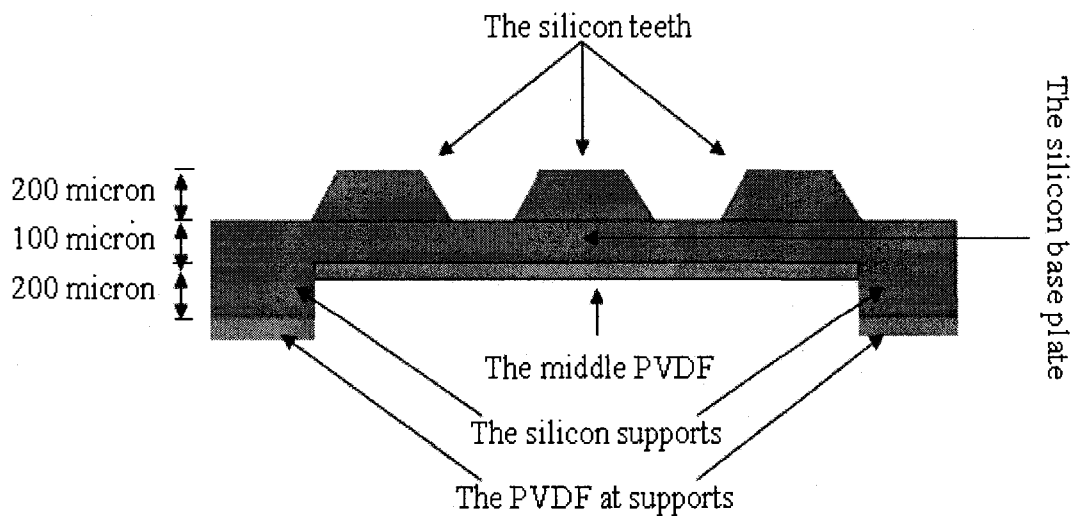


**Figure 2.5 - A cross-sectional view of the assembled silicon and PVDF layers**

### 2.3 The Sensor Assembly

The third layer consists of Plexiglas having  $30 \times 15 \times 2 \text{ mm}^3$  dimensions for length, width, and thickness respectively. Plexiglas is a biocompatible material and it is used to support the first two layers of the sensor and to be the connection layer with the commercial endoscope tool while assembling. The complete assembly of the proposed tactile sensor is shown in Figure 2.6.

The designed sensor will be integrated with one jaw of the endoscopic grasper. The second jaw is integrated with an additional etched silicon layer having the opposite shape of the teeth arrangement of the tactile sensor. That helps for better grasping and gentle pressure distribution on the grasped tissues/object. The proposed tactile sensor is integrated with an endoscopic grasper and is shown in Figure 2.7.

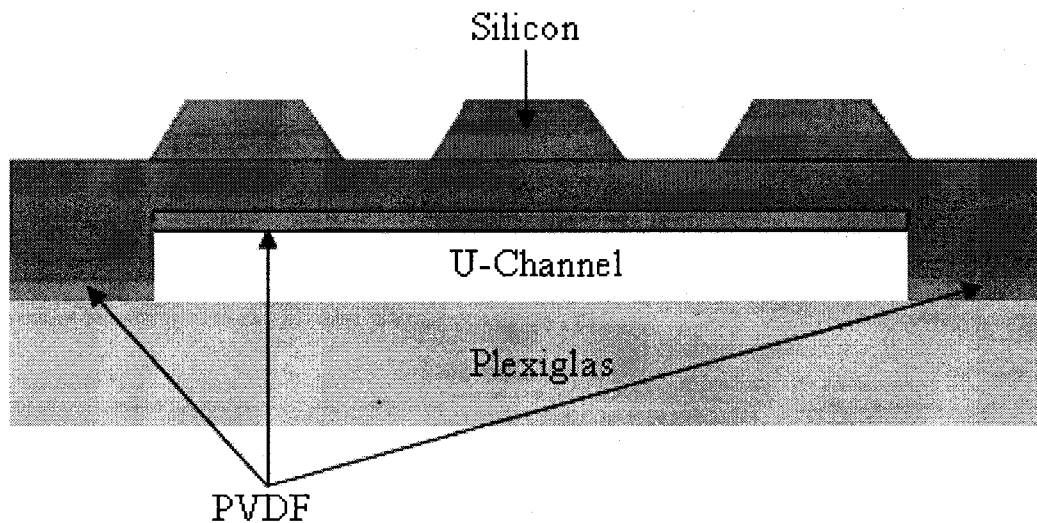


**Figure 2.6 – Cross-section of the proposed tactile sensor**

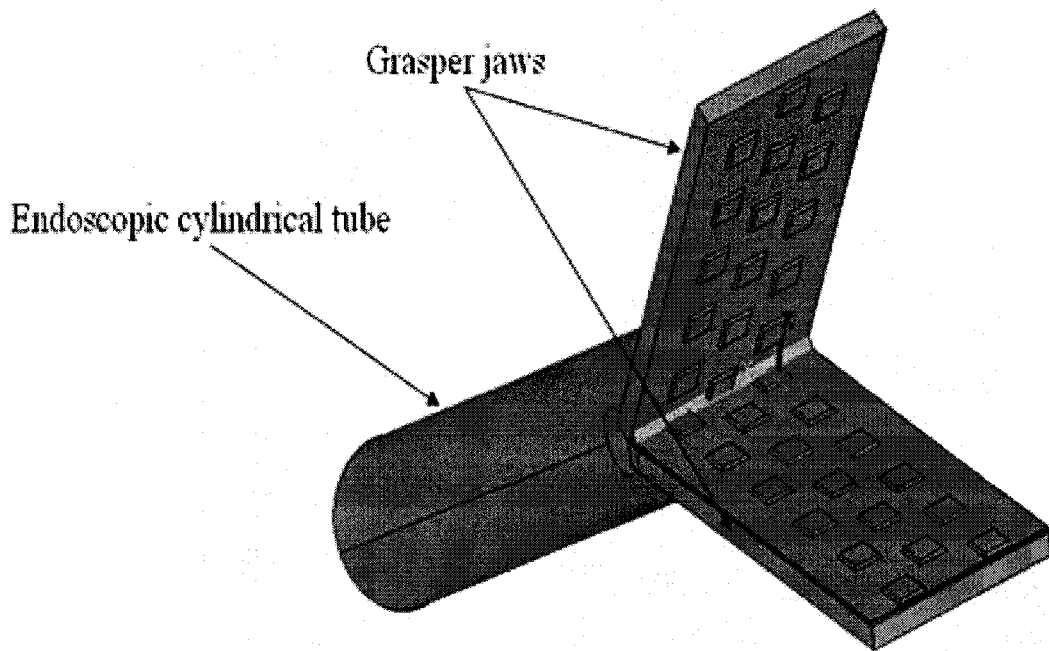


**Figure 2.7 - Endoscopic grasper integrations with the proposed sensor**

## **2.4 Closed Form Analysis of the Sensor**

As discussed in previous sections, there are two sensing layers located at two different locations. The first is the sensing layer at supports which is sandwiched between the silicon supports and the Plexiglas supporting layer. The second is the middle sensing layer which is glued to the back of the base plate.

The sensing layer at support has three functions. It determines the grasping force magnitude, locates any embedded lumps and indicates the pressure distributions along the grasped tissue. The middle sensing layer determines the grasped tissue softness, detects the blood vessels pulse and indicates any abnormal stiffness along the grasped tissue.

### 2.4.1 Sensing Elements at Supports

While grasping internal organs, a compression force will be transferred to the PVDF layers at support via the silicon layer and works on its thickness mode resulting in an output voltage to the electrodes. For greater compression loads, the PVDF layer will be compressed more resulting in a higher magnitude of voltage.

Because the silicon layer has two supports, and using simple mechanics principles, we can predict the applied load which is carried by these two supports. Depending on the pressure distributions and the concentric load locations, the load will be carried equally on both supports, or one of the supports will carry more than the other.

To prove the principle, a fixed-fixed simple beam with applied point load is considered as shown in Figure 2.8.

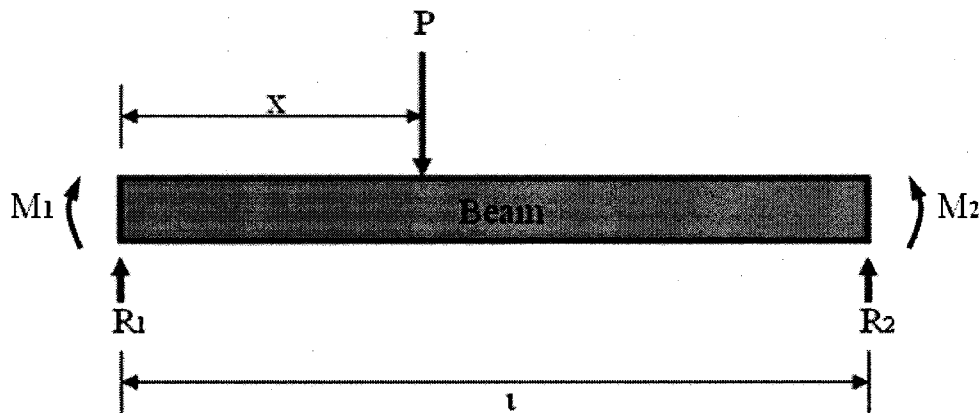


**Figure 2.8 - A simple fixed-fixed beam with point load application**

The point load ( $P$ ) is applied at a distance ( $x$ ) on the beam of length ( $L$ ). Two reactions,  $R_1$  and  $R_2$ , and two moments,  $M_1$  and  $M_2$ , appear at the fixed points of the beam. Magnitudes of both  $R_1$  and  $R_2$  are a function of  $x$ , and the summation of both is equal to the load magnitude ( $P$ ). Because the system is at static equilibrium, by applying

summation of forces and moments equal to zero [79], we can find the values of  $R_1$  and  $R_2$  from the following:

$$R_1 = \frac{P(\ell^3 - 3\ell x^2 + 2x^3)}{\ell^3} \quad (1)$$

$$R_2 = \frac{P(3\ell x^2 - 2x^3)}{\ell^3} \quad (2)$$

By plotting both equations versus the point load location, the relation is shown clearly and the principle of the point load detection is valid. Magnitudes of reactions versus the point load location are shown in Figure 2.9.

As discussed in section 1.7, the reaction of embedded lumps on the silicon plate is similar to a point load. Detecting the point load will indicate the presence of any embedded lump and determine the precise location.

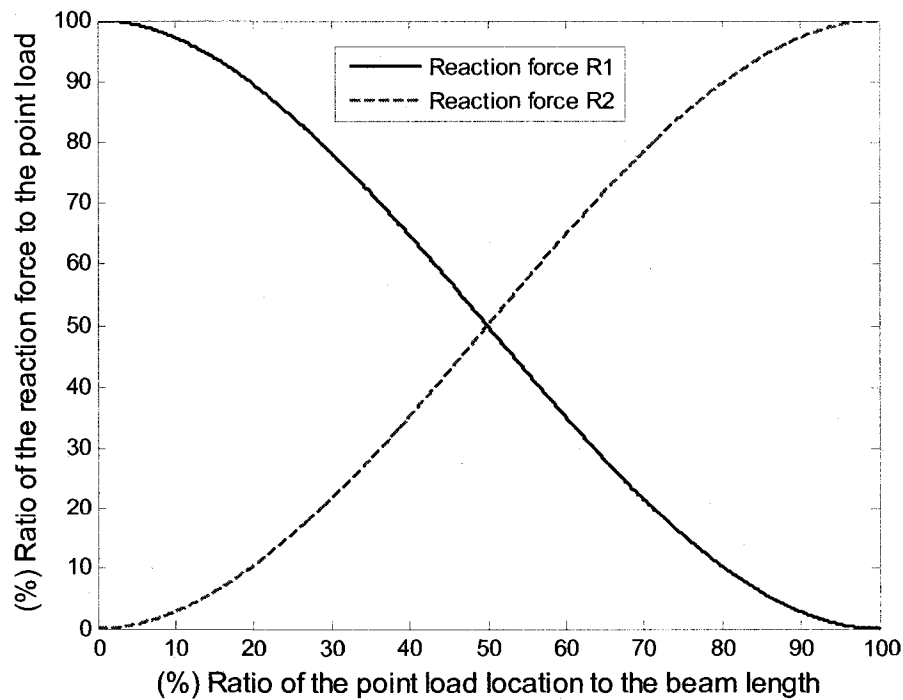


**Figure 2.9 - Reaction magnitudes as a function of the point load location**

The output voltage at each PVDF sensing element corresponds to the load carried by these two supports and, by comparing these output voltages, any embedded lumps will be located. The summation of these output voltages will indicate directly the total grasping load and, by calibrating this summation with the applied compression forces, the grasping force can be measured.

To find the grasping pressure distributions along the grasped tissue, an array of sensing elements must be considered. The PVDF layer at each support is fabricated to have an array of separated sensing elements and this is discussed later-on in the geometrical analysis and fabrication sections.

#### **2.4.2 Sensing Elements at Middle**

The middle sensing layer is a PVDF layer working on its extensional mode while deflection of the base silicon plate will cause the PVDF layer to stretch and supply an output voltage. This sensing layer is responsible for determining tissue softness and to find and respond to any low magnitude loading comparable to the blood vessels pulse.

Because the silicon layer is very thin, it is sensitive to any loading magnitude. While loading even small magnitudes, a deflection on the thin plate will occur and cause the glued middle PVDF layer to stretch. Because the PVDF layer is working on its extensional mode, the stretching caused by any small loading (comparable to the blood vessels pulse) creates a detectable voltage.

The silicon layer deflection is related to the softness of the contacting tissue. In the case of contacting soft tissue, the silicon will yield to a large deflection, in proportion to the large stretching of the PVDF layer, and produce a high voltage. On other hand, in the

case of contacting hard tissue, the silicon layer will only be slightly deflected with correspondingly less stretching of the PVDF giving rise to only a small voltage.

Abnormal stiffness along the grasped tissue can be found if the middle PVDF has an array of sensing elements. In the case of stiffness abnormality (i.e. half of the tissue is hard and the other half is softer), the deflection of the silicon base plate will not be uniform and neither will the stretching on the PVDF layer. This will cause the output voltage at some regions to become higher than others. The middle PVDF layer is fabricated to have an array of separated sensing elements. This array is discussed later at the geometrical analysis and microfabrication sections.

To prove that softer contacting tissue causes larger deflection of the silicon, and harder tissue causes smaller deflection, the following assumptions are made to simplify the problem;

1. A simple fixed-fixed beam with a contacting tissue will be considered.
2. With our analysis, geometrical properties of the system are constant, as well as for the material properties. The contacting tissue has the same length and width of the beam, but it is much thicker.
3. A uniform distributed load will be applied on the contacting tissue.

The model is shown in Figure 2.10. After the force application, the system will be deflected with a specific radius of curvature ( $R$ ). The magnitude of  $R$  is a function of the applied load, the resultant modulus of elasticity of the system, and the resultant second moment of inertia.

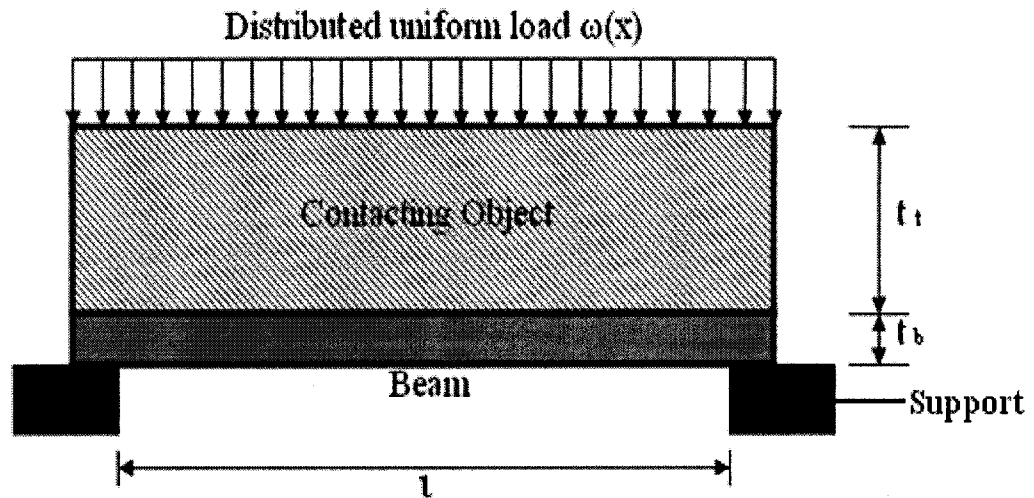


Figure 2.10 - A simplified model of the sensor consists of a simple beam and contacting tissue

The neutral axis (N.A) will be located in some position in the tissues layer because it is the thicker (assumption 3), so it will locate at a distance (c) upper than the contacting surface of the beam and tissue. The deflected system is shown in Figure 2.11.

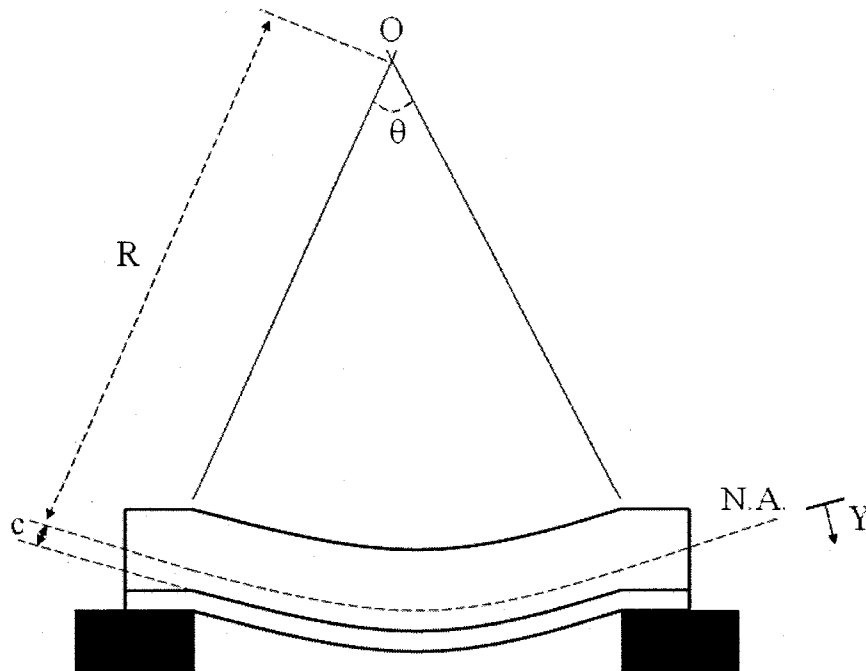


Figure 2.11 - Geometry of the model while deflection caused by a load action

Using the simple principles of material mechanics [79], the axial strain of the silicon beam is defined by:

$$\varepsilon_x = \frac{\delta\ell}{\ell} \quad (3)$$

Using the geometry in Figure 2.11:

$$\frac{\delta\ell}{\ell} = \frac{y\theta}{R\theta} \quad (4)$$

That's lead to have the axial strain on x-axis to be:

$$\varepsilon_x = \frac{y}{R} \quad (5)$$

Using Hook's law [79], the stress in x-axis is:

$$\sigma_x = \varepsilon_x E \quad (6)$$

Bending moments for a symmetric beam in pure bending [79] is:

$$M_z = \int -y\sigma_x dA \quad (7)$$

$$M_z = \int -y\varepsilon_x E dA \quad (8)$$

$$M_z = \frac{-b}{R} \int E y^2 dy \quad (9)$$

For the system of the beam and the contacting tissue, there is a total bending due to the tissue ( $M_{z1}$ ), and a total bending due to the beam ( $M_{z2}$ ).

The total bending due the tissue is:

$$M_{z1} = \frac{-b}{R} \int_{-(t_1-c)}^c E_t y^2 dy \quad (10)$$

By integrations with the given limits

$$M_{z1} = \frac{-bE_t}{3R} y^3 \Big|_{c-t_t}^c$$

$$M_{z1} = \left( \frac{b(c-t_t)^3 - bc^3}{3R} \right) E_t \quad (11)$$

The total bending due the beam is:

$$M_{z2} = \frac{-b}{R} \int_c^{t_b} E_b y^2 dy \quad (12)$$

By integrations with the given limits

$$M_{z2} = \frac{-bE_b}{3R} y^3 \Big|_c^{t_b}$$

$$M_{z2} = \left( \frac{bc^3 - bt_b^3}{3R} \right) E_b \quad (13)$$

The total bending of the whole system is:  $M_z = M_{z1} + M_{z2}$

$$M_z = \left( \frac{b(c-t_t)^3 - bc^3}{3R} \right) E_t + \left( \frac{bc^3 - bt_b^3}{3R} \right) E_b \quad (14)$$

One equivalent composite beam with equivalent modulus of elasticity ( $E_{eq}$ ) and equivalent second moment of inertia ( $I_{eq}$ ) can be considered. Because the tissue is much

thicker than the beam (assumption 3), we can consider the thickness of the equivalent beam equals to the tissue thickness, as shown in Figure 2.12.

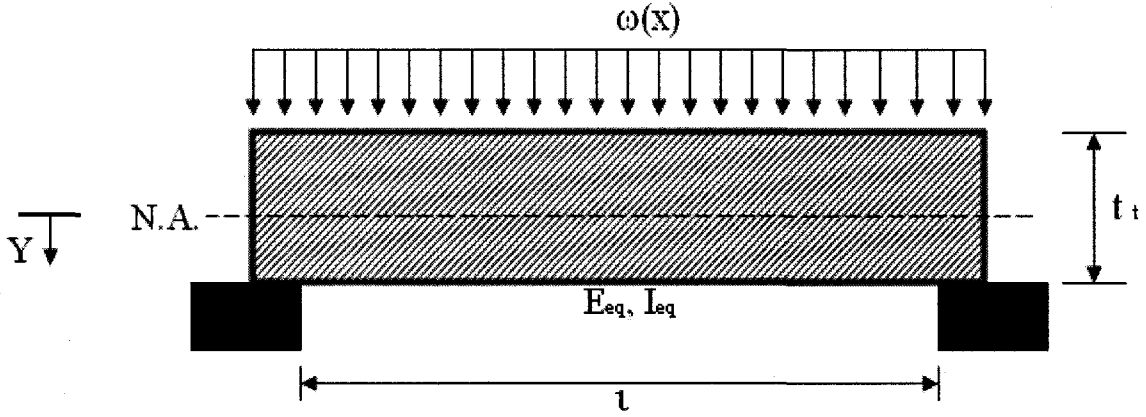


Figure 2.12 - The equivalent composite beam

The total bending ( $M_Z$ ) on the composite beam is:

$$M_Z = \frac{-b}{R} \int_{-\frac{t_t}{2}}^{\frac{t_t}{2}} E_{eq} y^2 dy \quad (15)$$

$$M_Z = \frac{-bt_t^3}{12R} E_{eq} \quad (16)$$

To find the equivalent modulus of elasticity of the composite beam, we substitute the total bending ( $M_Z$ ) of the system (Equation 14) equal to the total bending ( $M_Z$ ) of the composite beam (Equation 16), as shown in the following:

$$\left(\frac{b(c-t_t)^3 - bc^3}{3R}\right)E_t + \left(\frac{bc^3 - bt_b^3}{3R}\right)E_b = \frac{-bt_t^3}{12R} E_{eq}$$

By rearrangements' of the equation, we have:

$$E_{eq} = \frac{4bt_b^3 - 4bc^3}{bt_t^3} E_t + \frac{4c^3 - 4b(c - bt_t)^3}{bt_t^3} E_b \quad (17)$$

Based on assumption number 2, the geometry of the whole system is constant and will not be changed. Moreover, the modulus of elasticity of the beam is constant and the tissues modulus of elasticity is variable, so by substituting that:

$$C_1 = \frac{4bt_b^3 - 4bc^3}{bt_t^3} \text{ and } C_2 = \frac{4c^3 - 4b(c - bt_t)^3}{bt_t^3} E_b; \text{ where } C_1 \text{ and } C_2 \text{ are constants.}$$

So the equivalent modulus of elasticity (Equation 17) will become as:

$$E_{eq} = C_1 E_t + C_2 \quad (18)$$

It is clear from the last equation; that if the modulus of elasticity of the contacting tissue ( $E_t$ ) is increased, then the equivalent modulus of elasticity ( $E_{eq}$ ) will be increased. Also if  $E_t$  is decreased, then  $E_{eq}$  will be decreased as well.

Because the tissue is much thicker than the beam (assumption 3), and because the second moment of inertia is just a property of geometry; the equivalent second moment of inertia can be assumed as the second moment of inertia of the contacting tissue.

$$I_{eq} = I_t = \text{Constant} \quad (19)$$

Deflections of the equivalent composite beam under a distributed force action are given by [79]:

$$EI \frac{d^4 y}{dx^4} = -\omega(x) \quad (20)$$

For the fixed-fixed beam, we have the following boundary conditions:

$$y(0) = y(\ell) = 0$$

$$\left. \frac{d y}{d x} \right|_{x=0} = \left. \frac{d y}{d x} \right|_{x=\ell} = 0$$

By integration and considering the boundary conditions, we have the deflection as:

$$y = -\frac{\omega(x)x^2}{24E_{eq}I_{eq}}(\ell - x)^2 \quad (21)$$

If we consider any point on the beam (i.e. middle point), and by substituting the equivalent modulus of elasticity and the equivalent second moment of inertia (Equation 18) into the deflection of the middle point of the beam, finally we have:

$$y = \frac{-\omega(x)\ell^4}{384I_t(C_1E_t + C_2)} \quad (22)$$

Again, because the geometry and the load are constants, we substitute that:

$$C_3 = -\omega(x)\ell^4, C_4 = 384I_tC_1, \text{ and } C_5 = 384I_tC_2; \text{ where } C_3, C_4 \text{ and } C_5 \text{ are constants.}$$

Finally, we have the deflection of the beam as a function of constants related to the system geometry, and related to one variable related to the contacting tissue softness, as shown in the following equation:

$$y = \frac{C_3}{C_4E_t + C_5} \quad (23)$$

As it is shown, larger values of contacting tissue modulus of elasticity ( $E_t$ ) mean lower values of the silicon layer deflection. And smaller values of  $E_t$  mean higher values of the beam deflection. The constants  $C_3$ ,  $C_4$  and  $C_5$  are depending on the system geometry and the beam modulus of elasticity, the deflection of the beam for assumed values of these constants as a function of the tissue modulus of elasticity is shown in Figure 2.13.

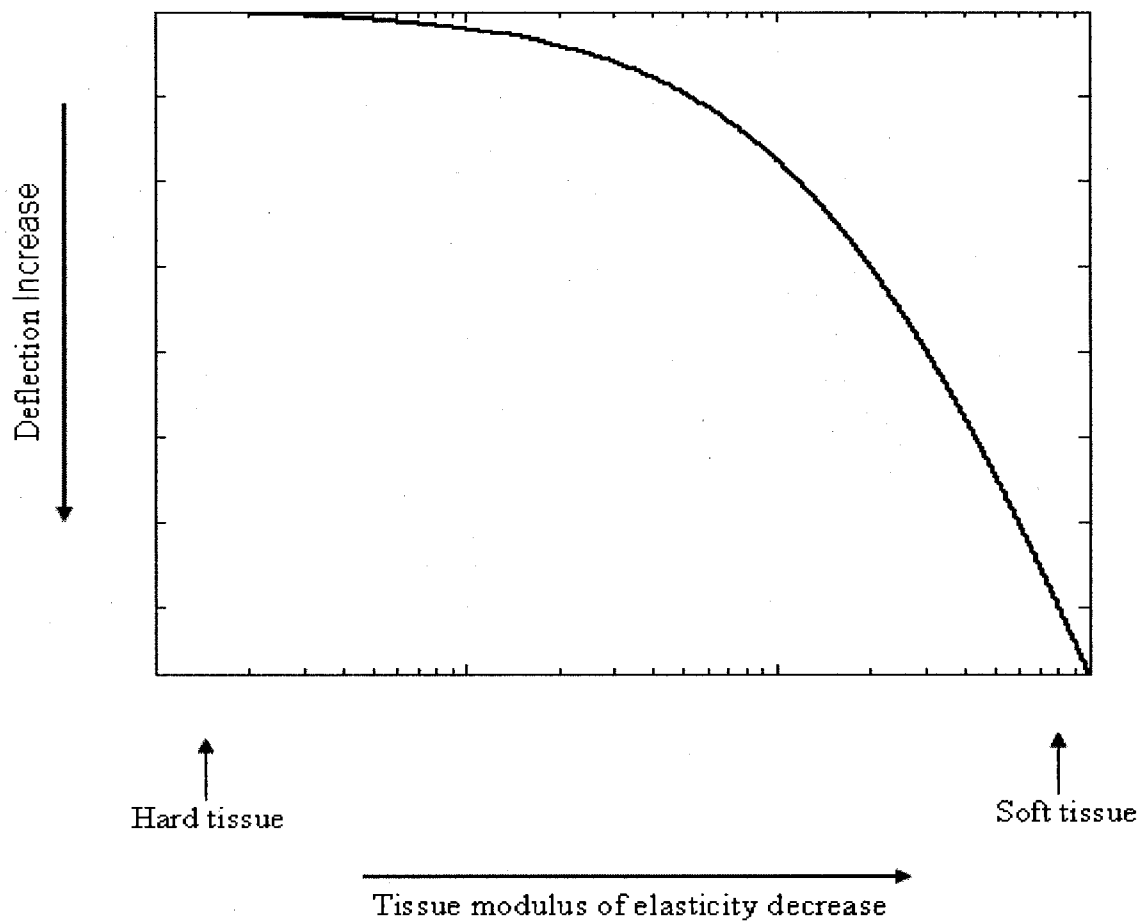


**Figure 2.13 - Deflection of the beam versus the object softness**

After presenting of the sensor design and the principle of its work on this chapter, the following chapter is going to discuss the finite element modeling and analysis of the

design. Moreover, simulations are going to be carried out with different loading and boundary conditions to verify the sensor functions and performance. Sensor parametrical study and geometrical analysis are discussed as well.

## **2.5 Summary**

In this chapter, the sensor's design is discussed. Dimensions and specifications of each layer are explained; specifications of the silicon layer due to the silicon planes are discussed in order of the teeth forming. Dimensions and locations of the PVDF layers are designed in order of satisfying the sensor functions. Assembly of the silicon layer with the PVDF layers together is discussed, and finally its congregation with a layer of Plexiglas is reported. Integration of the proposed sensor with MIS tool such as endoscopic jaws is addressed as well. Using a simplified model of the sensor, and a few assumptions; principles of the sensor functions are analytically verified.

## Chapter 3 – Finite Element Analysis of the Sensor

This chapter is divided into four sections. The first section deals with the finite element analysis of the proposed sensor using ANSYS 10 software. The second section illustrates a parametric study of the sensor dimensions. The third section discusses the geometrical analysis of the corrugated silicon shapes and sensing elements distribution. The last section discusses the results of simulations run for different loading conditions.

### 3.1 Sensor Modeling

The proposed sensor is modeled and analyzed using ANSYS version 10, Finite Element analysis software. It is used to construct a complete physical model of the sensor and the contacting object. This model is used to determine the deformation of the sensor and the output voltage at PVDF layers for different loading conditions.

While using ANSYS software, all of the operations are performed using sequential steps as shown in Figure 3.1. ANSYS software can be used in either the programming mode or the graphical mode [80]. The graphical mode is used in this research.

**Preference** is the first step of ANSYS and is used to describe the nature of the problem and to decide the method to be used for its solution. For this sensor analysis, the problem is a coupled field structural modeling. Different modules are available for performing the analysis such as **h** or **p** methods [80]. For this analysis, the **h** method is used.

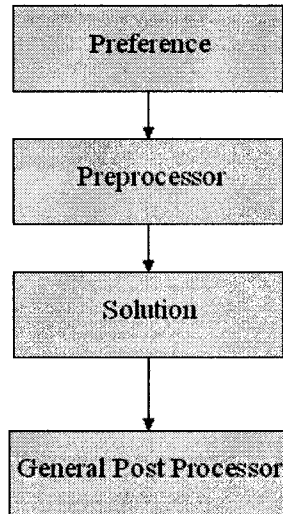


**Figure 3.1 - Sequence of ANSYS steps**

The **Preprocessor** is the next step and is the main body of the problem modeling. At this stage; many steps are included; such as defining the element type and material properties as well as the real constant. In this section of modeling, the first thing to be defined is the element types and its material properties [80]. This sequence is shown in Figure 3.2.

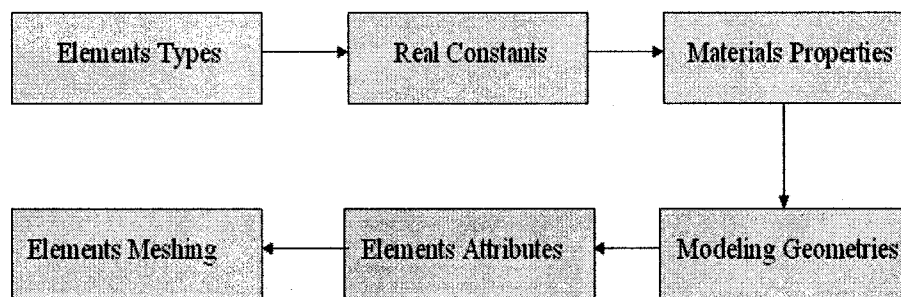


**Figure 3.2 - Sequence of Preprocessor steps**

The silicon layer is modeled using SOLID45 element which is used for the 3-D modeling of the solid structures. It is defined by eight nodes having three degrees of freedom at each node: translations in the nodal X, Y, and Z directions. SOLID45 element has

plasticity, creep, swelling, stress stiffening, large deflection, and large strain capabilities [81]. There are different choices to model the silicon layer, using different element types of higher orders, such as SOLID95, SOLID185, SOLID186 and SOLID187. Considering the available ANSYS version, SOLID45 was chosen to model the silicon layer, because its ability to model the silicon precisely and it has the lower number of nodes, where the available ANSYS version can support that number of nodes.

SOLID227 is used for the PVDF layers modeling and is used to model the 3-D Coupled-Field solid structures. It has strong capabilities when dealing with problems pertaining to Structural-Thermal, Piezo-resistive, Piezo-electric, Thermal-Electric, Structural-Thermoelectric and Thermal-Piezoelectric. SOLID227 element has ten nodes with up to five degrees of freedom per node. Structural capabilities are elastic only and include large deflection and stress stiffening [81]. There are different choices to model the PVDF layer, using different element types of higher or lower orders, such as SOLID5, SOLID62, SOLID98 and SOLID226. Considering the maximum number of allowed nodes with the available ANSYS version, and the required capabilities, SOLID227 was chosen.

More details of justification of the proposed choices of choosing the elements are described in [82].

The coupling method which has been used is the Strong (simultaneous, full) coupling method, where the general matrix equation is given by the form [83]:

$$\begin{bmatrix} [K_{11}] & [K_{12}] \\ [K_{21}] & [K_{22}] \end{bmatrix} \begin{Bmatrix} \{X_1\} \\ \{X_2\} \end{Bmatrix} = \begin{Bmatrix} \{F_1\} \\ \{F_2\} \end{Bmatrix} \quad (1)$$

The coupled effect is accounted for by the presence of the off-diagonal sub-matrices, [K12] and [K21].

The matrix equation for the SOLID227 element as a piezoelectric element is given by the form [83]:

$$\begin{bmatrix} [M] & [0] \\ [0] & [0] \end{bmatrix} \begin{Bmatrix} \{\ddot{u}\} \\ \{\dot{V}\} \end{Bmatrix} + \begin{bmatrix} [C] & [0] \\ [0] & [0] \end{bmatrix} \begin{Bmatrix} \{\dot{u}\} \\ \{V\} \end{Bmatrix} + \begin{bmatrix} [K] & [K^Z] \\ [K^Z]^T & [K^d] \end{bmatrix} \begin{Bmatrix} \{u\} \\ \{V\} \end{Bmatrix} = \begin{Bmatrix} \{F\} \\ \{L\} \end{Bmatrix} \quad (2)$$

Where:

$$\begin{aligned} \{F\} &= \{F^{nd}\} + \{F^{th}\} + \{F^{ac}\} + \{F^{pr}\} \\ \{L\} &= \{L^{nd}\} + \{L^C\} + \{L^{SC}\} \end{aligned} \quad (3)$$

The material properties are defined in Sections 2.1 and 2.2, together with the mechanical and electrical properties of the silicon and PVDF materials. These values are used in ANSYS modeling.

The final stage of the preprocessor, before starting the computational iteration and finding the solution, is the elements attributes and Meshing. In this stage, each part of the sensor is linked to their respective materials and elements type. After that, the whole modeled layers are glued to each other and finally the elements are meshed [80]. Meshing is refined many times until finally the number of the elements reaches the maximum number for this software edition (16000 elements). The sensor after modeling and meshing is shown in Figure 3.3.

The next two steps are the Solution and the General Post Processor. These are discussed in the last section with the sensor simulation results.

### 3.2 Parametrical Analysis

The fabricated sensor to be tested is 30 mm long and 15 mm wide. These dimensions are compatible with the experimental set-up and to the available commercial laparoscopic tool.

The thickness of the silicon layer of the sensor is designed to cover the loading range of the grasping forces, as well as to be sensitive to the small mechanical forces which are equivalent to the pulse of blood vessels. After etching teeth shapes on the silicon layer, the thickness of the plate at the base is chosen to be 100  $\mu\text{m}$ .

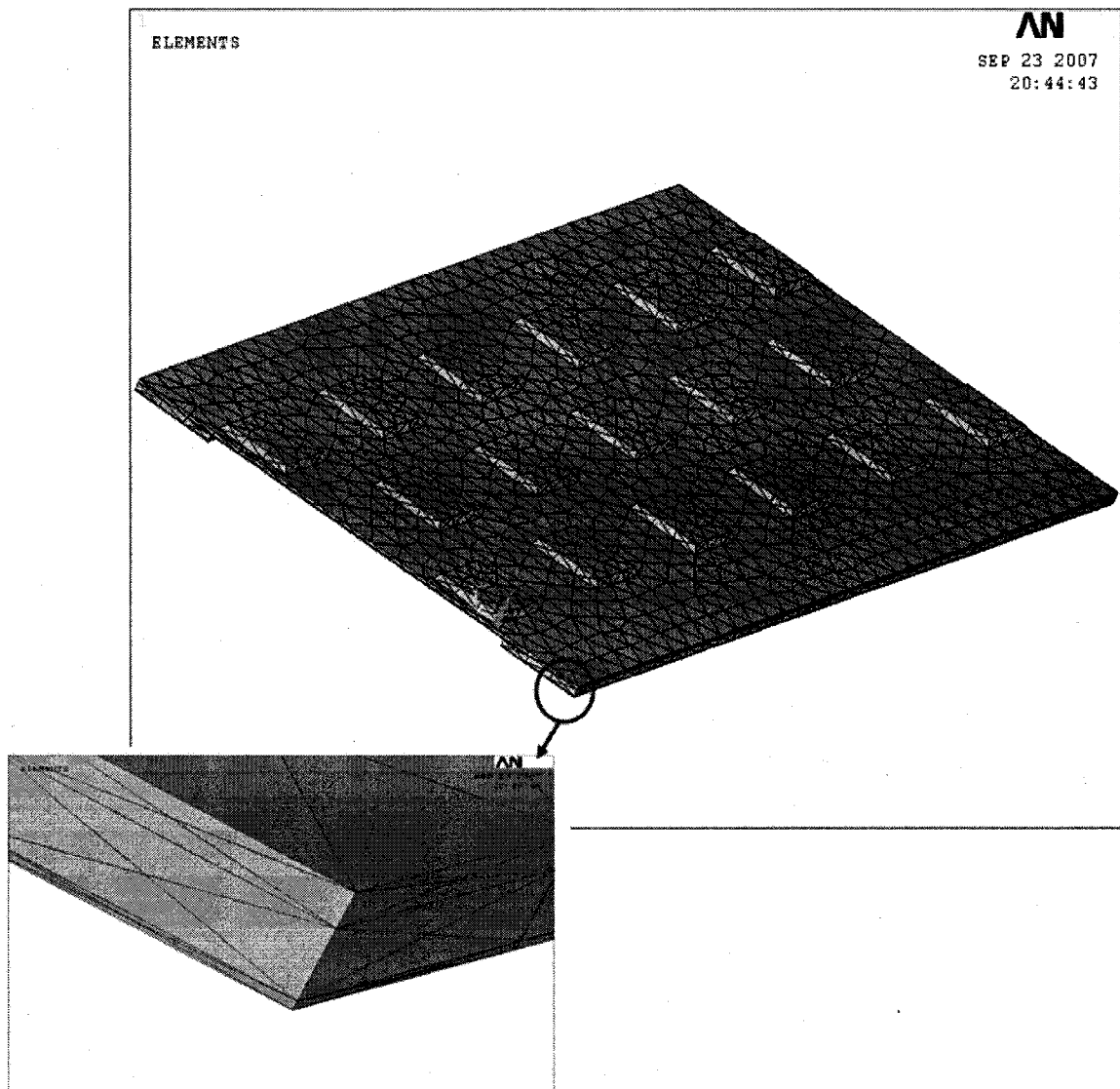


**Figure 3.3 - Finite element meshing of the sensor**

Each designed sensor could have a different length ( $l$ ), width ( $w$ ) and thickness ( $t$ ) and be compatible with different endoscope tools and sizes. For any combination of sensor

dimensions, and to cover the same loading and outputs ranges, a parametric study of the design is undertaken by running the model with ANSYS 10 software many times and finding the solution by following the solution steps, as detailed in Section 3.4.

The elongation of the silicon layer in the Y-direction as a simple plate is studied with different dimensions of the sensor. The simple plate is shown in Figure 3.4.

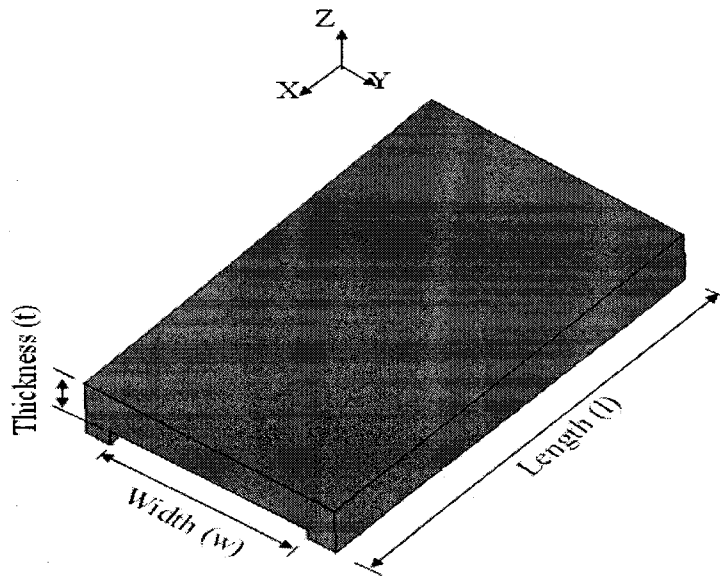


**Figure 3.4 – The simple plate which used in the parametrical study**

A point load of 4N magnitude is applied on the center of the plate, and the elongation in Y-direction with respect to different lengths, widths, and thicknesses of the sensor is calculated.

At first, the elongation versus the length is studied by keeping the width and the thickness at constant values all the time (15 mm for the width and 100  $\mu\text{m}$  for the thickness) and varying the length and recording the elongation each time. The relationship between each elongation and length is shown in Figure 3.5.

The same is done for the width, where the length and the thickness of the plate are kept constants (30 mm for the length and 100  $\mu\text{m}$  for the thickness), while changing the width

of the plate and recording the elongation for each width. The relation between each elongation and width of the plate is shown in Figure 3.6.

Finally the length and the width are kept constant (30 mm for the length and 15 mm for the width) while the thickness of the plate is changed for different values. The relation of elongations and thicknesses is shown in Figure 3.7.

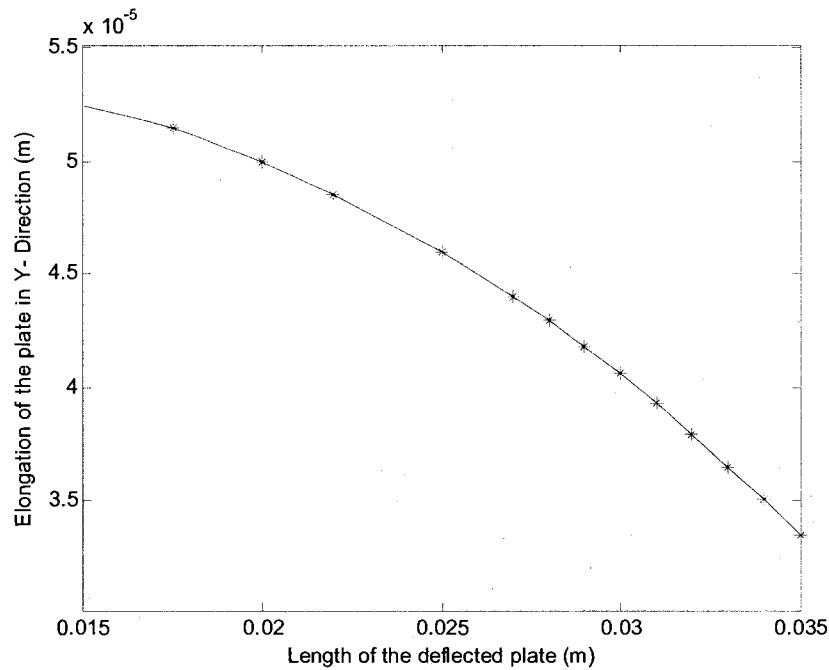


**Figure 3.5 - Deflections of the silicon plate in Y-direction versus plate length**

Taking into consideration the fracture strength of silicon (approximately 4 GPa) and a reasonable factor of safety (F.S = 3) for the design; the maximum point load applied on the simple plate having the same dimensions as the designed prototype sensor ( $l = 30$  mm,  $w = 15$  mm, and  $t = 100$   $\mu$ m) is 4 N. In that case, elongation of the plate in the Y-direction was approximately 40  $\mu$ m. In addition, for the same dimensions and a small point load which could be comparable to the blood vessels pulse ( $\sim 1$  mN); the elongation was about 9 nm.

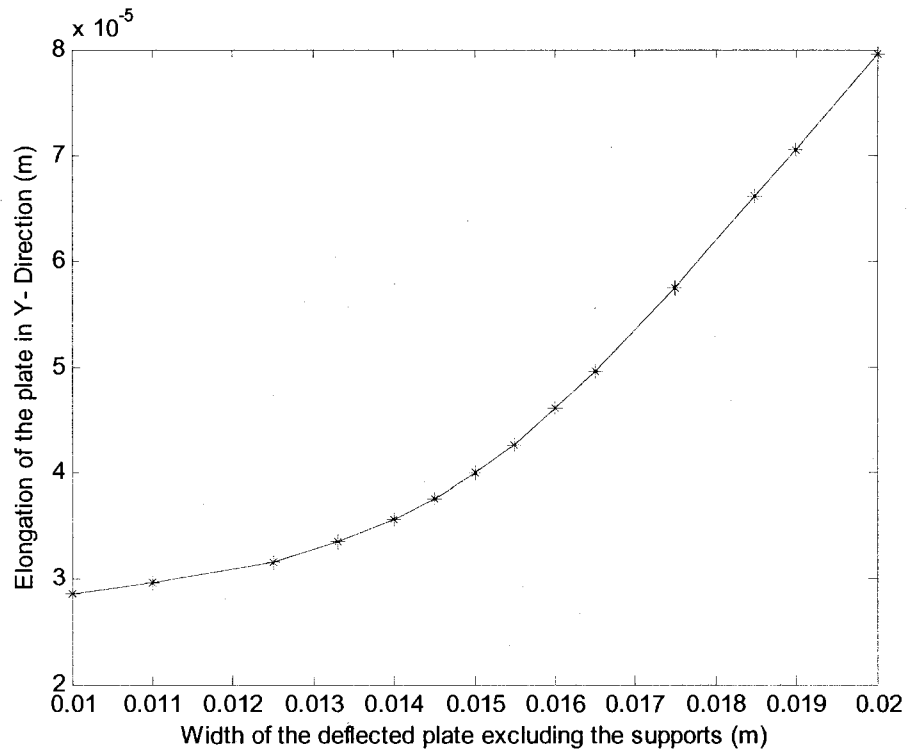


**Figure 3.6 - Deflections of the silicon plate in Y-direction versus plate width**

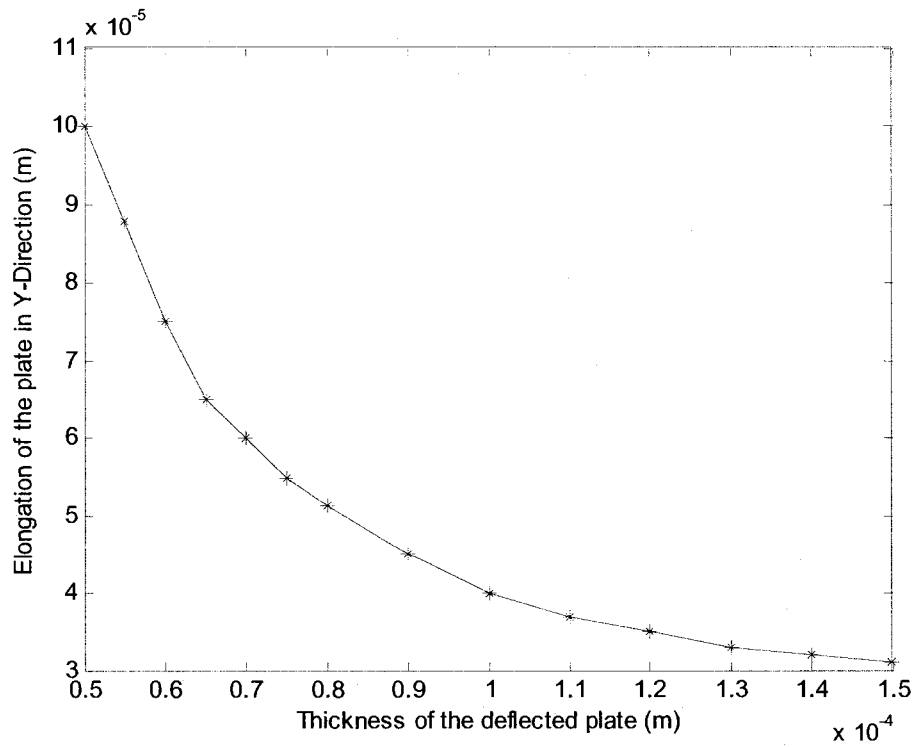


**Figure 3.7 - Deflections of the silicon plate in Y-direction versus plate thickness**

For each dimension of the plate, a range of that dimension is given to the ANSYS software; ANSYS solution loop is keep changing the dimensions within the given ranges and finding the elongations at each dimension combinations under both 4N and 1mN point load applications. The ranges used with this analysis were: 1 - 4 cm, 0.75 - 2 cm, and 50 - 150  $\mu\text{m}$  for the length, width, and thickness respectively.

Each dimensions combinations with elongations equal to the prototype elongations, under the 4N and the 1mN point load application, is picked and plotted to represent a point on the 3D-surface shown in Figure 3.8. Any point of the surface is representing a different dimensions of the silicon plate which having the same elongations as the prototype elongations.

By choosing one dimension of the sensor, which could be restricted to a specific value to fit the medical tool itself, the other two dimensions can be found from Figure 3.8 to have the same loading and elongations of the designed prototype sensor. In conclusion, the designed sensor can be with different dimension but working with the same loading range. That gives the design a flexibility to be microfabricated with different dimensions which could fit with different surgical tools.

### **3.3 Geometrical Analysis of the Sensor**

Geometry of the corrugated shapes of silicon layer was discussed in the first section. The second section is discussing orientations, locations and distributions of the sensing elements. These studies are carried out by running the models using ANSYS 10 software repeatedly and finding the solution by following the solution steps explained in Section 3.4.

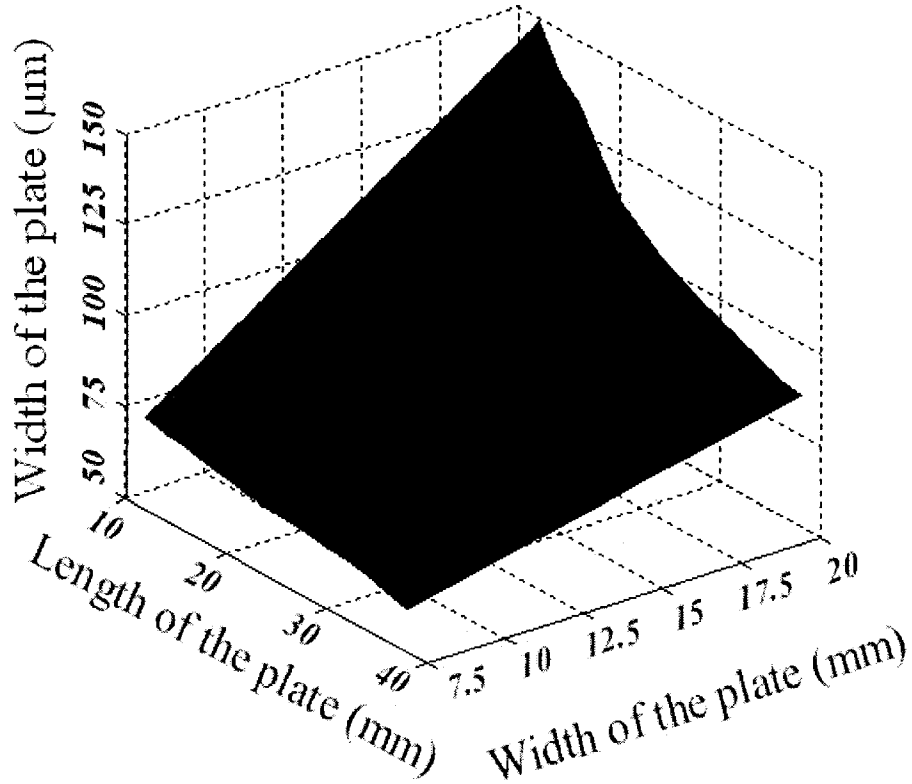


**Figure 3.8 - Different dimensions of the sensor for the same loading range**

### 3.3.1 Teeth Arrangements

For the designed prototype sensor, the tooth-like shape of the etched silicon layer is studied. Three cases were simulated and examined in order to determine which gave the largest deflection. These included a simple plate of 100  $\mu\text{m}$  thickness, a regular arrangement of the teeth with base plate thickness equal 100  $\mu\text{m}$ , and an irregular arrangement of the teeth with 100  $\mu\text{m}$  of base plate thickness. Figure 3.9 shows the three shapes. The deformations, under the same point load at the center in each case on one hand, and under the same uniform distributed load on the other hand, were recorded as shown in Figure 3.10. The comparison curves of deformation in the Z-direction between

the three cases for the point load case are shown in Figure 3.11, and the comparison curves of the Z-direction deformation between the three cases for the distributed load case are shown in Figure 3.12.

As can be seen in the curves which shown in Figure 3.11 and Figure 3.12; the greatest deformation occurred using the simple plate. But since the designed sensor has to be integrated with a grasper, and the teeth-shape is required for better grasping ability, the simple plate is a bad choice. Moreover, the figures showing that the case with irregular arrangements of the teeth is deformed larger than the case with regular arrangements of the teeth. In conclusion, the irregular teeth arrangement was chosen because of its teeth property and because it is more deformable than the regular teeth arrangement.

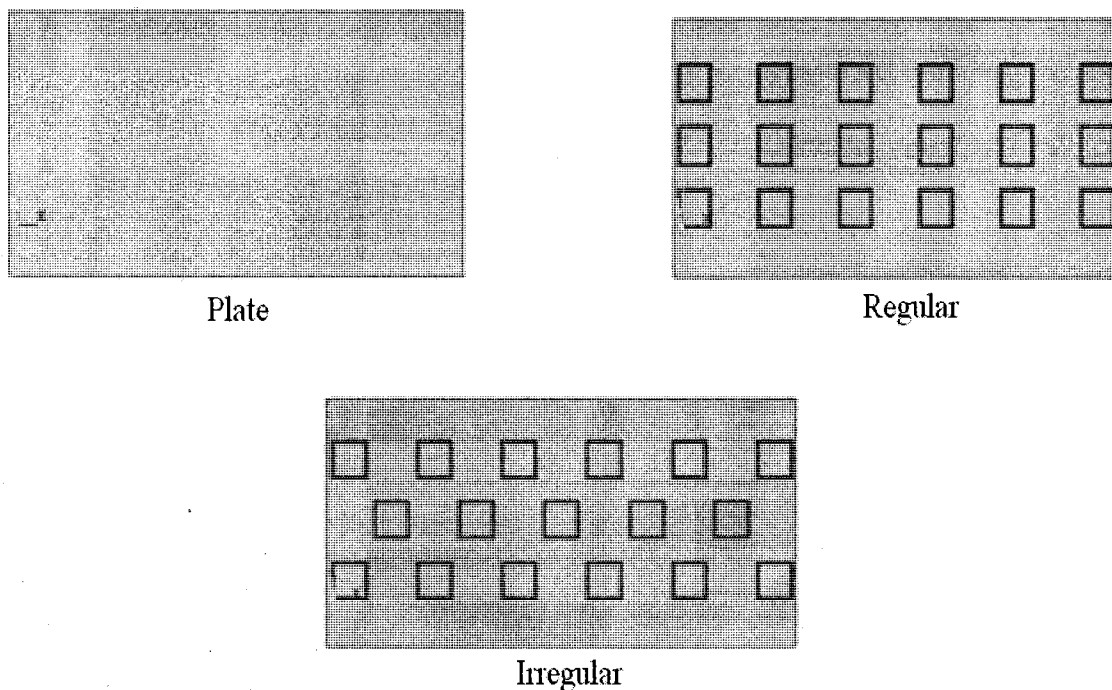
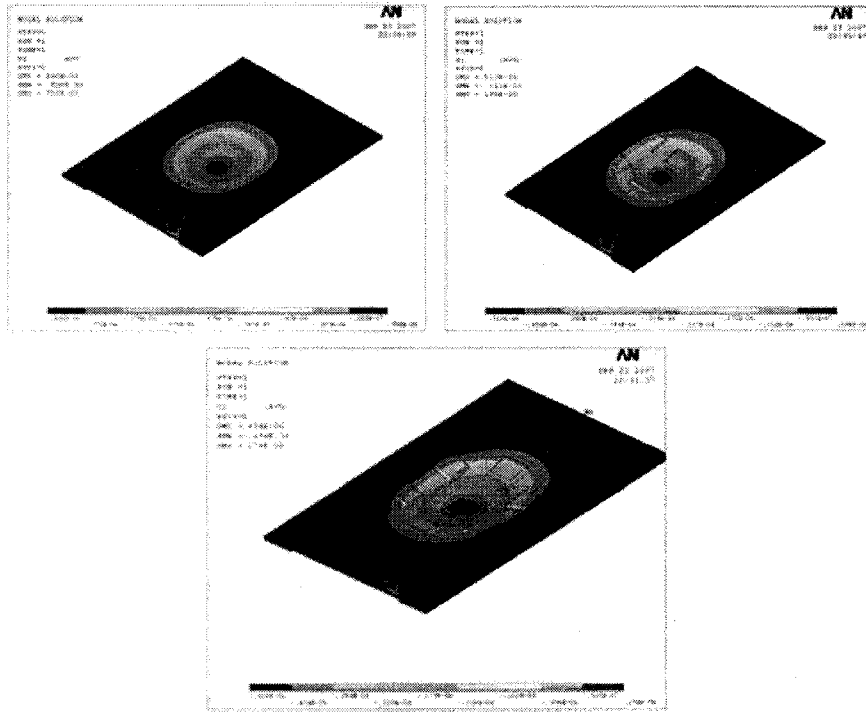
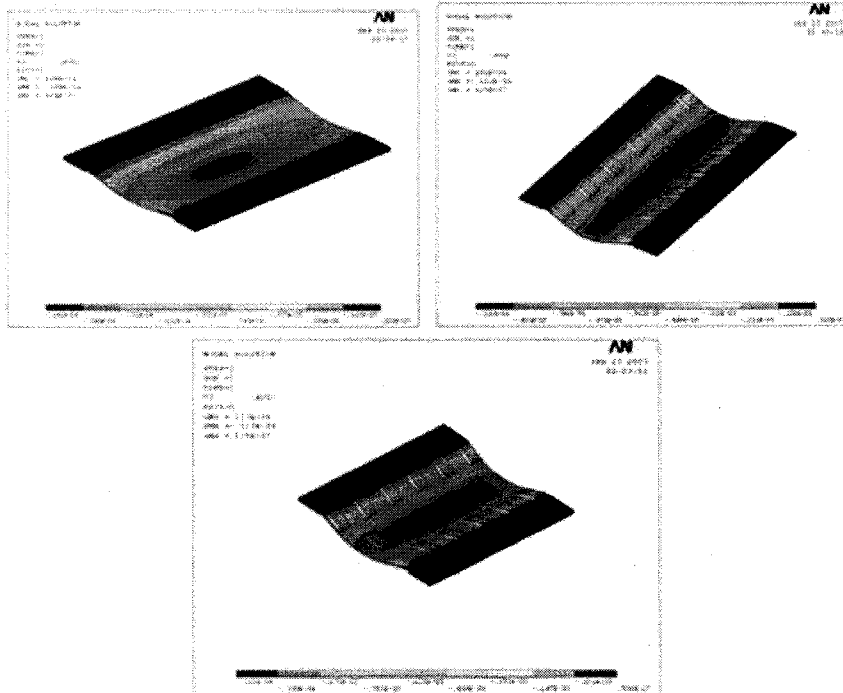


**Figure 3.9 - The proposed shapes of the microfabricated silicon layer**



Point load at the center



Uniform distributed load

Figure 3.10 - Deformations of the proposed shapes

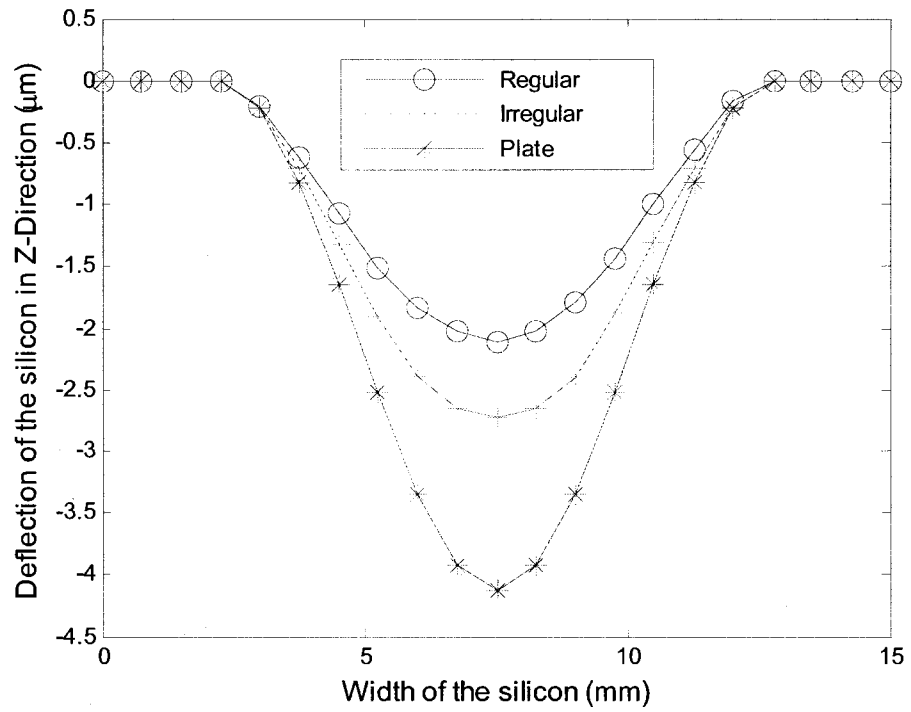


**Figure 3.11 - Deformation curves in the Z-direction while a case of point load at the center**

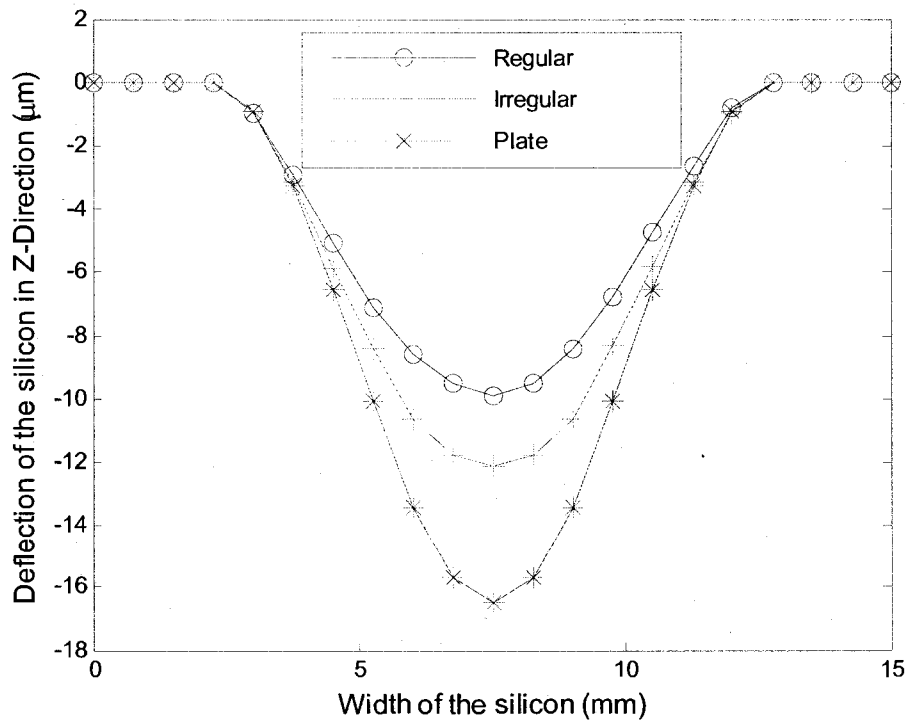


**Figure 3.12 - Deformation curves in Z-direction while a case of distributed pressure load**

### 3.3.2 Sensing Elements Arrangements

The location and distribution of the sensing elements on the PVDF layers are studied. PVDF strips were glued at the middle and each support then a point load (1N) was applied on the center of sensor and the output voltage distribution on each PVDF layer is noted. Figure 3.13 and Figure 3.14 shows the voltage distribution on PVDF layers at the supports and the middle, respectively. As shown in these two figures, the induced voltage profiles at each layer were distributed on the middle region taking around one third of each PVDF layer area. These regions are the useful regions of PVDF layers and they are of our main interest to collect the output charges. For that reason, these useful regions will be located at the middle and considered as one combination of the sensing elements. Because that combination covered almost one third of the overall area, so two other combinations of sensing elements can be added and distributed on the PVDF layers and finally cover the whole area of PVDF layers. The active sensing element locations and distributions are shown in Figure 3.15.

Finally, the orientation of the PVDF layers is studied. Two possible cases are considered. In the first case, the drawn direction ( $d_{31}$ ) of PVDF films is oriented parallel to the sensor width (Y-direction). In the second case, the drawn direction of the PVDF layers is oriented parallel with the length of the sensor (X-direction).

The output voltage distribution on the supports and middle PVDF layers for the first orientation case ( $d_{31}$  in Y-Direction) while the point load is applied on the center of sensor are shown in Figure 3.13 and Figure 3.14, respectively. When the second case of orientation is considered ( $d_{31}$  in the X-Direction) and for the same loading conditions, the

output voltage distribution on the supports and middle PVDF layers are shown in Figure 3.16 and Figure 3.17 respectively.

It is clear that at a higher voltage,  $d_{31}$  direction of PVDF must be oriented parallel to the sensor width (Y-direction), and the cross-talk between the neighbored sensing elements on same PVDF layer is less. That is because the voltage distribution in this case is more uniform and bounded on the force action region. For that reason, the case of drawn direction and width of the sensor are parallel is chosen.

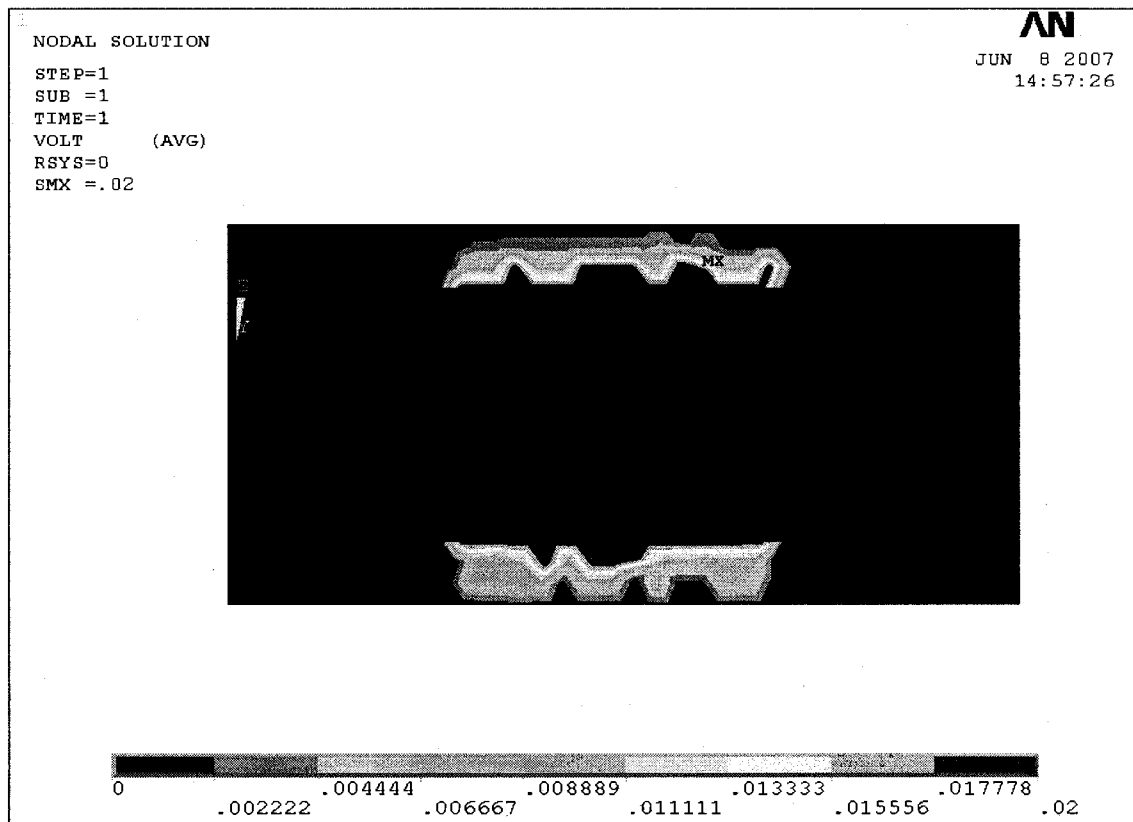


**Figure 3.13 - The output voltages on supports PVDF layers under point load at the center of the sensor ( $d_{31}$  oriented with Y-direction)**

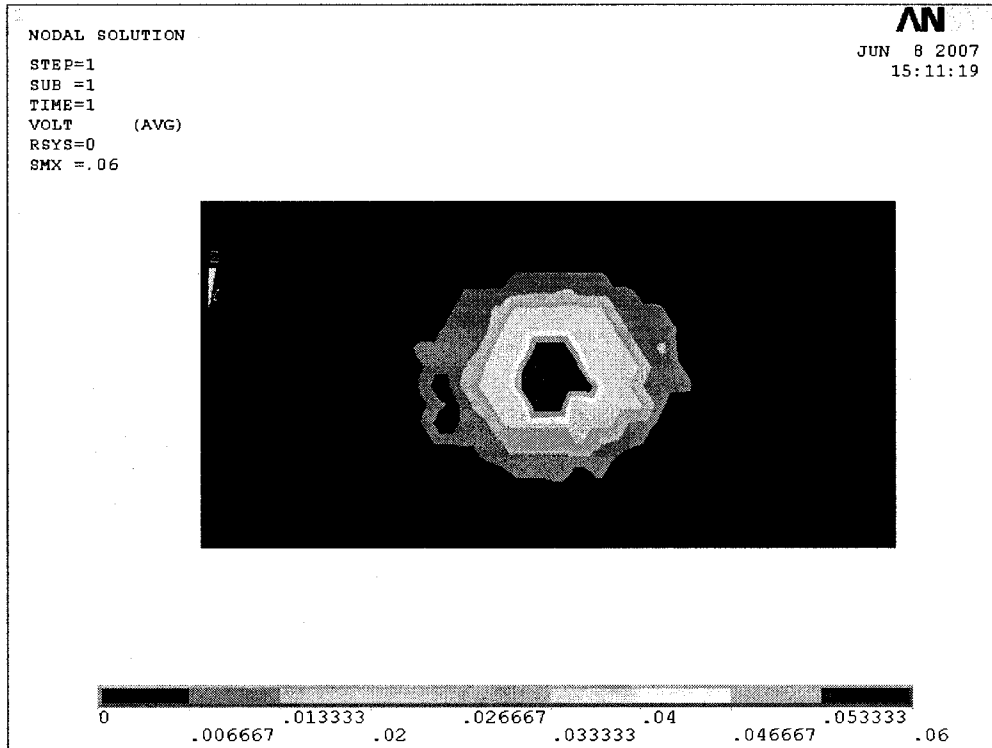


Figure 3.14 - The output voltage on middle PVDF layer under point load at the center of the sensor ( $d_{31}$  oriented with Y-direction)

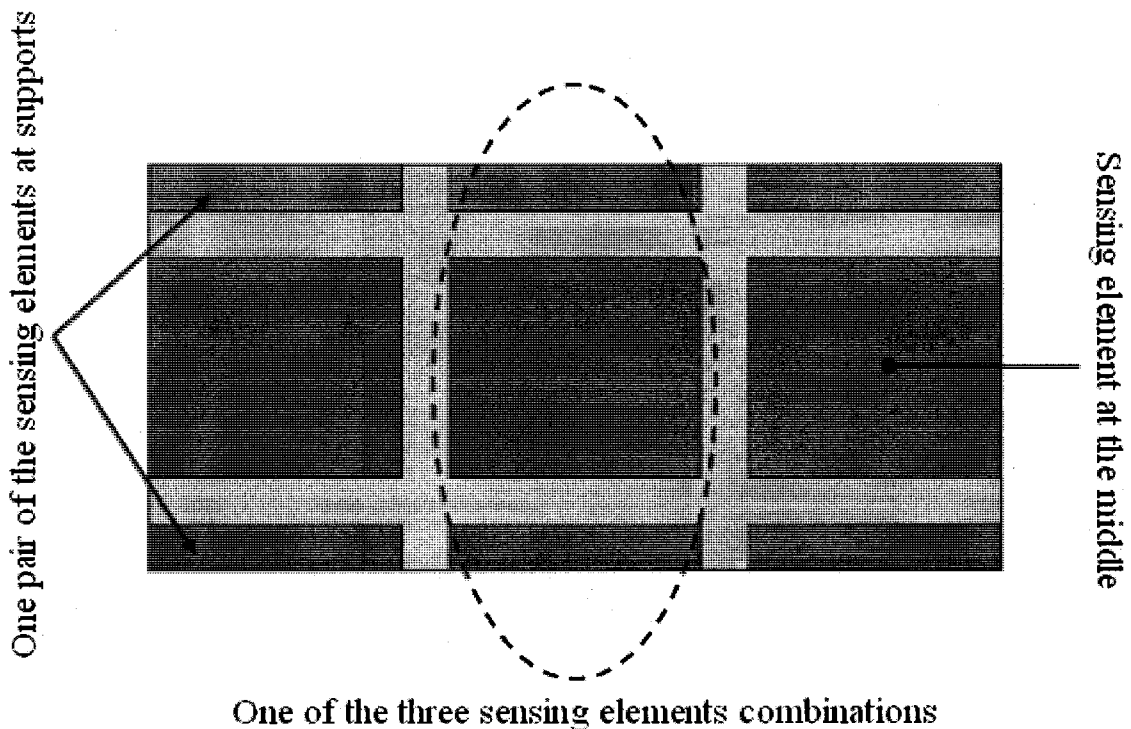


Figure 3.15 - Distribution's of the active sensing elements at each PVDF layer

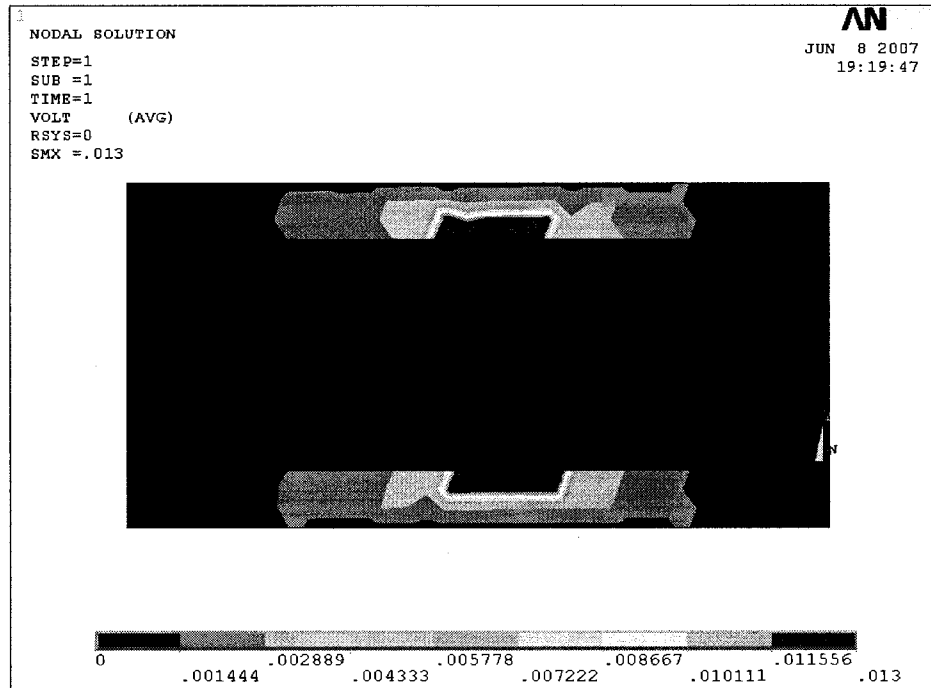


Figure 3.16 - The output voltage on supports PVDF layers under point load at the center of the sensor ( $d_{31}$  oriented with X-direction)

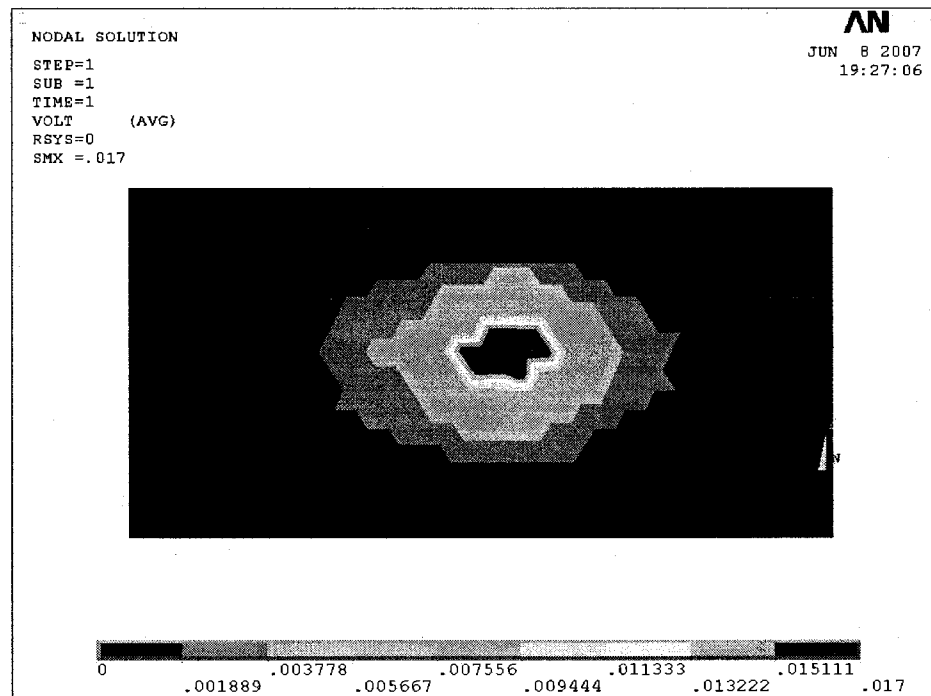
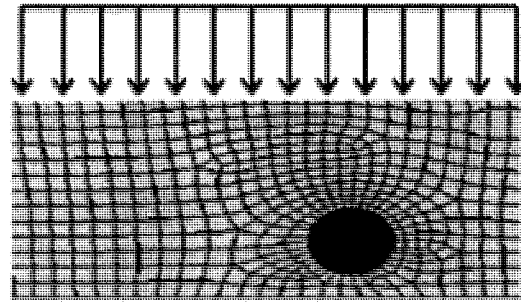


Figure 3.17 - The output voltage on middle PVDF layer under point load at the center of the sensor ( $d_{31}$  oriented with X-direction)

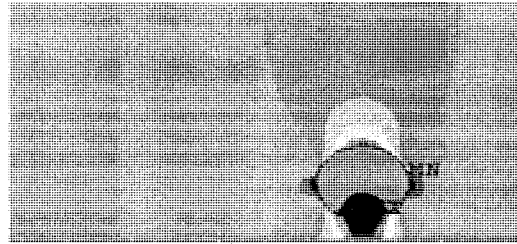
### 3.4 Hidden Features inside Grasped Objects

In minimally invasive surgery, finding the position of a concentrated load is very important, as it could be used in determining the positions of variety of hidden anatomical features. When a soft tissue without any embedded feature is grasped, the stress profile recorded at the surface is kind of a uniform (or at least smooth) distributed load. However, in general, the existence of any hidden anatomical feature such as lump, or hollow tubular feature whether with pulsation (e.g., arteries or veins) or without pulsation (e.g., ureters) appears as a disruption in this uniform pressure distribution.

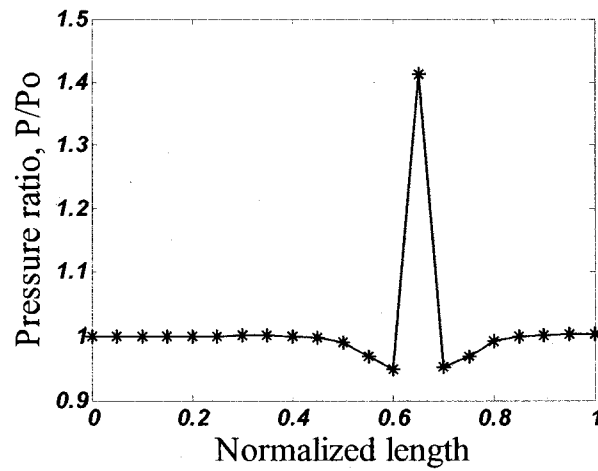
For instance, when there is no lump within the grasped tissue, a uniform background pressure distribution ( $P_0$ ) would be registered at the contact surface of grasped object and sensor surface. However, when there is an embedded lump in a bulk soft tissue, a sudden jump in the normal stress would be observed. The peak stress value occurs exactly at the position of the lump. Figure 3.18-a shows a finite element model of a lump embedded in a slab of soft material and a compressive load, simulating the grasped boundary conditions, is applied from the top and bottom. In the following simulations, the materials were assumed to be isotropic. The properties of soft material were considered as  $E_t=20$  kPa and  $\nu=0.49$  whereas Young's modulus of 200 kPa and  $\nu=0.4$  for the lump. The normal stress profile at the sensor surface (i.e., here the bottom surface) is shown in Figures 3.18-b and c. In Figure 3.18-c, the stress values read at the contact surface ( $P$ ) was normalized by dividing to the background pressure  $P_0$  (i.e., pressure values when there is no lump). It is shown that more than 40% force increase at the location of lump is recorded. A simple model of this behavior can be thought as a point load that is superimposed on a uniform distributed load, as shown in Figure 3.18-d.



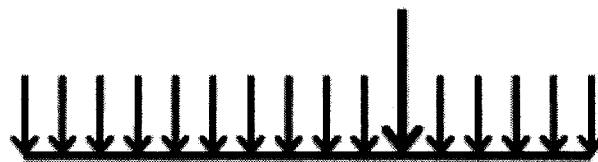
(a)



(b)



(c)

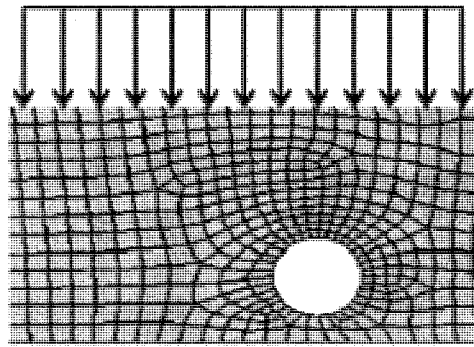


(d)

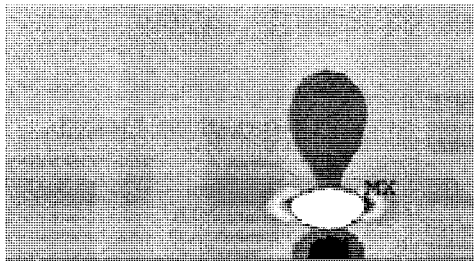
**Figure 3.18 - The finite element model of the soft object with an embedded lump**

The 2-D finite element model of a non-pulsating tubular feature embedded in a bulk soft tissue is shown in Figure 3.19. This model can be seen as a void inside the tissue. To avoid unnecessary complexity, the material property of the feature wall was considered

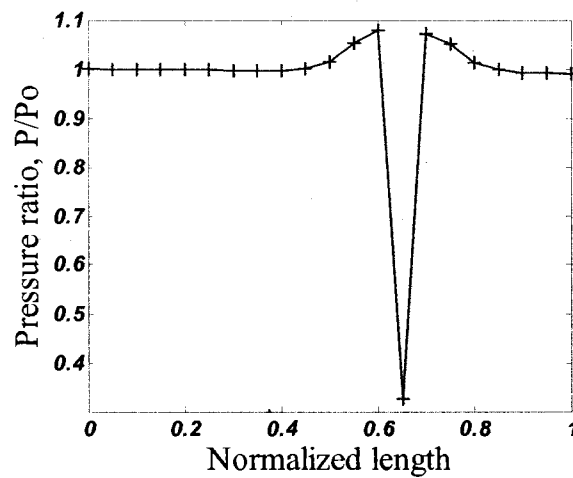
similar to the surrounding tissue. As shown in Figures 3.19-a, b and c, when there was a void inside the grasped object, a sudden decrease at the position of the void was observed.



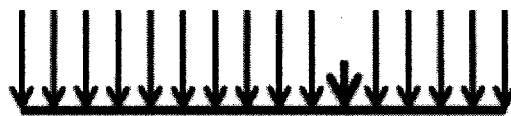
(a)



(b)



(c)



(d)

**Figure 3.19 - The finite element model of the soft object with an embedded void**

In Figure 3.19-c, the calculated pressure values ( $P$ ) are divided by the background pressure ( $P_0$ ). A sudden decrease of about 65% is predicted for this scenario. Again in this case, as shown in Figure 3.19-d, the problem of finding a hidden anatomical feature is turned into finding the location of a point load. This is also valid for a pulsating artery or vein. These pulsating features are dynamic, though can be considered as a void between two consecutive beats and seen as a lump during pulsation. Figure 20 shows the transient stress profile at the contact surface. As the simulations show when there is no pulsation (i.e., at  $t=0$  sec), there is a reduction in the normal stress. However, during the pulsation the amplitude of the load start increasing and reaches to its maximum when the pulse is in its peak value (here,  $t=0.3$  sec).

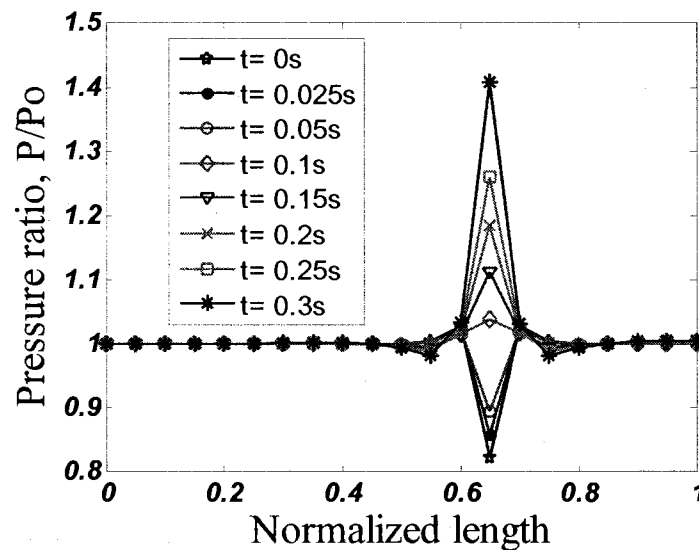


**Figure 3.20 - The normal stress distribution at the contact surface, when a pulsating feature is embedded in the tissue is calculated.**

From the above simulations it was concluded that if a sensor system is capable of detecting and locating concentrated loads, it would be able to detect and locate a variety of hidden anatomical features.

### 3.5 Sensor Simulations

In this section, the ANSYS solution of the modeled problem is carried out and the solution sequence is shown in Figure 3.21. The first required entry is to define the analysis types such as static, harmonic, dynamic. Applied loads require entry of boundary conditions that apply to our model. The last step is to solve the meshed model [80].

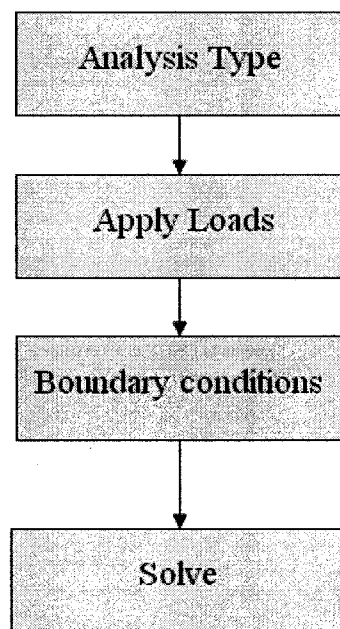


**Figure 3.21 - ANSYS model solution steps**

As shown on the solution sequence; the type of solution, such as static or dynamic have first to be defined. The type chosen with this analysis is the static analysis type because the applied force is either a static point load or a uniform static pressure.

The next step is to define the boundary conditions of the model [80]. The first boundary condition is defined as being the bottom side of the lower PVDF layers at supports is fixed to a zero displacement in the X, Y and Z directions because the bottom side of the

PVDF is glued to the rigid Plexiglas layer. The second boundary condition is zero voltage on the top side of the PVDF layers to represent the common electrode of PVDF layers at middle and supports. The last boundary condition which must be considered is the voltage coupling of nodes on each active sensing element to have the same voltage value in order to simulate each electrode at the bottom side of the PVDF layers. These coupling boundary conditions are shown in Figure 3.22.

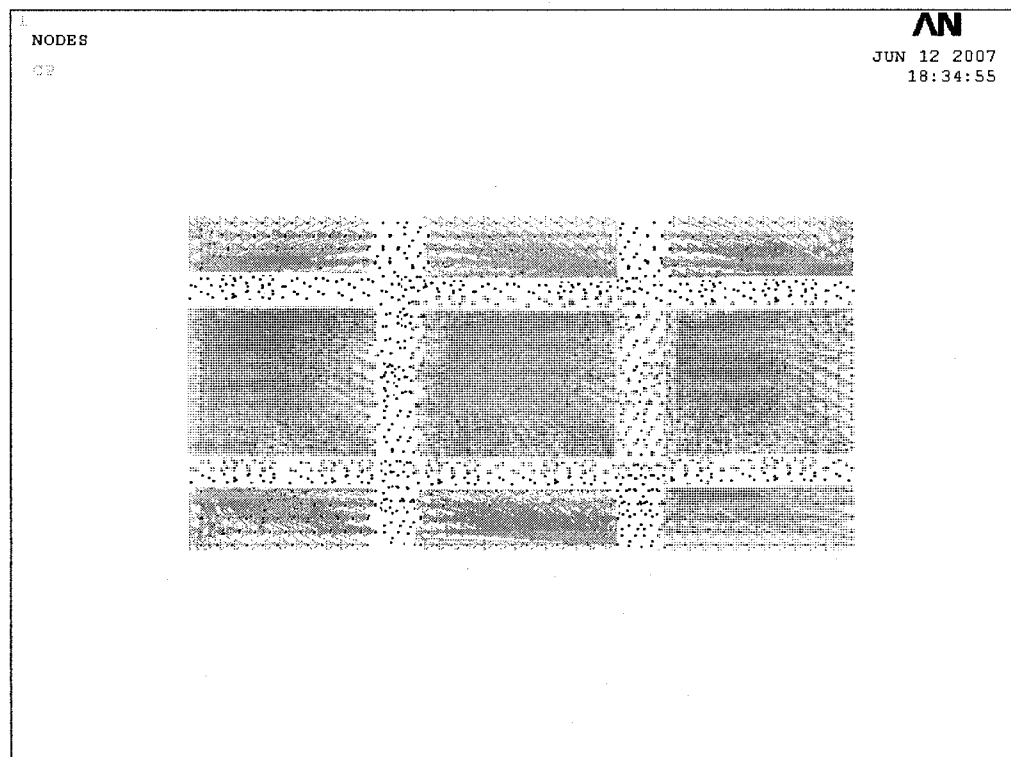


**Figure 3.22 - The voltage coupling boundary condition which applied on the bottom of PVDF layers**

The last step is running the program and getting results from the General Post Processor menu. Results are reviewed using the many options available on the General Post Processor, plot section and list section which provides the results in graphical

presentation and numerical values respectively. Results such as output voltage at each PVDF layer, stresses, strains and reactions at any point can be visualized using graphs.

Different kinds of loading are applied in order to find the performance of the designed sensor functionality. Simulation is carried out many times and the results are recorded and compared. The following sections illustrate each kind of loading and its simulation results.

The first section dealt with a point load with different magnitudes and located at the center of the silicon plate, while the second section discussed a case of point load of 1N magnitude and located at different locations on the silicon plate. In the last section, a uniform distributed pressure on the tissue being contacted was considered and the simulation was carried out for different contacting tissues softness.

For the results comparison, each sensing element of the sensor is denoted by a unique notation as shown in Figure 3.23.

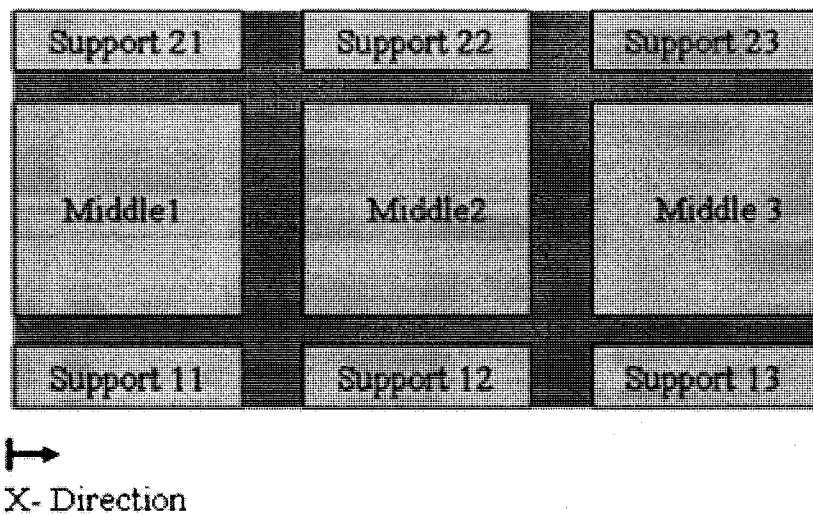


**Figure 3.23 - Notations of the PVDF sensing elements**

### 3.4.1 Point Load at the Center

The kind of loading used in this section is a point load applied at the center of the silicon plate. This kind of loading and simulation is carried out in order to find a relation between the output voltages on PVDF layers with respect to the applied load magnitudes. From this, we obtain calibration curves for the designed model from which we can determine what grasping forces are actually applied during surgery.

As mentioned previously, the load is applied on the center point of the sensor at the top surface of the silicon layer at the point is shown in Figure 3.24.

The magnitudes of forces vary between the two designed range limits. At each load magnitude, output voltages at PVDF layers are recorded. The output voltage on PVDF layers when 1N is applied is shown in Figure 3.25.

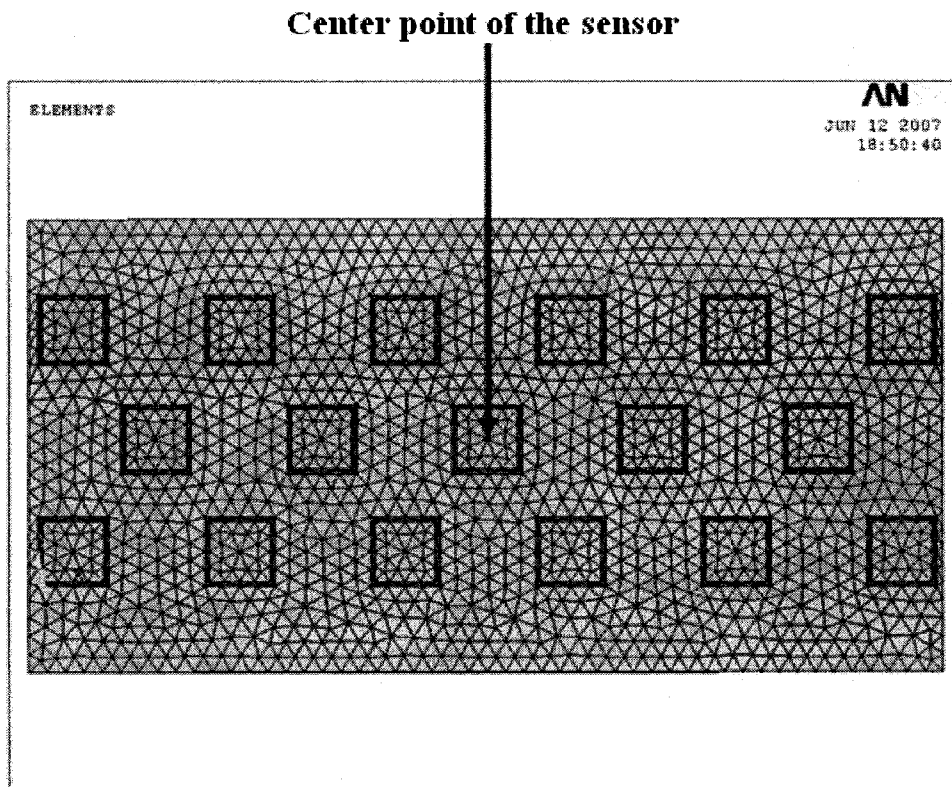


**Figure 3.24 – Top view of the meshed sensor showing a point load application at the center**

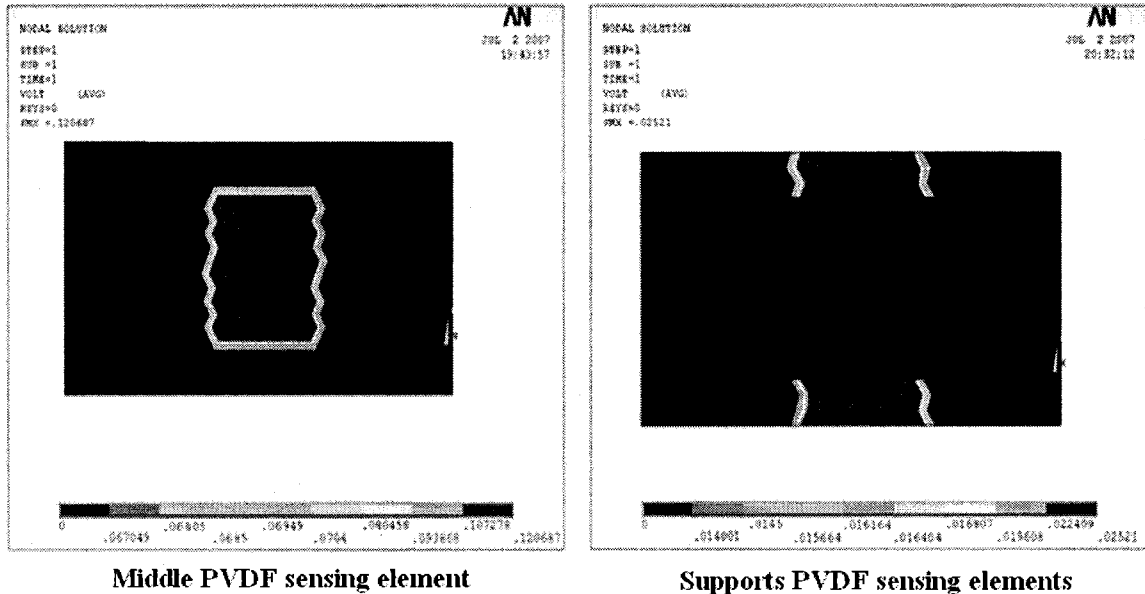


**Figure 3.25 - Output voltages at the PVDF sensing elements when a point load is applied at the center of the sensor**

The applied load is 5 N which is the maximum allowable grasping force for this modeled design, and the minimum is 1 mN which it is comparable to the blood vessels pulse. The calibration curves are shown in Figure 3.26.

As shown in the calibration curves, the linear relation between output voltage at each PVDF layer and the magnitude of applied load is verified. As shown, the output voltage at each support is equal to each other because the application point of the loading is located at the center and the load is carried by the two supports equally. Also it is clear that the maximum output voltage is at the middle PVDF layer where it is working on the extensional mode while the other two layers at supports are working on the thickness mode. The PVDF layer at the middle is the more sensitive, and it is expected to detect the low magnitude forces such as the pulse in blood vessels. In this case, the magnitude of the applied force can be detected based on output voltages and the calibration curves.

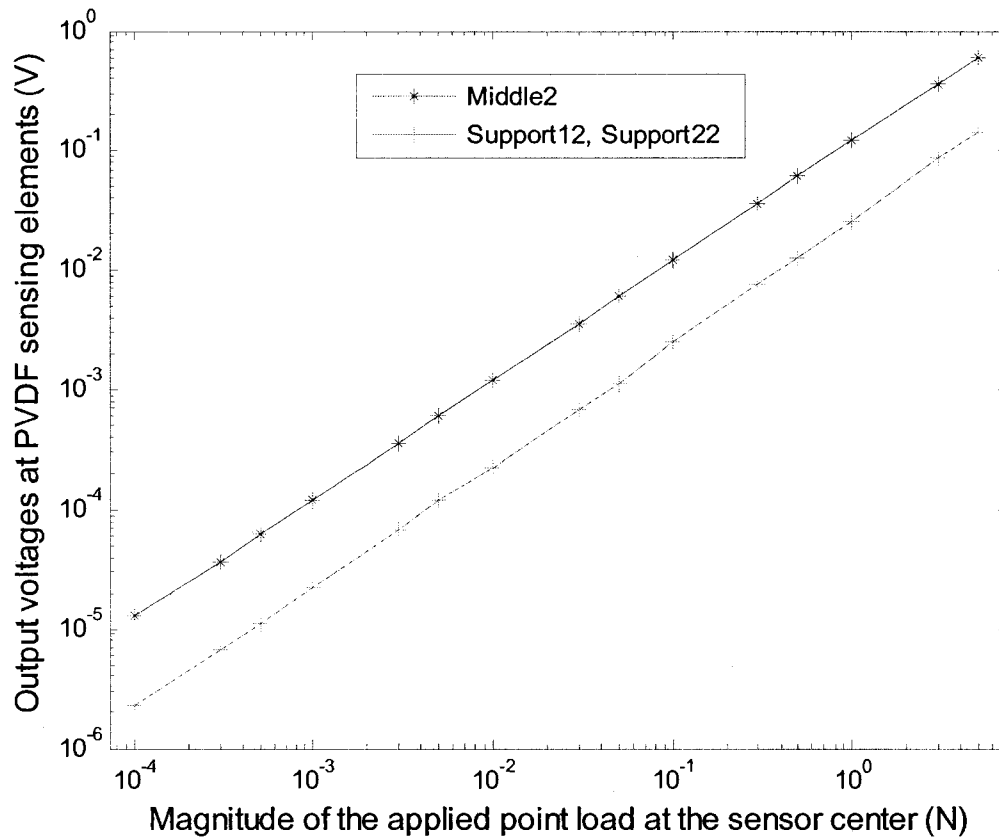


**Figure 3.26 - Output voltages on PVDF layers versus the different load magnitudes**

### 3.4.2 Point Load in XY Plan

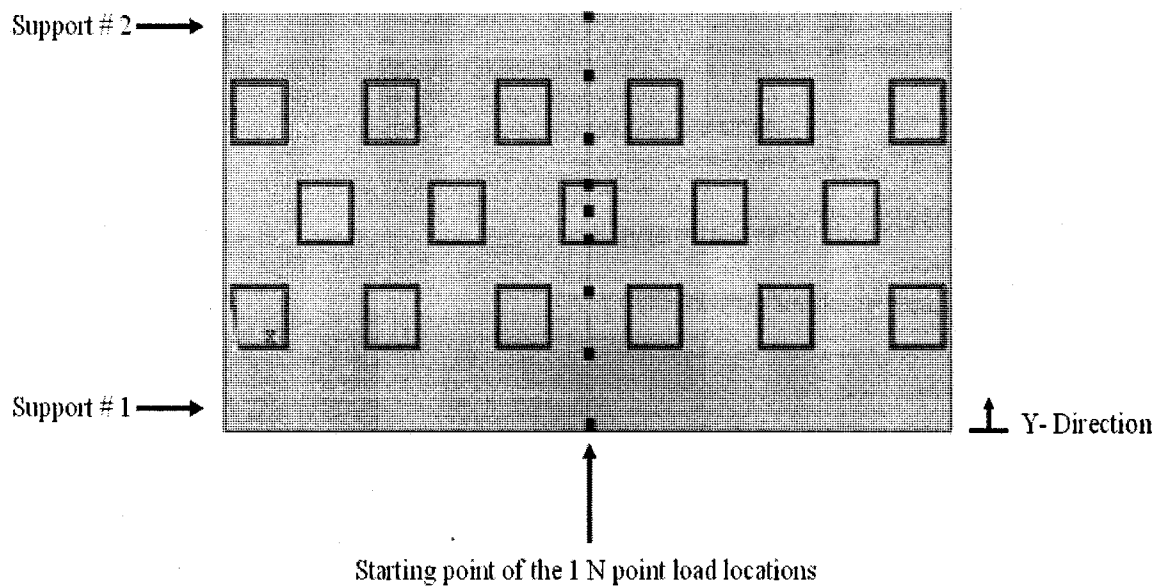
In order to detect the precise location of the point applied load, as when locating embedded lumps during surgery, a constant point load of 1N magnitude is applied on the silicon layer at different points each time.

Points of examination are chosen to move in the Y-direction at middle of the length at first, and then to move in the X-direction at the middle of the width. The following two sections discuss both cases.

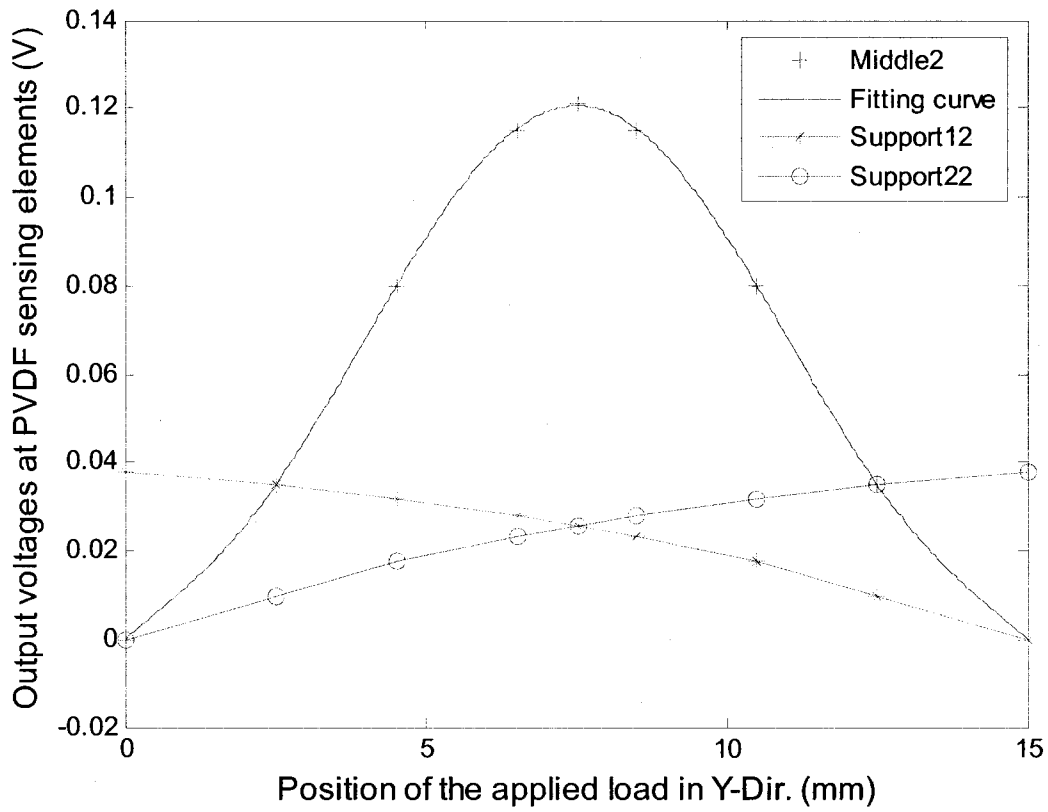
### 3.4.2.1 Point Load Moves Along Y-Direction

Figure 3.27 shows the points we were examining (the black squared points). Output voltages on the PVDF films at supports and middle are recorded and compared. Voltage curves versus location of the 1N point load are shown in Figure 3.28.

As shown in Figure 3.28, a higher voltage is induced on the middle PVDF layer when the point load is applied on a point (at  $y = 7.5$  mm). This is the center point on the tooth-shape plate and the base plate deflection is at its maximum when the load location lies at the center. Once the load is moves forwards or backwards from that point; output voltage on this PVDF layer will become lower, and a symmetrical curve on the left and the right sides of the center point is displayed.



**Figure 3.27 – Position of the point load application along Y- Direction**



**Figure 3.28 - Output voltages at the sensing elements when a point load is applied along Y-Direction**

The output voltages on PVDF layers at supports are also shown from which it is clear that that maximum voltage on the PVDF layer at support #1 occurs when the point load is applied on the top of support #1 ( $y = 0$ ). It then goes down when the load location moves further away until reaching zero voltage when the load is applied at the top of support #2 ( $y = 15\text{mm}$ ). On the other side, the output voltage on PVDF layer at support #2 starts from zero value when the load is applied on top of support #1, and then becomes correspondingly higher when the load location moves further away until finally reaching the maximum output voltage when the load is applied on top of support #2. The output voltages on both PVDF layers at support #1 and support #2 equal each other when the

load acts at the center point ( $y = 7.5 \text{ mm}$ ) which is the same when the output voltage at middle PVDF is maximum.

In conclusion, the difference between output voltages on the PVDF layers at supports indicates the location of the applied load as illustrated by the curve shown in Figure 3.29. The summation of these two voltages indicates the total force magnitude and is shown in Figure 3.30.

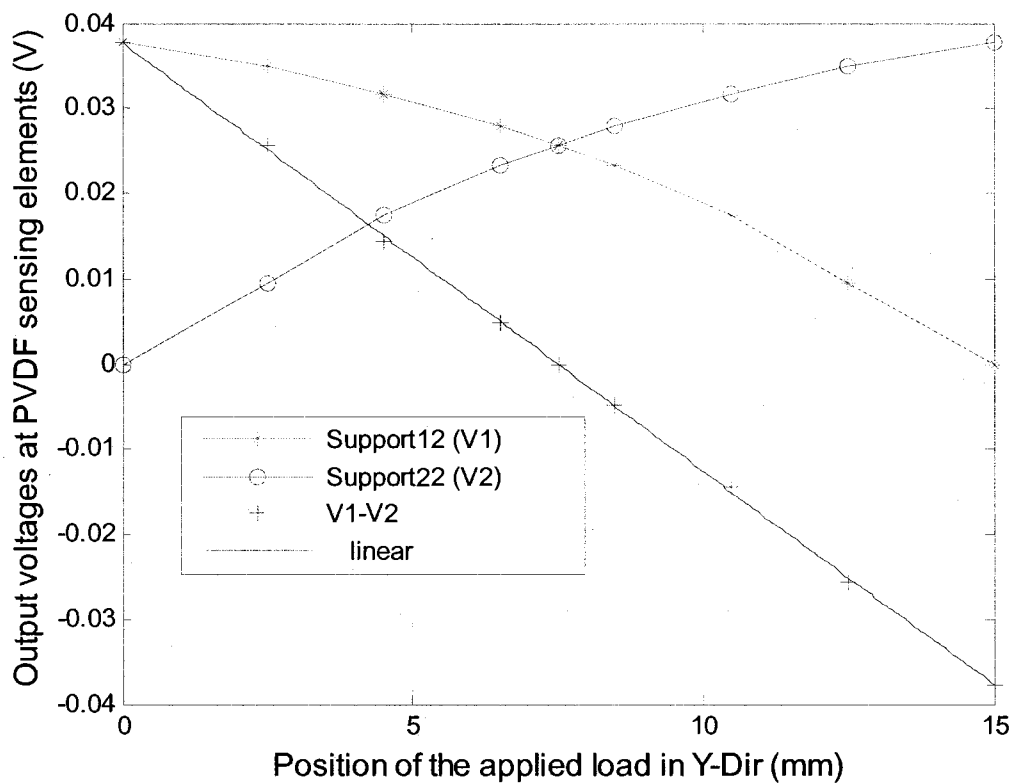


**Figure 3.29 - The difference between output voltages at the sensing element Support12 (V1) and the sensing element Support22 (V2)**

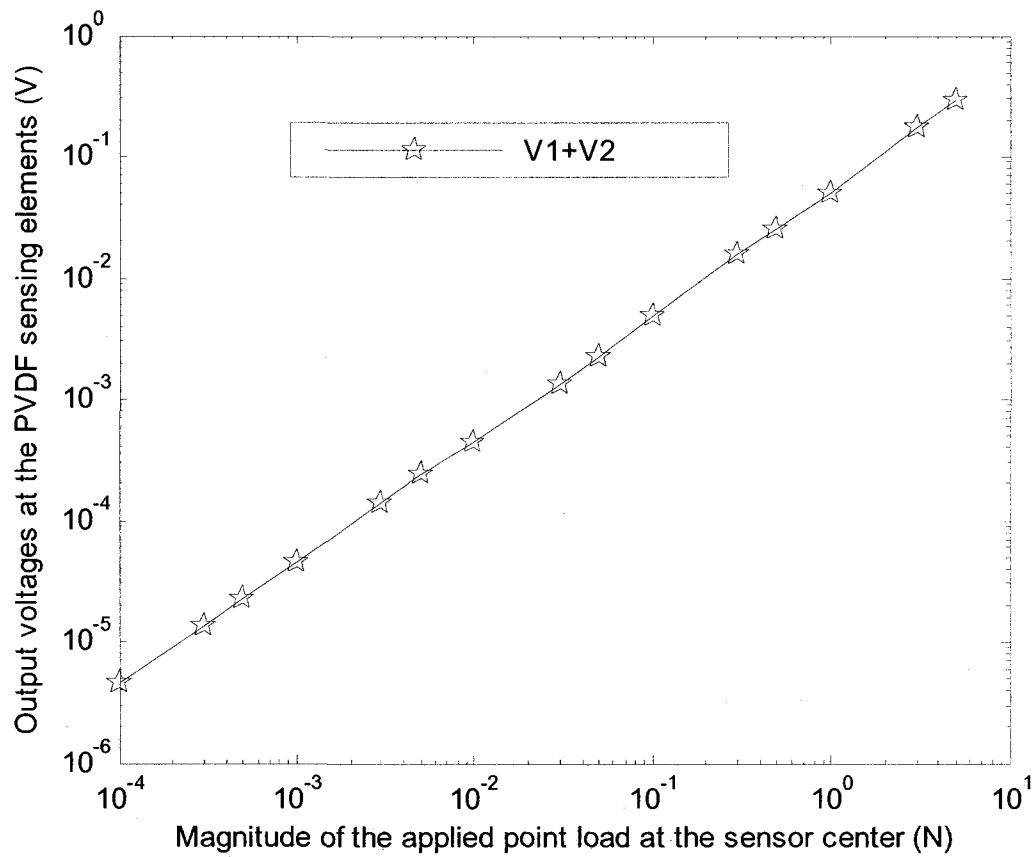


**Figure 3.30 - Summation of output voltages at the sensing elements Support12 (V1) and the sensing element Support22 (V2)**

### 3.4.2.2 Point Load Moves Along the X-Direction

Figure 3.31 shows the points we were examining (the black squared points). Output voltages on the active sensing elements of the PVDF films at supports and middle are recorded and compared. Output voltages of the sensing elements at supports and middle versus location of the 1N point load are shown in Figure 3.32 and Figure 3.33, respectively.

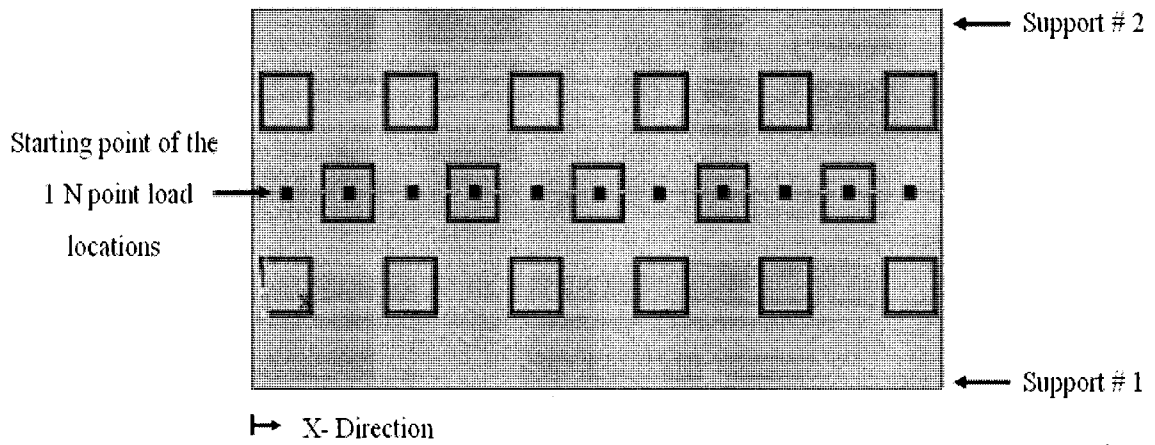


**Figure 3.31 - Position of the point load application along X- Direction**

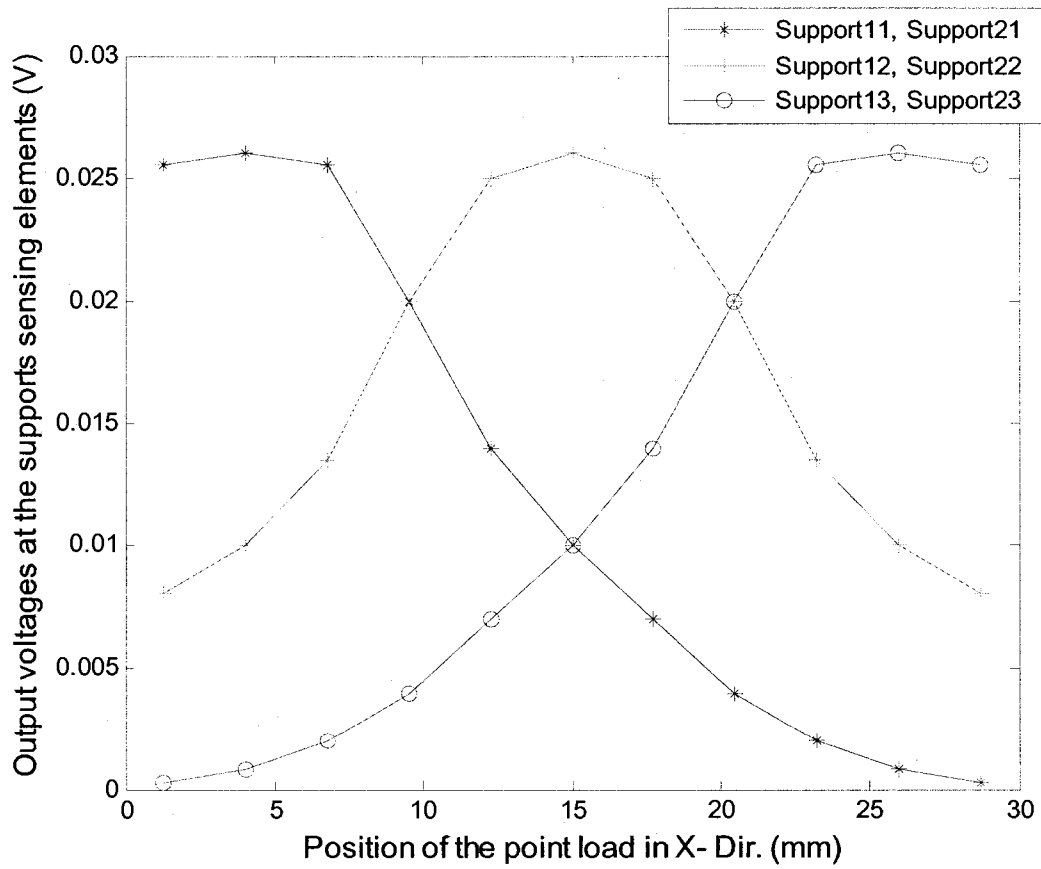


**Figure 3.32 - Output voltages at the supports PVDF sensing elements when a point load is applied along X- Direction**

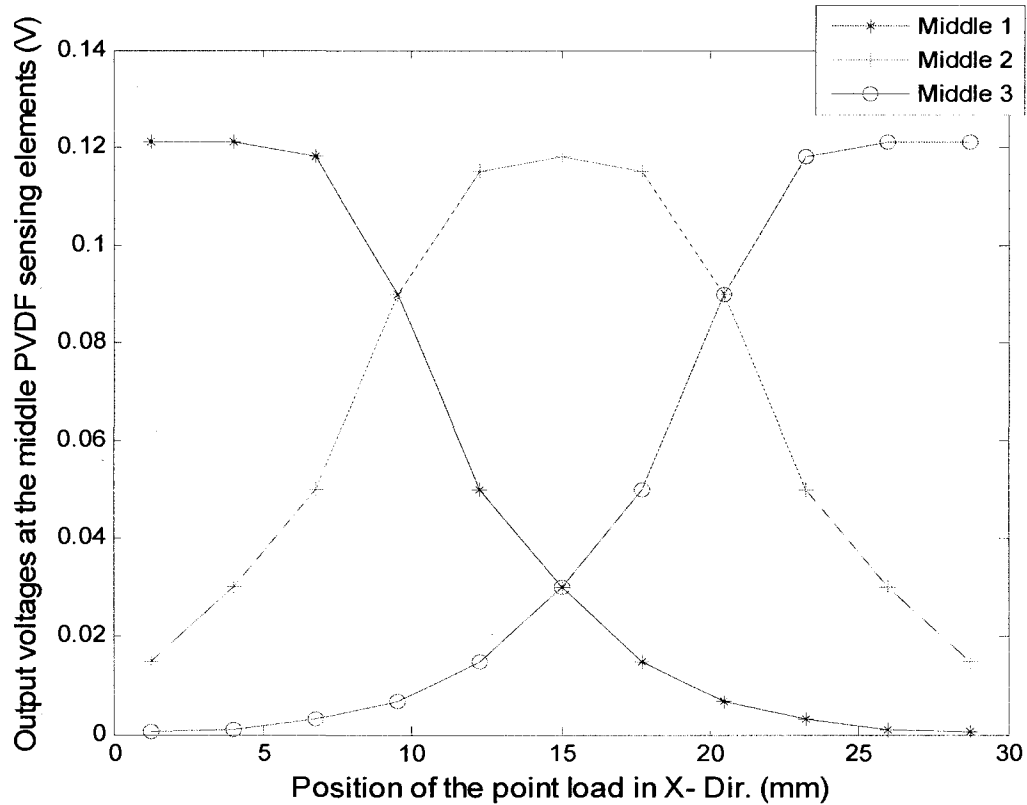


**Figure 3.33 – Output voltages at the middle PVDF sensing elements when a point load is applied along X- Direction**

As shown in Figure 3.32, the output voltages at Support11 and Support21 (the first support's pair) are always equal because location of the applied load is always on the center between both, and the compression load is divided equally. Also, the sensing elements Support12 and Support22 (the second support's pair) have the same output voltages for the same reason. This also applies to sensing elements Support13 and Support23 (the third support's pair) where both have the same output voltages.

From Figure 3.32, it is clear that the output voltages at Support11 and Support21 on one side, and at Support13 and Support23 on the other side, are a mirror image of each other and are equal when  $x = 15\text{mm}$  (center point of the plate). Voltages at Support11 and

Support21 are at a maximum when  $x= 4\text{mm}$  because the load is directly acting on the vertical line passing through its centers and becomes lower when the force location moves further away. The same rationale applies to Support13 and Support23 in which the output voltages are initially low and become higher reaching a maximum when the load is acting on  $x= 26\text{mm}$ . This is because the load is acting on the vertical line passing its centers directly. The load is directly on a vertical line passing through the centers of Support12 and Support22 when  $x= 15\text{mm}$ , and the output voltages on that sensing elements are at maximum.

For the middle sensing elements, Figure 3.33 shows the output voltage on Middle1 sensing element is at a maximum when the load is applied on  $x= 4\text{mm}$  and then becomes less when the load moves further away. The same applies for Middle3 where the output voltage is initially low and becomes higher reaching a maximum when  $x= 26\text{mm}$  because the load is directly the top. Output voltages at Middle1 and Middle3 are equal when the load is acting on the center point of plate ( $x= 15\text{mm}$ ), and the voltage at Middle2 is at its maximum at that position because the load is acting directly on top.

As previously shown and discussed, the location of the applied point load on the X-direction can be distinguished precisely using the curves of sensing element voltages versus the load location. In like manner, the location on the Y-direction can also be detected as discussed in section 3.4.2.1.

In conclusion, the accurate location of the point load can be detected on the plane XY since any point on the sensor's surface is active and responsible for transferring loading to the corresponding sensing elements. Locating the point load while grasping is directly indicates an embedded lump inside the grasped tissue and its location. Magnitude of the

point load with respect to the uniform distributed grasping load is indicates the size and the depth of this tumor inside the grasped organ.

### 3.4.3 Contacting Object and a Distributed Load

One of the major objectives of this sensor design is to measure and indicate the softness of contacting tissues by results obtained from simulation experiments.

The sensor design is modeled again with consideration of a contacting elastic object/ tissue and a PVDF layer at the middle. The contacting object/ tissue is modeled and connected to the design sensor, and finally the whole system is meshed. Modeling and meshing of the sensor with the contacting object/ tissue is performed by the sequential steps discussed in section 3.1.

The finer meshing is chosen to be on the PVDF layers with coarser meshing on the object/ tissue. The element size is changed to reach the maximum number of nodes supported by this software version. The model with the contacting object/ tissue is shown in Figure 3.34, and the whole system after meshing is shown in Figure 3.35.

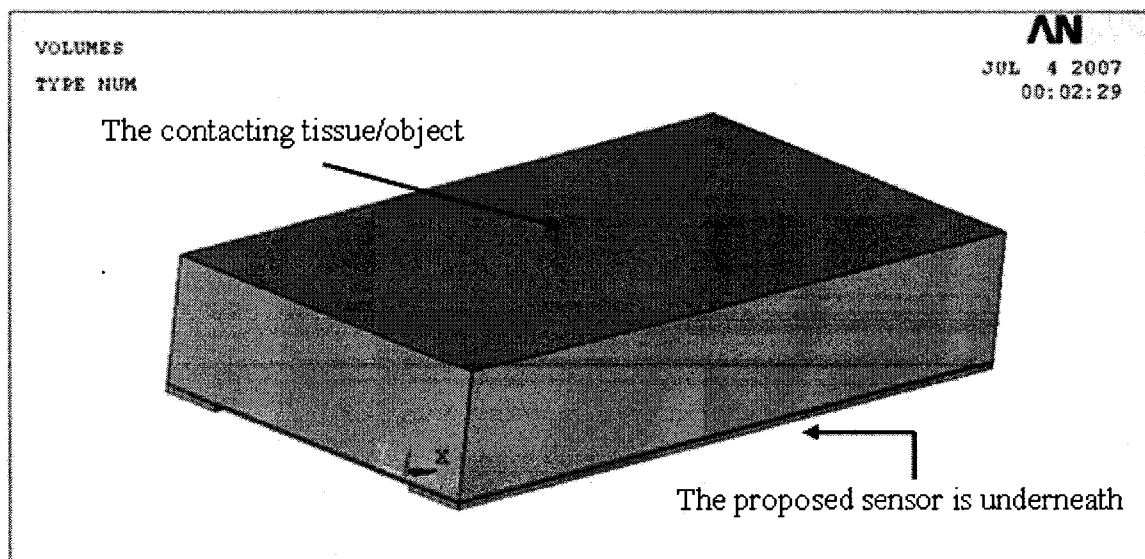
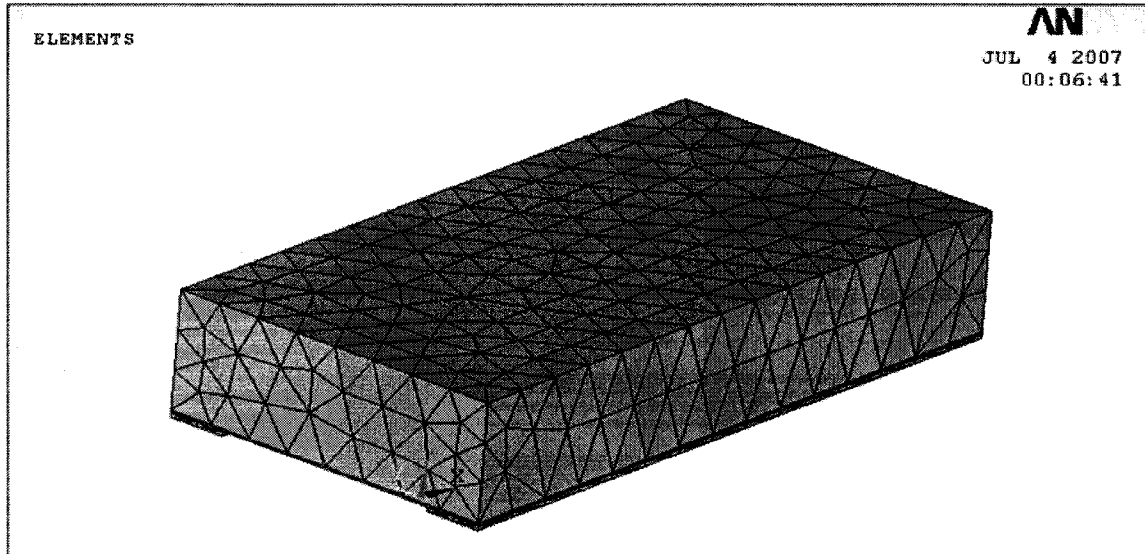


Figure 3.34 - An elastic object/ tissue is added and modeled with the sensor



**Figure 3.35 - Finite element meshing of the sensor with the contacting object/ tissue**

The contacting object/ tissue is modeled using SOLID45 element, which it has plasticity, creep, swelling, stress stiffening, large deflection, and large strain capabilities for 3-D modeling [81]. For tissues, Poisson's ratio is considered as 0.49 and different moduli of elasticity are examined.

Different loading magnitudes and different object/ tissue stiffness's are considered. The same boundary conditions which are discussed in 3.4 are applied with this model as well. Then the output voltages at the middle PVDF sensing elements are recorded. The applied uniform distributed load acts on top of the object/ tissue and the pressure is transmitted to the upper silicon plate of the teeth shape. Pressure on the base plate of the silicon will cause a deflection which is translated to stretching on the glued PVDF layer at middle. This stretching will create charges which are collected by the aluminum electrodes as a voltage. Figure 3.36 shows the deformation on the silicon layer and stretching of the middle PVDF layer. The output voltage profile on the three sensing elements of the middle PVDF is shown in Figure 3.37.

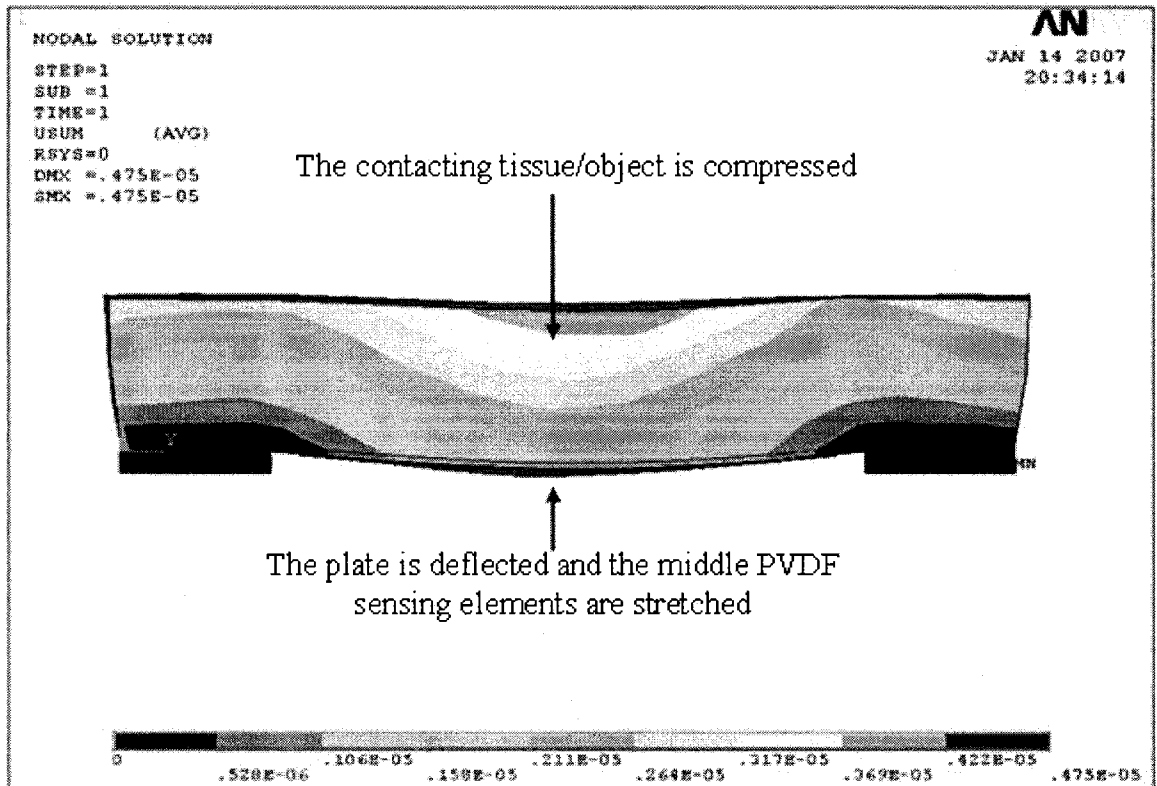


**Figure 3.36 - Deflection of the sensor when a distributed load is applied on top of the object**

As proved in Section 2.4.2, soft contacting object/ tissue cause a large deflection of the silicon layer. Consequently, by large stretching of the glued PVDF at middle, a high voltage on the PVDF layer at middle is expected. However, hard contacting object/ tissue means smaller deflection of the silicon and smaller stretching of the PVDF results in lower than expected voltage.

Different moduli of elasticity of the contacting object/ tissue are considered. At each modulus of elasticity of the contacting object/ tissue, and keeping the same distributed pressure magnitude, the system is simulated and the results are recorded.

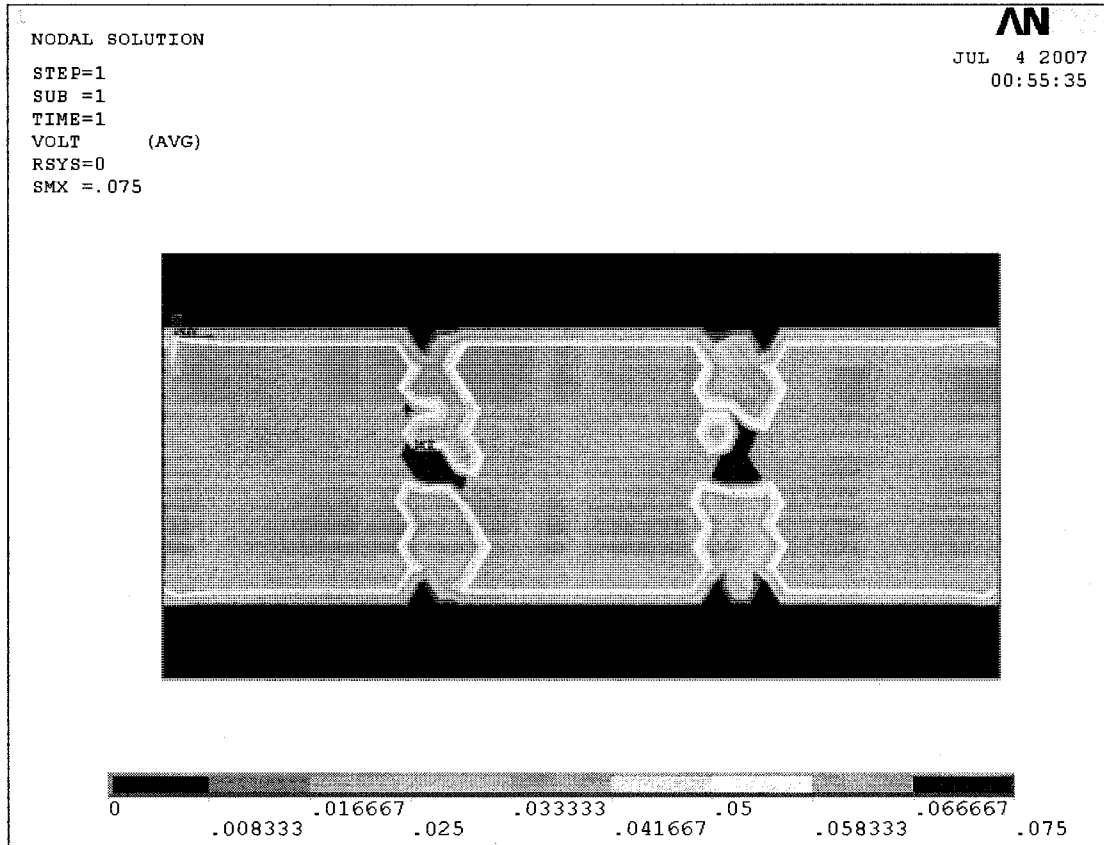


**Figure 3.37 - Output voltage at the middle PVDF sensing elements**

At first, a distributed load of 5 N magnitudes is applied on the top of object/ tissue as a reasonable grasping force during surgery [14]. Then output voltages on the middle PVDF sensing elements versus a different modulus of elasticity of the object/ tissue are recorded. Figure 3.38 shows the relation curve between output voltage and the different modulus of elasticity of the contacting object/ tissue.

Moreover, different grasping forces are considered in order to check the sensor sensitivity. At each grasping force, the output voltages at different modulus of elasticity of the contacting object/ tissue are recorded. The relation between the output voltage and the modulus of elasticity of the contacting object/ tissue at different grasping forces are shown in Figure 3.39.

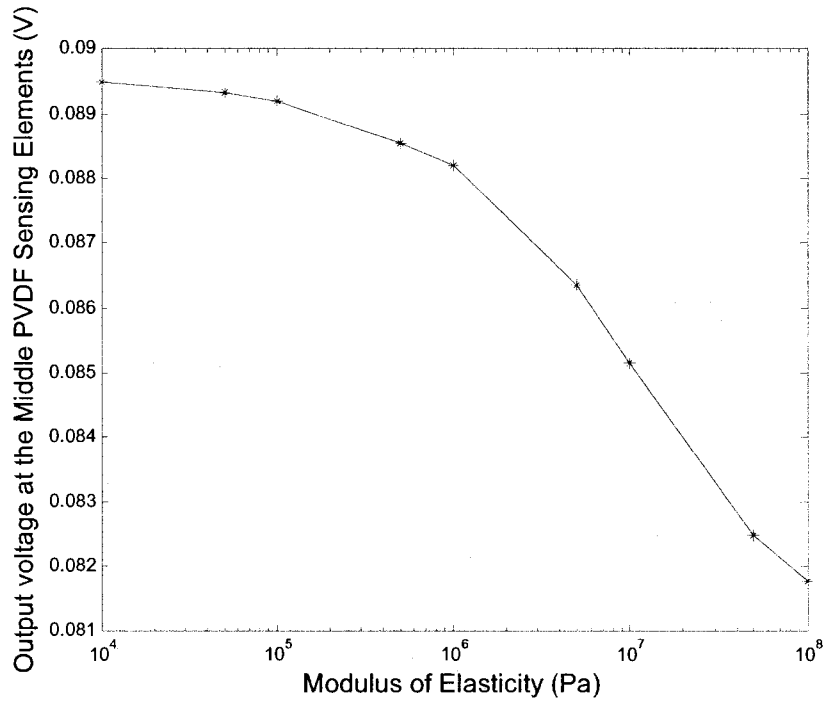


**Figure 3.38 - Output voltages at the middle PVDF sensing elements versus different object/ tissue stiffnesses at 5 N grasping load**

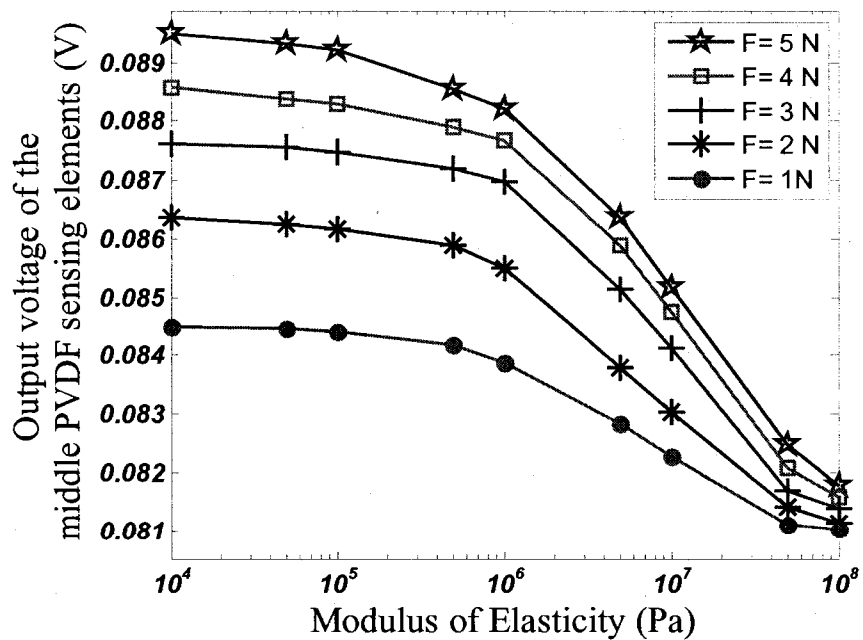


**Figure 3.39 - Output voltages at the middle PVDF sensing elements versus different object/ tissue stiffnesses at different grasping loads**

As shown in Figure 3.35, output voltage at the middle PVDF decreases with harder contacting tissues. Output voltages at different tissue modulus of elasticity are reasonably varied and can be detected.

In Figure 3.39, it is clear that the sensor sensitivity is better with higher grasping forces. Given such a high grasping load, the sensor can easily detect the contacting tissue softness. On the other hand; with low grasping load, the sensor is less sensitive to the softness of contacting tissue and it is harder to differentiate between induced signals at different tissue hardness. That is reasonable and comparable to the manual palpation by a surgeon when using his/her fingers; where palpations needs enough compression forces to distinguish the object stiffness and any abnormality inside.

The next chapter presents the sensor layers microfabrication in detail, followed by a discussion on the assembly of the different layers.

### **3.5 Summary**

This chapter started with the sensor finite element modeling procedure using software ANSYS 10. The sequential steps of the graphical mode of ANSYS modeling were discussed in detail and then the used elements for the different layers modeling were addressed. The coupling method which has been used for piezoelectricity modeling was discussed and the associated matrix equations reported. After modeling, parametrical studies of simple plate dimensions as a simplified model of the sensor were studied. The parametrical study resulted with a graphical relation between the proposed sensor dimensions for any further different designs sizes with the same loading range. Distribution of the teeth on the top of silicon layer was studied and optimized. Also, the

PVDF layer orientations, as well as the sensing elements distributions on the PVDF layer, were studied and optimized. Then the relation between hidden features inside the grasped organ and a point load was verified. After explaining the structural and electrical boundary conditions, many simulations and sensor performance evaluations were carried out and discussed. Calibrations curves were established and the sensor ability for grasping loads and low magnitude loads, comparable to blood vessels pulse measurements, were verified. Then, the sensor ability of point load detection in two dimensions was confirmed. Finally, the sensor remodeled with a contacting tissue consideration, and the sensor performance on the contacting tissue softness estimations was established.

## Chapter 4 – Sensor Microfabrications and Assembly

The sensor microfabrications and assembly are discussed in this chapter. This chapter is divided into three sections. The first section deals with the silicon microfabrications using MEMS technology. The second section illustrates the sensing elements microfabrication by PVDF patterning using MEMS. On the last section, assembly of the different sensor parts is negotiated.

### 4.1 Silicon Layer Microfabrications

Upper layer of the proposed sensor is micro-machined from silicon wafer, along 100 orientations, using MEMS technology. It is anisotropically etched to form the rigid tooth-like structures; each tooth has a trapezoidal prism shape having anisotropic etching angle ( $54.74^\circ$ ) on the side walls. The silicon wafer thickness is  $500\ \mu\text{m}$ , which is the most commercially available thickness and is another important factor in the cheap manufacturing cost of this sensor. Height of the prism tooth is equal to  $200\ \mu\text{m}$ , also the depth of the etched U-channel on the back is  $200\ \mu\text{m}$ , and finally the remaining thickness of the etched layer is  $100\ \mu\text{m}$ .

(100) Silicon wafer is chosen, that to have the prism tooth shape with  $\{111\}$  side walls inside the Tetra-methyl ammonium hydroxide (TMAH) etching.

Microfabrications of the silicon is done by sequential steps, starting with the proper cutting of silicon samples, and then cleaning followed by thermal oxidizations. After that, photolithography process which discussed in section 1.4.4 is performed starting by photoresist deposition on the silicon surfaces and followed by soft baking of the sample

and then UV exposure followed by photoresist developing and consequent with hard baking. After hard baking, etching of the silicon oxide is taken place and finally removal of the photoresist. Core and last step is the silicon anisotropic wet etching as discussed in section 1.4.2. These sequential steps of the silicon microfabrications are discussed in details within the following sections.

#### **4.1.1 Silicon Oxidizations**

At first, the wafer is cleaned by deionized (DI) water and nitrogen gun on both sides, and then it is wet oxidized in oxidization furnace. Oxidization furnace is shown in Figure 4.1. Oxidization process is done at  $1100\text{ C}^{\circ}$  for two hours to build-up a silicon oxide layer of around  $1.2\mu\text{m}$  thickness at each side. Cares are taken to oxidize both sides equally by holding the samples vertically; also the care is taken about the gradual entering of the wafer inside the furnace at beginning, and the gradual removing of wafer outside of furnace at the end; as shown in Figure 4.2. The created layer of oxide of the thickness  $1.2\mu\text{m}$  will play the hard mask role for silicon bulk etching on both sides. After completing this step, the next is photoresist deposition and the soft baking.

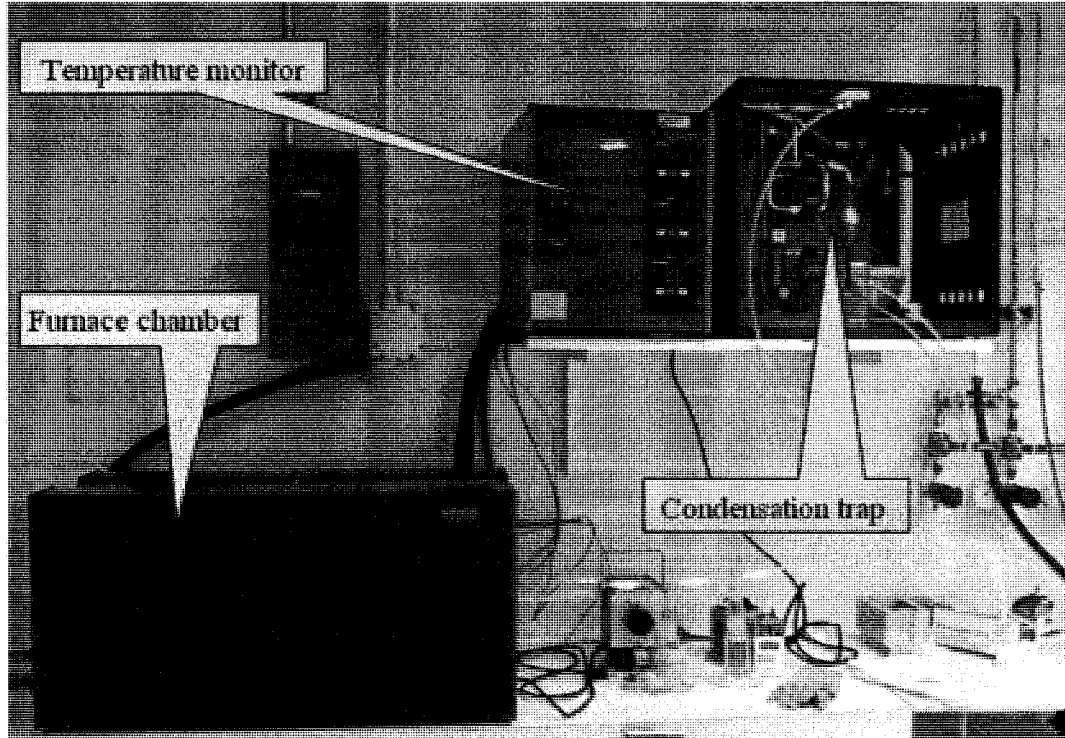


**Figure 4.1 – Oxidation furnace set-up**

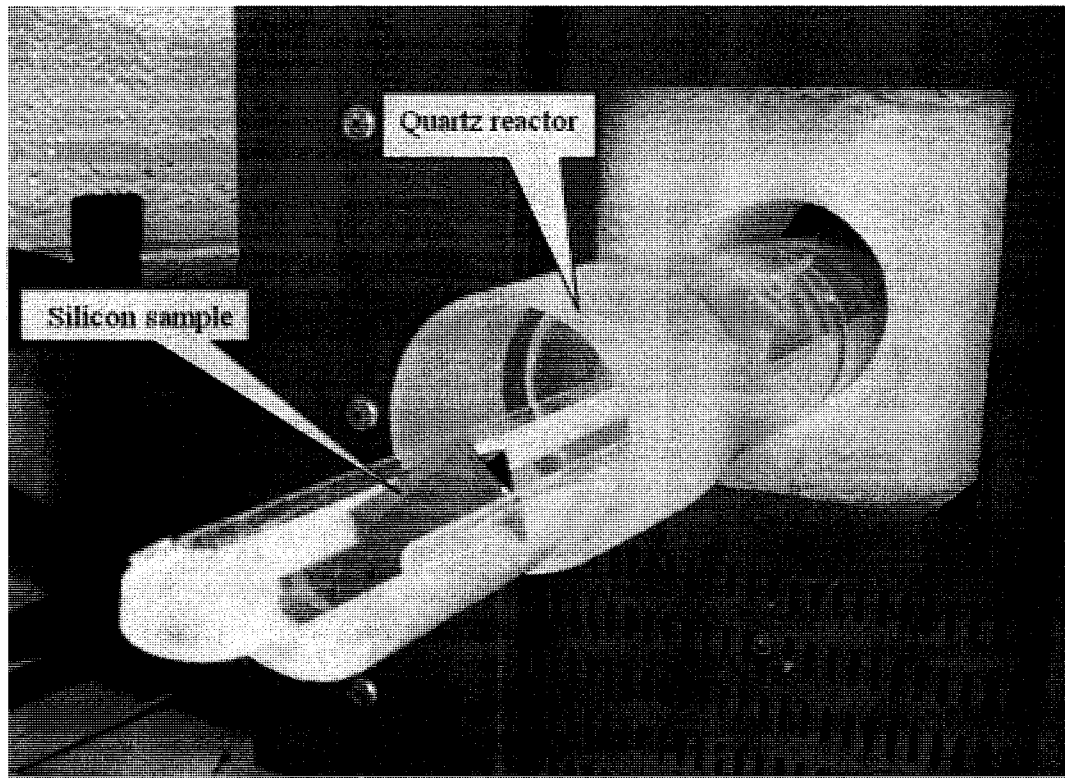


**Figure 4.2 – Samples are vertically positioned using a quartz holder**

#### **4.1.2 Photoresist Deposition and Soft Baking**

After finishing oxidization, photolithography stage is the next. It is applied on the both sides of silicon sample. That because the silicon sample is to be etched on each side; etching of the teeth shapes on the polished surface, and etching of the supports on the other side.

The first two steps of photolithography process are the photoresist deposition and the soft baking. These two steps is performed twice, the first time is carried on the back of the sample (the unpolished surface). Back of the silicon wafer is covered by a layer of S1813 positive photoresist (PR) after careful cleaning of samples using nitrogen gun. Photoresist deposition is done by spin coating, which that by holding the sample face on the spinner using the pneumatic vacuum chuck, and then the rotation is fixed around 3000 rpm. After that, about three equal drops of PR are released continuously on the wafer back and the sample is kept rotating with a total time of approximately 45 second. Spinner is shown in Figure 4.3.

After spinning, the wafer with the deposited PR layer is soft baked inside baking oven at temperature of 110 C° for around forty minutes; baking oven is shown in Figure 4.4.

The second turn of these two steps is performed on the polished face following the same procedure. The polished face of the sample is covered by photoresist and followed by soft baking again as discussed on the previous stage.

After finishing of these two steps of photolithography, the third step is to expose the deposited photoresist on each side by UV light through masks.

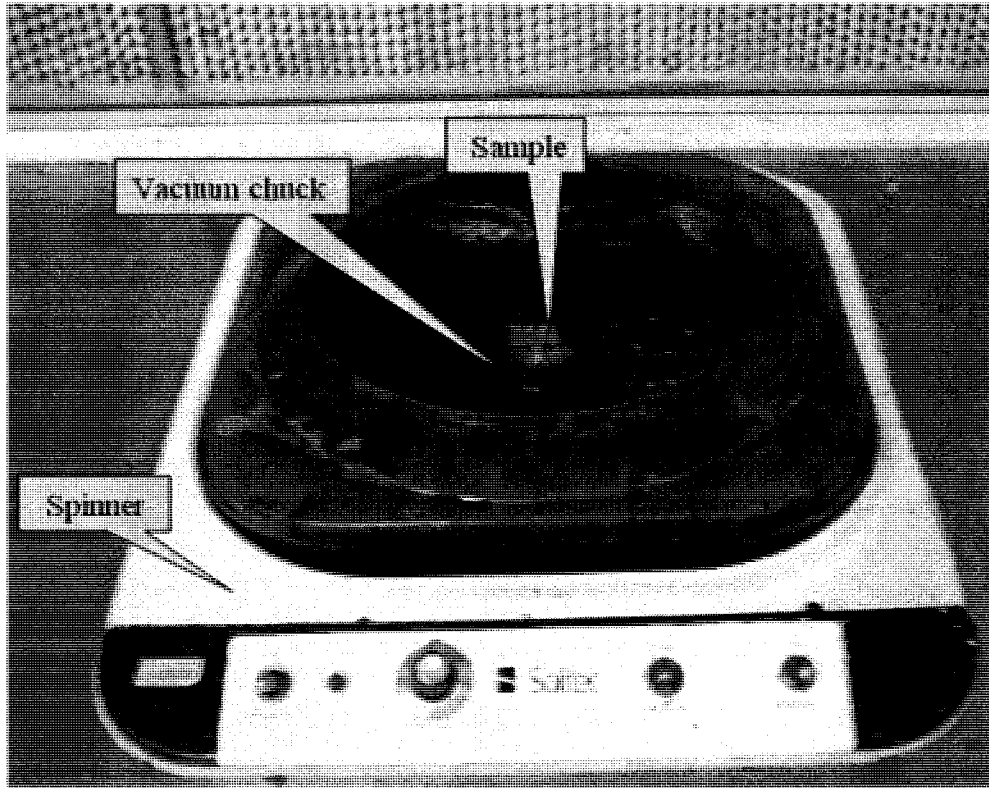


**Figure 4.3 – Photoresist deposition on the sample by spinning**

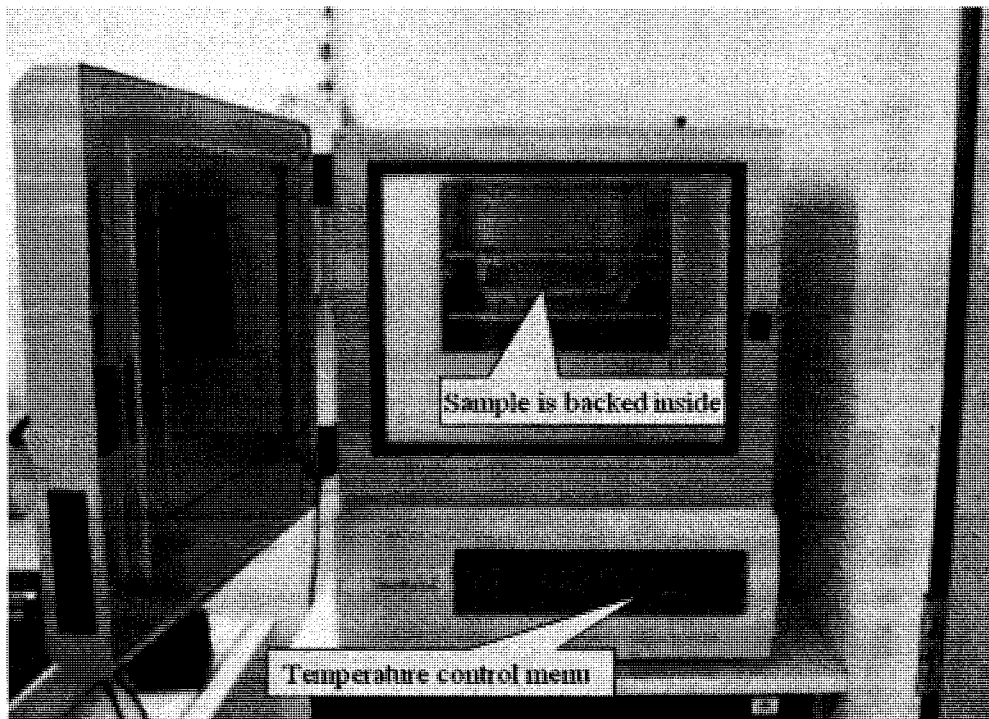


**Figure 4.4 – Baking oven**

### 4.1.3 Masks Design and the Ultra-Violet (UV) Exposition

For this sensor design, two different light field masks are used; the first mask is used with the polished face of the sample to represent the teeth shapes of the sensor, and the second mask is used to represent the U-channel and the supports on the back of the sample. The two masks are prepared with proper dimensions and plotted on a glass mask. The first mask is shown in Figure 4.5.

As shown in Figure 4.5, the mask is designed with proper dimensions to have the same dimensions of the sensor and the teeth specifications. The convex corner is protected and compensated using a method for convex corner compensation inside TMAH etching [84-90]. For our design, the depth of etching is 200  $\mu\text{m}$ , and using the given equation on the presented compensation method, the length of the compensator edge (a) which shown in Figure 4.5 is equal to 367  $\mu\text{m}$ . The method used for convex method compensation is illustrated on Figure 4.6.

The mask is aligned to the wafer carefully to have the  $\{111\}$  side walls; the samples should be cut to have either parallel or perpendicular edges to (100) wafer flat as shown in Figure 4.7. And that is followed by UV exposure for 15 seconds; UV aligner is shown in Figure 4.8. By finishing the UV exposure, the mask shape is transferred to the PR layer.

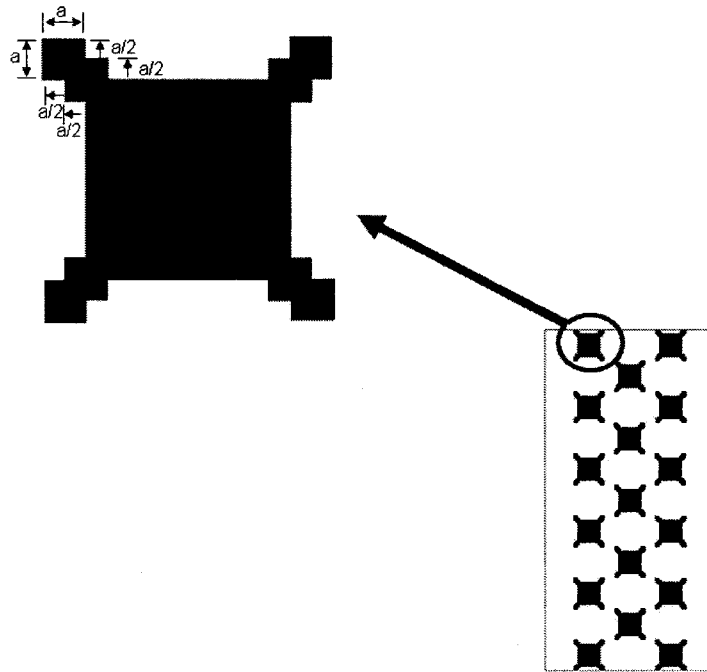


Figure 4.5 – The first light field masks for teeth microfabrications

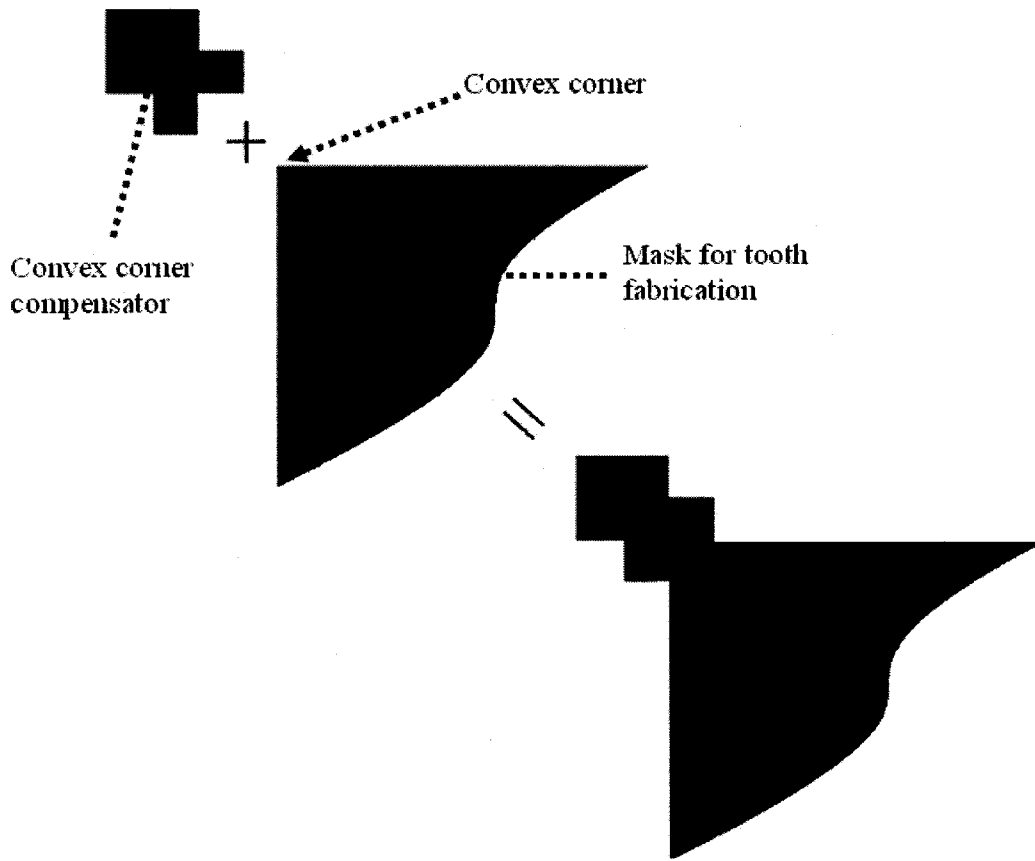
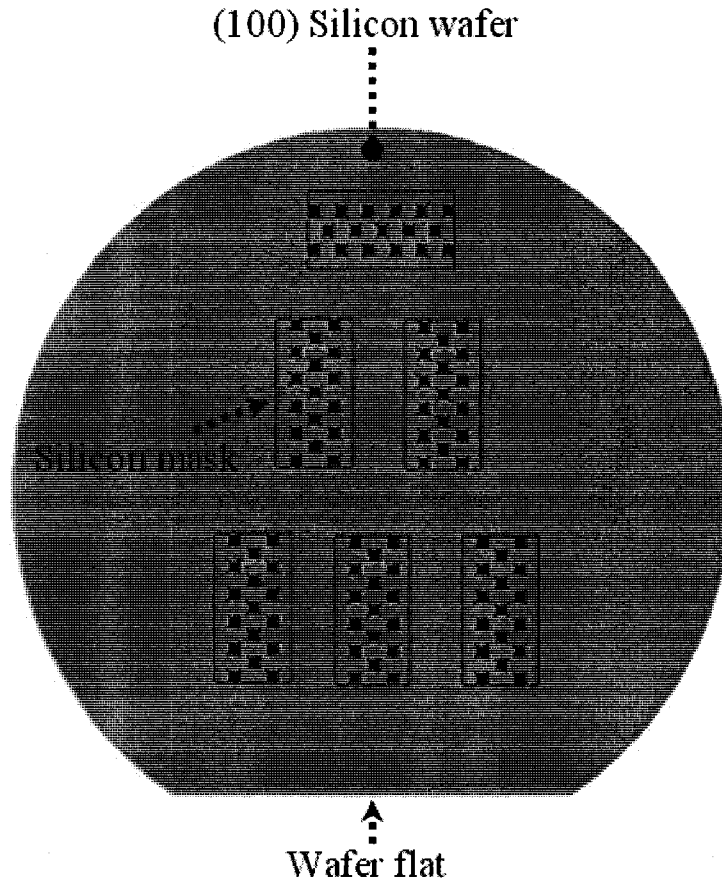
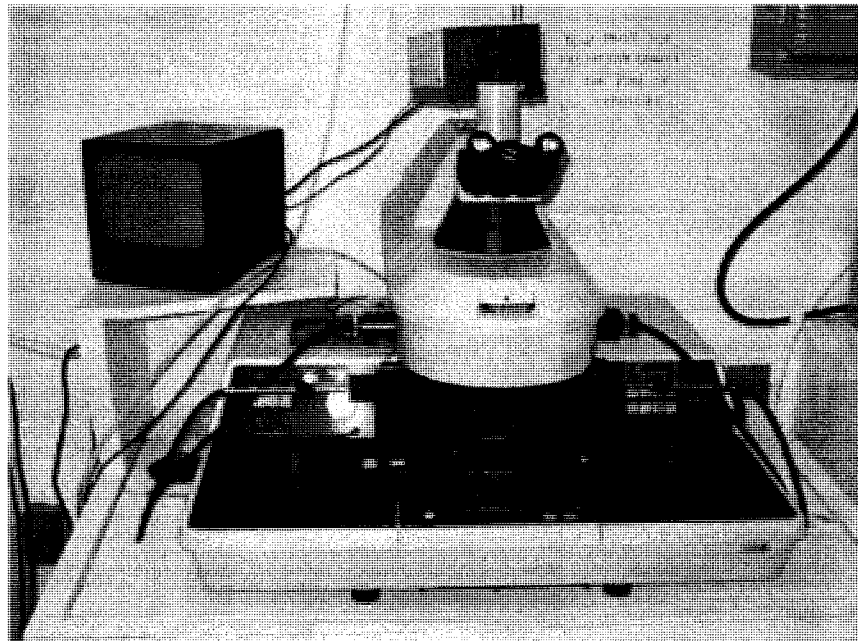


Figure 4.6 – Details of the convex corner compensation method



**Figure 4.7 – Silicon masks edges are aligned with the wafer flat**



**Figure 4.8 – Quintel double-sided mask aligner**

Using the same procedure of alignments and UV exposure, the PR on back of the sample is exposed after aligning the second masks which responsible to represent the U-channel. The second mask is shown in Figure 4.9.

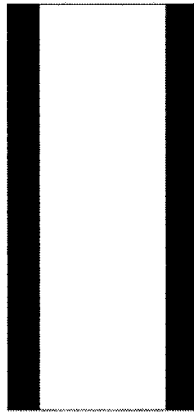


**Figure 4.9 – The second light field masks for supports microfabrications**

After finishing of UV exposing, the masks shapes are transferred to the PR layers at each side. The next step of the photolithography is to develop the PR layers and hard baking.

#### **4.1.4 Photoresist Developing, and Hard Baking**

After UV exposure, the PR is developed and the exposed PR regions are removed. Unexposed regions of the PR which were protected by the black areas of the mask while exposing are remains and are playing as the hard mask while the silicon oxide etching.

PR is developed using an appropriate PR developer, that by dipping the samples on the developer until the pattern become clear to the human eyes. And then dipping and rinsing inside a beaker of DI water for few minutes. Finally, the sample is hard baked on the backing oven at temperature of 110 C° for around forty minutes.

After finishing of hard baking, the remaining PR regions will protect etching of the oxide underneath, but the clear areas of oxide will be etched out as discussed on the following section.

#### **4.1.5 Silicon Oxide Etching**

The next step is the wet etching of silicon oxide to form the hard mask of silicon bulk etching. First of all, a buffered HF (Hydrofluoric acid) is prepared by adding one part of 49% HF to four parts of 40% NH<sub>4</sub>F (Ammonium fluoride) inside a Teflon beaker of suitable size. And then one part of 49% HF is added to fifty parts of water inside another Teflon beaker. Moreover, two glass beakers are filled with DI water.

Silicon oxide etching is started by inserting the sample inside the buffered HF for around one to two minutes. Then the sample is cleaned by inserting inside the first beaker of DI water. Subsequently by inserting the sample inside the third beaker which contains HF and water mixture, keeping the sample inside until completely etching of the unprotected silicon oxide, it takes one minute or more. The procedure can be repeated many times until making sure that the oxide is completely etched on the PR opening. Oxide wet etching procedure is shown in Figure 4.10.

The oxide etching can be checked if it is completely done or not by using hydrophilic and hydrophobic phenomena, that's by notice the water adherence on the sample surface after dipping inside the second DI water glass beaker. If there is a noticeable layer of water sticking on the whole surface, then the oxide did not etched completely yet, that because silicon oxide is a hydrophilic material and holds water drops. And if the surface is found dry except few drops that prove the complete etching of oxide because silicon is a hydrophobic material and dose not hold water drops. Finally and after verifying the

complete oxide etching, the sample is cleaned by insertion inside DI water beaker for few minutes. And then PR is removed by acetone soaking until fully removal.

The last step of silicon layer microfabrication is the silicon anisotropic etching inside TMAH bath; the etched silicon oxide will be the hard mask for this silicon bulk etching.

The next section is discussing the silicon bulk etching.

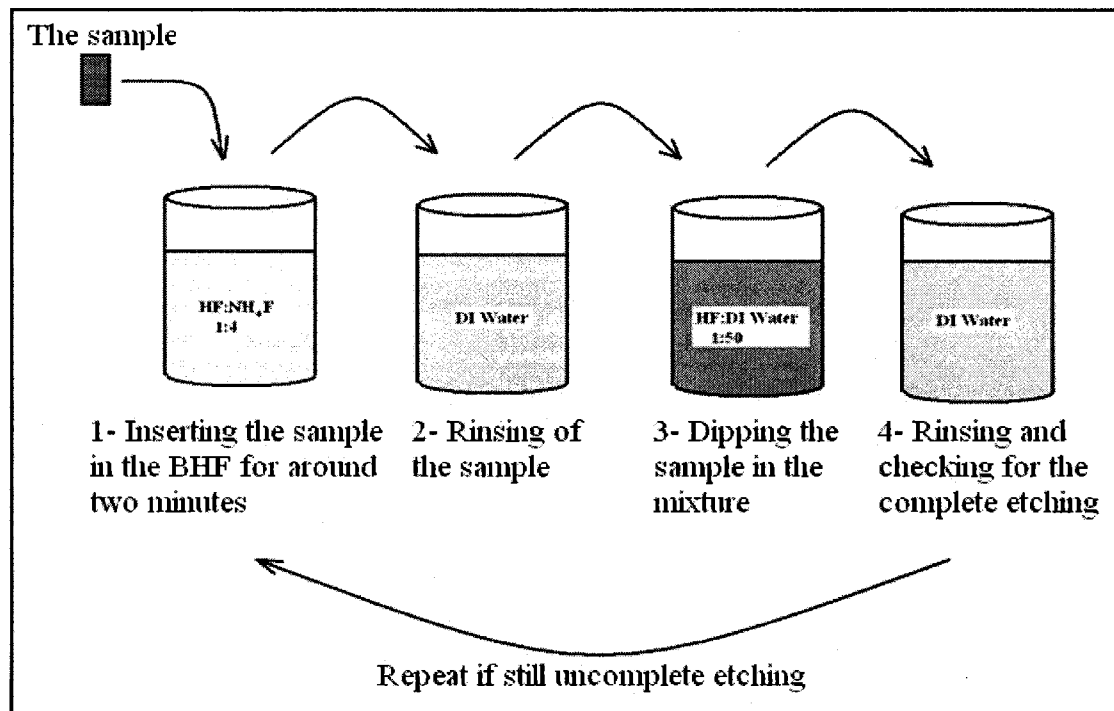


**Figure 4.10 – Procedures of the silicon oxide wet etching**

#### **4.1.6 TMAH Silicon Etching**

After forming of the hard silicon oxide mask on the previous step, the silicon wafer is bulk etched inside the TMAH bath. A glass beaker of proper size is prepared and filled with a suitable amount of TMAH % 25, and then the sample is inserted inside the beaker,

and the beaker is held inside the TMAH bath with temperature of 80C°. TMAH bath is shown in Figure 4.11.

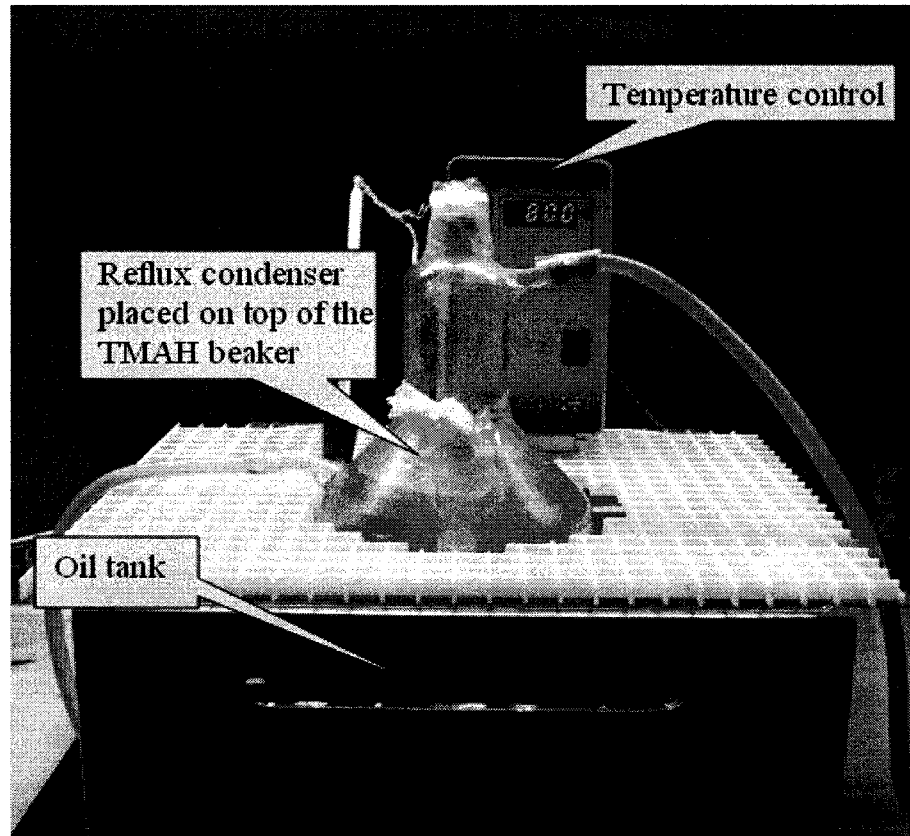


**Figure 4.11 – The TMAH bath set-up**

To guarantee good etch rate, the sample were held vertically on a special holder to make sure that the etch rate on both sides is equal. Furthermore, the etch rate is the best with the vertical position of sample, that because faces of sample are parallel to the TMAH flow and circulation. Moreover; to assure best etch rate at the given temperature and TMAH concentrations; a rotating magnet stirrer is inserted on the bottom of beaker to rotate and move TMAH inside the beaker and increase the kinetics of TMAH molecules to increase the etch rate.

The expected etch rate of silicon in  $\langle 100 \rangle$  direction on the ideal conditions is around  $24 \mu\text{m}/\text{hour}$  [84-90]. Ideally, it's expected to keep the beaker inside the TMAH bath for about eight and half hour's to etch the  $200 \mu\text{m}$  on each side of the silicon sample.

After two hours of TMAH etching was running, the sample is checked under the microscope and found around  $38 \mu\text{m}$  is etched on each side. As result, with this etching conditions, the etching rate in  $\langle 100 \rangle$  direction is around  $19 \mu\text{m}/\text{hour}$ , and it is expected to spend eight and half hour's more inside the TMAH bath to have the desired etching depth.

After carrying out the ten hours and half of the sample inside running TMAH bath, the etching depth is checked under the microscope and the  $200 \mu\text{m}$  etched depth on each side is verified. The front side of the sample which contains the fabricated teeth is shown in Figure 4.12, and the back of the sample which expresses the channel shape forming the supports of the sensor is shown in Figure 4.13.

Figure 4.14 is showing a picture taken by microscope; it is showing one tooth of the sensor and the  $\{111\}$  planes of the side wall with the inclined angle  $35.3^\circ$ . Moreover, the microscope magnification is concentrated on one side of one tooth to check the wall accuracy, the wall edges straightness, and the tooth height. The magnification is focused once on the upper edge of the side wall and then on the lower edge of side wall. Both edges are shown in Figure 4.15.

The etch rate of silicon oxide inside TMAH bath is roughly around  $6 \text{ nm}/\text{hour}$  [91]. For that, after the ten and half hours of silicon etching, it is expected to have about  $63 \text{ nm}$  etched out of the  $1.2 \mu\text{m}$  oxide layer at each side. Because that, the silicon oxide is valid

as a hard mask for this silicon layer microfabrications, and the hard mask can be shown in Figure 4.14 is survived after the TMAH silicon etching.

Fabricated teeth of height 200 micron

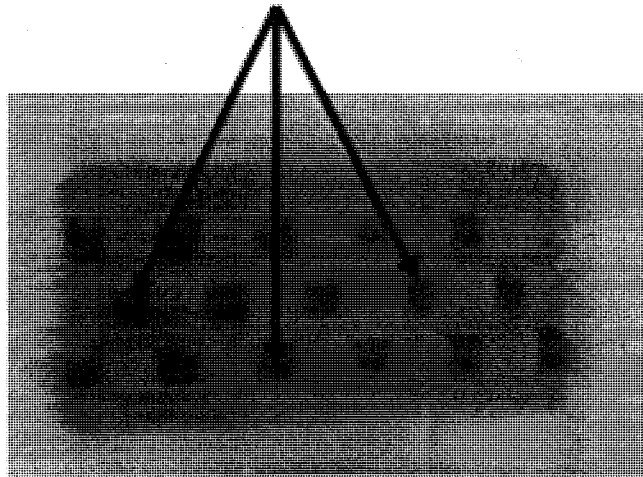


Figure 4.12 – Top view of the sample showing the teeth shapes

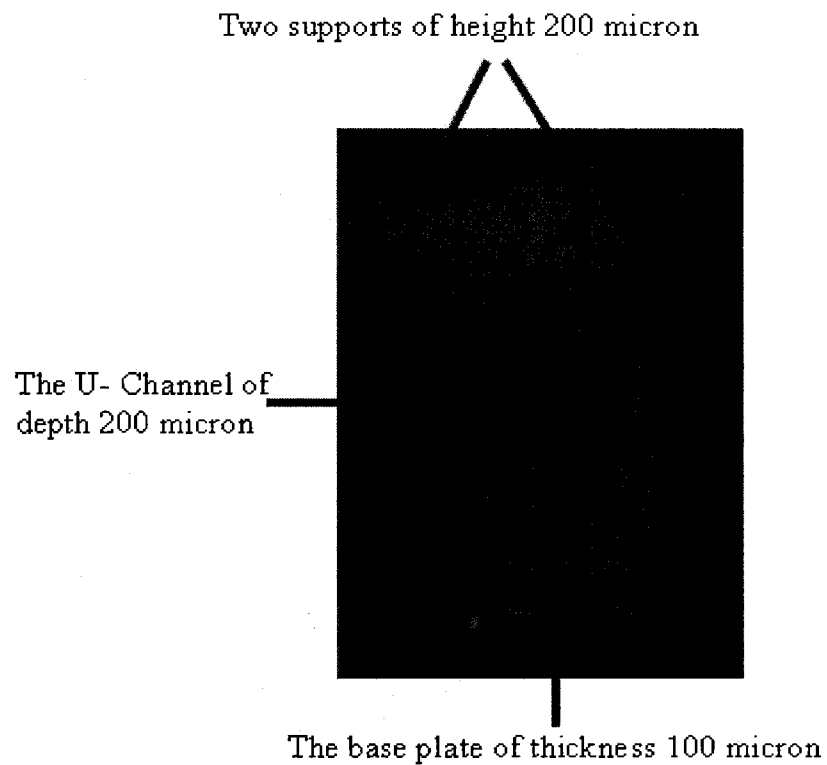
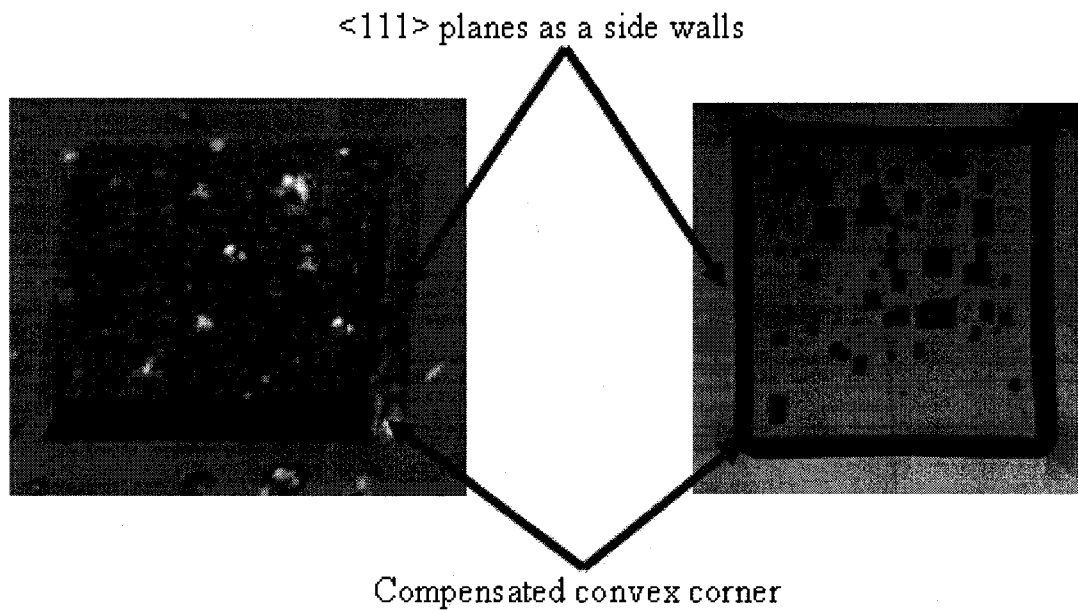
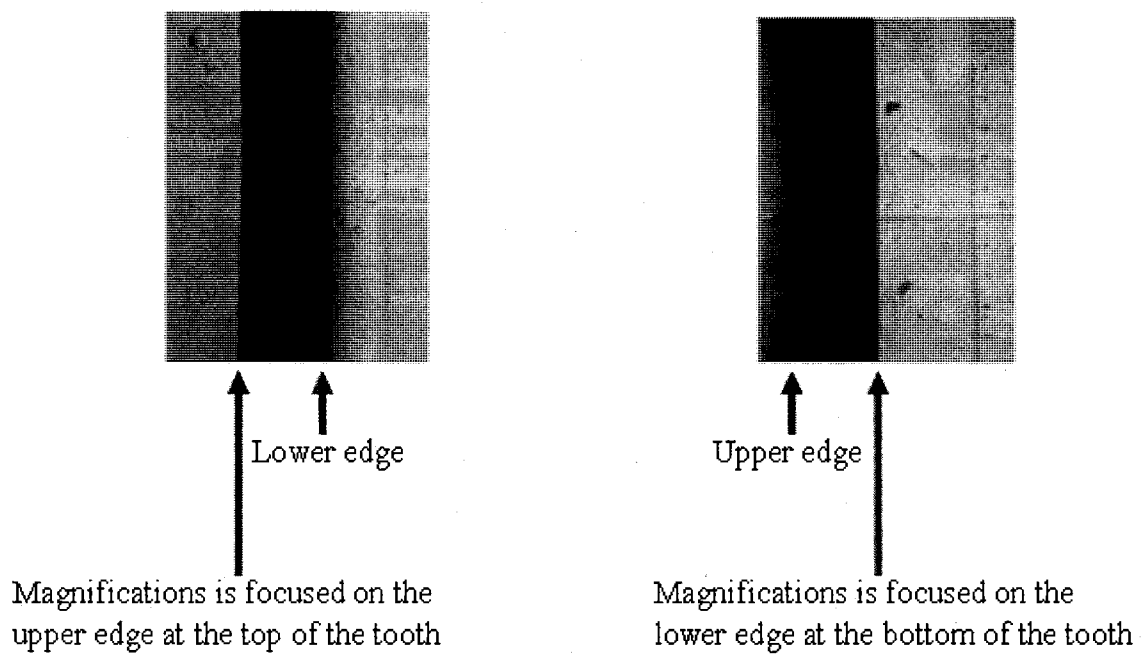


Figure 4.13 – The bottom view of silicon showing the channel and supports



**Figure 4.14 – The  $\langle 111 \rangle$  side walls and the compensated convex corners of the microfabricated teeth**



**Figure 4.15 – Upper and lower edges of the tooth side wall which is used to verify the tooth height**

A cross-sectional view of a tooth is taken by microscope showing the plate and the trapezoidal shape of the tooth with the  $\{111\}$  planes. The cross-sectional view is shown in Figure 4.16.

Finally the remaining oxide can be removed using the same procedure of silicon oxide etching which discussed on section 4.1.5.

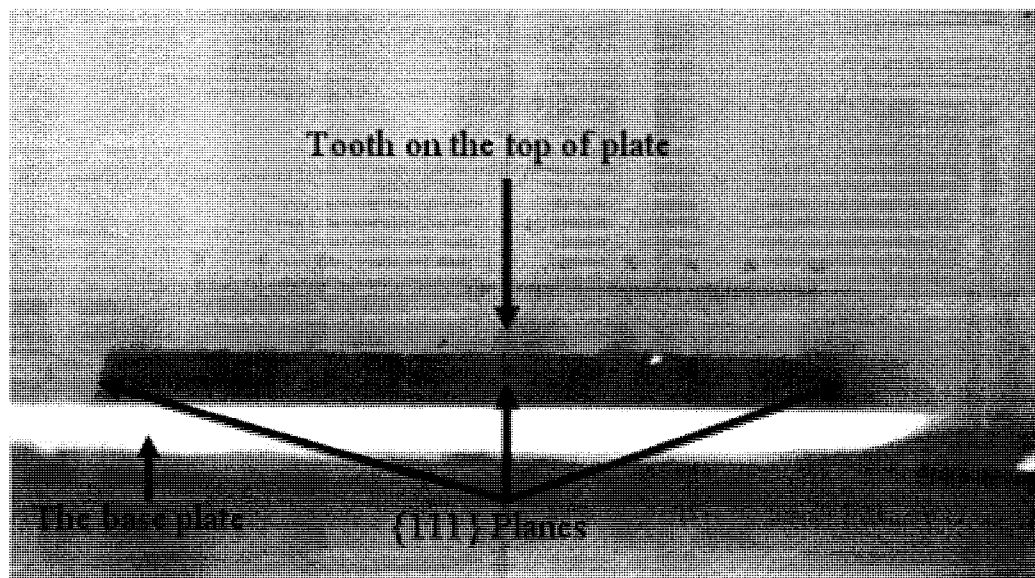


**Figure 4.16 – Cross sectional view of the microfabricated silicon showing a tooth cross-section**

## **4.2 PVDF Layer Microfabrications**

Microfabrications of the PVDF layer to have the desired sensing elements configurations are presented in this section. It is processed using the same MEMS technology steps including the photolithography steps.

The process starts with the proper cutting and cleaning of the PVDF sample, and then the photoresist is deposited and the sample is soft baked. After preparing of the mask, the

sample is exposed and then the photoresist is hard baked after developing. After hard baking, the aluminum cover is patterned and then photoresist is removed.

#### 4.2.1 Sample Preparations

A sample of aluminum ( $Al$ ) metalized PVDF film is prepared and cut with a rectangular shape and suitable dimensions. Care is taken to have the drawn direction ( $d_{31}$ ) of the PVDF strip in parallel with the width direction (the short dimension) of the sample. The sample has the dimensions  $30 \times 15 \text{ mm}^2$  to represent the PVDF layers at middle and supports. One side of this sample will be patterned to represent the active sensing PVDF elements at the middle and supports. The second side of the PVDF layer is kept without patterning to represent the common electrode for all sensing elements. The PVDF sample is shown in Figure 4.17.

The PVDF sample

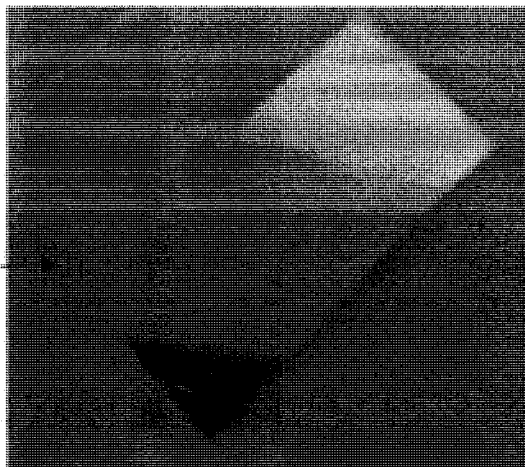


**Figure 4.17 – A typical metalized PVDF sample of  $25 \mu\text{m}$  thickness**

After cutting preparations, the sample is cleaned using DI water and then dried by the Nitrogen gun. The next step is the photoresist deposition; it is discussed on the next section.

#### 4.2.2 Photoresist Deposition and Soft Baking

On contrary of silicon samples; PVDF sample cannot be coated by Photoresist material directly on the spinner, that because PVDF film is very thin and flexible to be held on the suction chuck of spinner. For that, a slide of glass is prepared to support the PVDF sample while spinning, baking, UV exposure and patterning. A slide of glass with proper size is prepared and cleaned using DI water and finally dried using Nitrogen.

The PVDF sample is glued to the glass slide using photoresist, for that the glass slide is held on the spinner chuck and coated by a layer of photoresist (PR) as the same procedure discussed earlier for silicon spinning. After the PR layer is built on the glass slide, the glass slide is removed from vacuum chuck and the PVDF layer is carefully attached to its top.

After the previous step, the PR between glass slide and the PVDF is working as good uniform glue as well as giving the protection to  $Al$  coating of the contacting face of PVDF while  $Al$  patterning. Care is taken while gluing of the PVDF on the glass slide especially on the sample edges. The glass slide with the glued PVDF is baked on the baking oven on a  $50C^{\circ}$  temperature for few minutes to make sure that the PVDF is well glued on the glass slide and stick probably.

After getting the sample out of the baking oven, the glass slide with the glued PVDF is held on the spinner, and the S1813 positive photoresist (PR) is deposited on the PVDF surface by releasing three equal continues drops of the PR on the PVDF while rotating at 3000 rpm. After that, the sample is kept rotating for around 45 seconds and then removed from the spinner.

After PR spinning, the sample is soft baked inside baking oven at  $50 C^{\circ}$  for 40 minutes.

### 4.2.3 Applied UV, PR Developing, and Hard Baking

A mask for the sample is designed and prepared and finally plotted on a glass mask. The mask is shown in Figure 4.18. The mask is aligned to the sample carefully and then the sample is exposed to UV light for 15 seconds on the same aligner used for silicon samples previously.

After the UV exposure, the mask shape is transferred to the PR layer. And then the sample is developed by dipping inside a beaker filled with PR developer for around 1~3 minutes until the pattern became clear. Then, the sample is stored inside DI water beaker for few minutes. That followed by hard baking of the sample inside baking oven at 50 C° for 40 minutes. In Figure 4.19, the sample after hard baking stage is shown.



**Figure 4.18 – The light field masks which is used for patterning the PVDF sample**

The last step of the sensing elements microfabrication is the aluminum ( $Al$ ) patterning, this step is discussed on the next section.

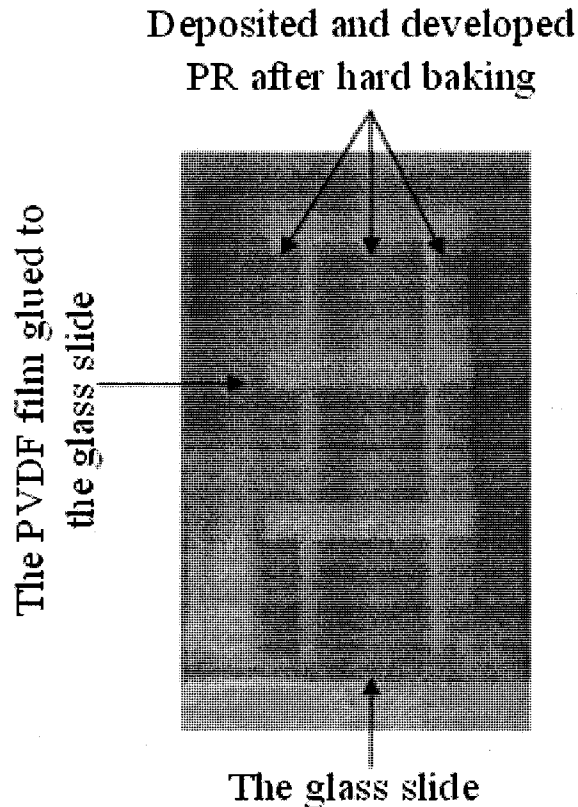


**Figure 4.19 – The PVDF sample after hard baking**

### **4.2.3 Aluminum Etching**

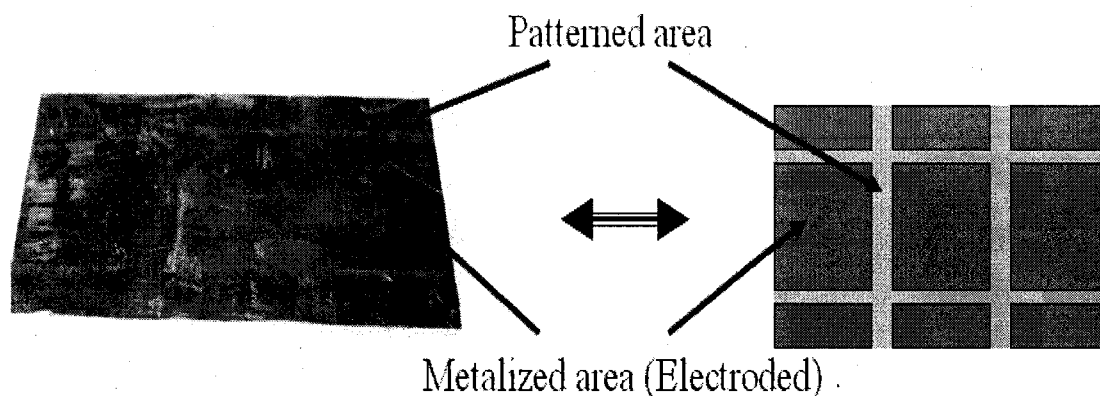
The next step is aluminum ( $Al$ ) etching, where the covered  $Al$  regions by the remaining PR are protected and will not be etched out with  $Al$  etchant since PR is resisting  $Al$  etching [92]. On other hand,  $Al$  coating will be etched out on the clear and unprotected areas of PR.

Appropriate glass beaker is prepared and filled with a commercial aluminum etchant type-A solution [92] and heated on a hot plate until temperature of  $50\text{ C}^\circ$ . After that the sample is rinsed inside the etchant beaker for about one minutes or more until the aluminum is etched on the clear areas.

After visual noting of *Al* coating etching on the unprotected areas (etch rate around 600 nm/ min [92]), the sample is taken out of *Al* etchant and stored inside DI water beaker for few minutes. Finally the sample is dipped on acetone to remove the remaining PR layers and separate the PVDF layer than the glass slide.

The PVDF sample after patterning can be shown in Figure 4.20; the figure clearly showing the etched strips of *Al* coating and the remaining electrodes. Three remaining electrodes cover separate regions of the top PVDF at the left and the right sides to representing three active regions of sensing elements at each support. Also three regions at the middle are kept metalized to represent three active regions of sensing elements at middle of the base plate.

The bottom *Al* coating of the sample is kept without any patterning to represent a common electrode for all active sensing element regions.



a) Patterned PVDF film

b) Designed PVDF sensing elements

**Figure 4.20 – The patterned PVDF film**

### 4.3 Sensor Assembling

Once the three layers of the sensor are completely microfabricated and realized, the next step is to assemble them.

At first, a thin layer of nonconductive glue is deposited uniformly at the bottom of the etched U- Channel on the back of silicon layer, and kept for 5 minutes on the baking oven at 50 C° to spread out on the surface uniformly. After that, the PVDF layer is carefully aligned under a magnification lenses and smoothly attached and stretched on the bottom of U- Channel surface. A compression block is placed carefully to press the PVDF layer to the silicon layer to make sure for uniform attaching of both layers together. This step is shown in Figure 4.21.

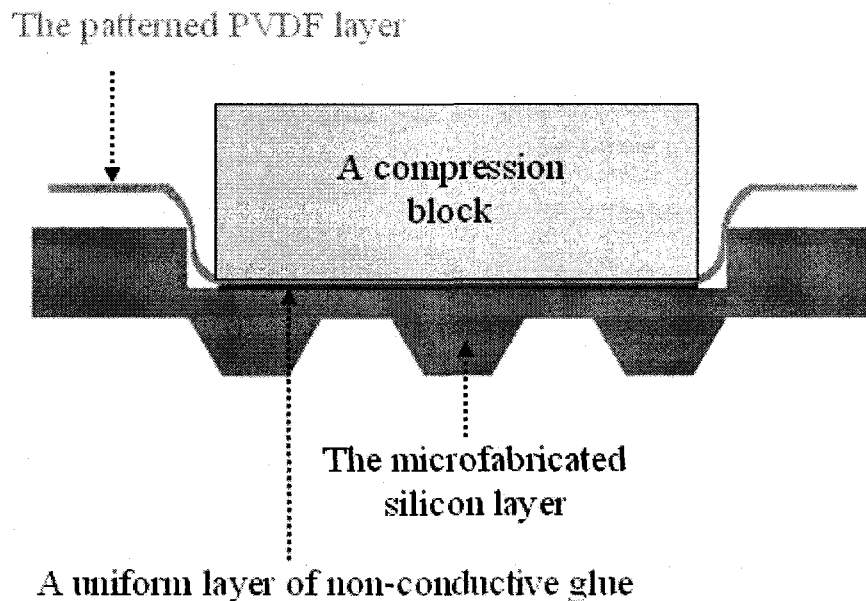


**Figure 4.21 – First step of the sensor assembly**

The compression block is to stay for 24 hours compressing the two layers at the room temperature. After the 24 hours, the same procedure of assembling is repeated to attach

the side parts of the PVDF layer on the surface of the silicon supports. Taking into consideration keeping the compression block at the middle, this step is shown in Figure 4.22.

After keeping the whole compression blocks pressing both layers together for 24 hours as shown in Figure 4.22, the output wires are prepared.

Each output of the sensor is prepared by soldering a thin copper wire to a copper electrode. The copper electrodes are to be connected to the metalized areas of the PVDF layer, and the copper wires to be connected to the measurement instruments (Computer, Oscilloscope, etc). One of the prepared outputs is shown in Figure 4.23.

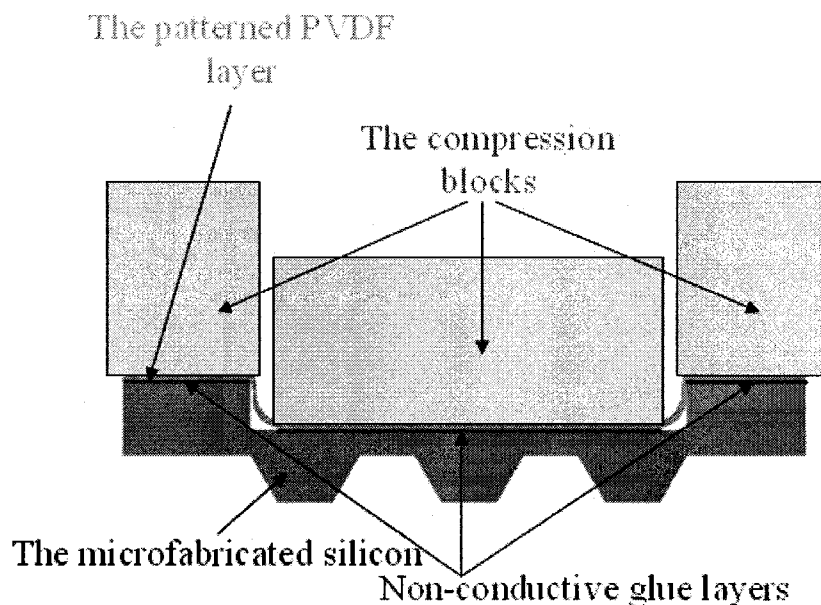


**Figure 4.22 – Second step of the sensor assembly**

After preparing the ten output electrodes of the sensor and working under magnification lenses; each electrode is carefully aligned and connected by a conductive epoxy to the proper metalized area on the PVDF. Connections of the electrodes to the metalized areas of the PVDF are shown in Figure 4.24.

The next step is to attach the whole structure to the supporting Plexiglas layer. A piece of Plexiglas is prepared with relevant dimensions and assembled to the sensor. This step is shown in Figure 4.25, and the complete assembly of the sensor is shown in Figure 4.26.

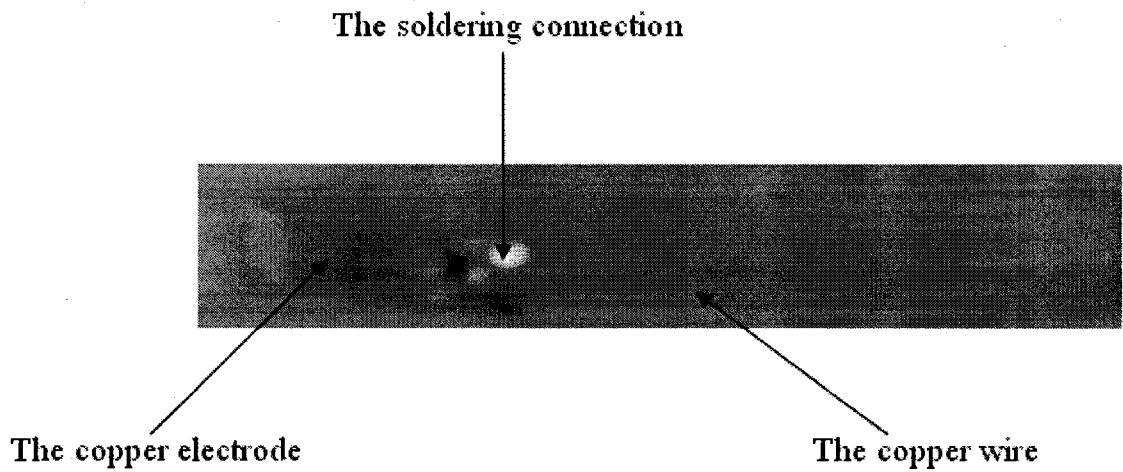


Figure 4.23 – Details of the output terminal preparations

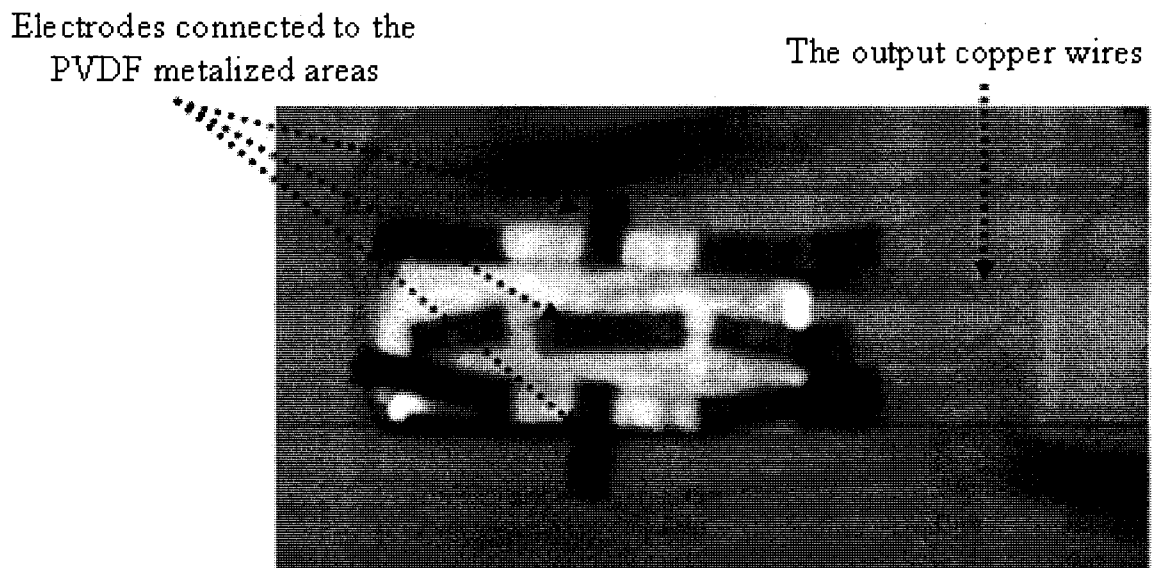
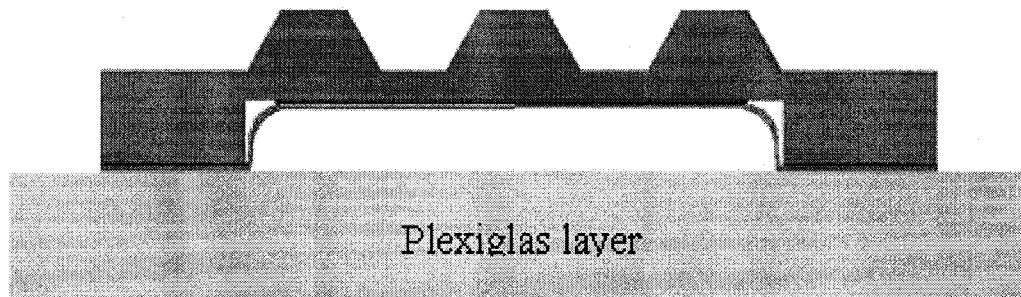
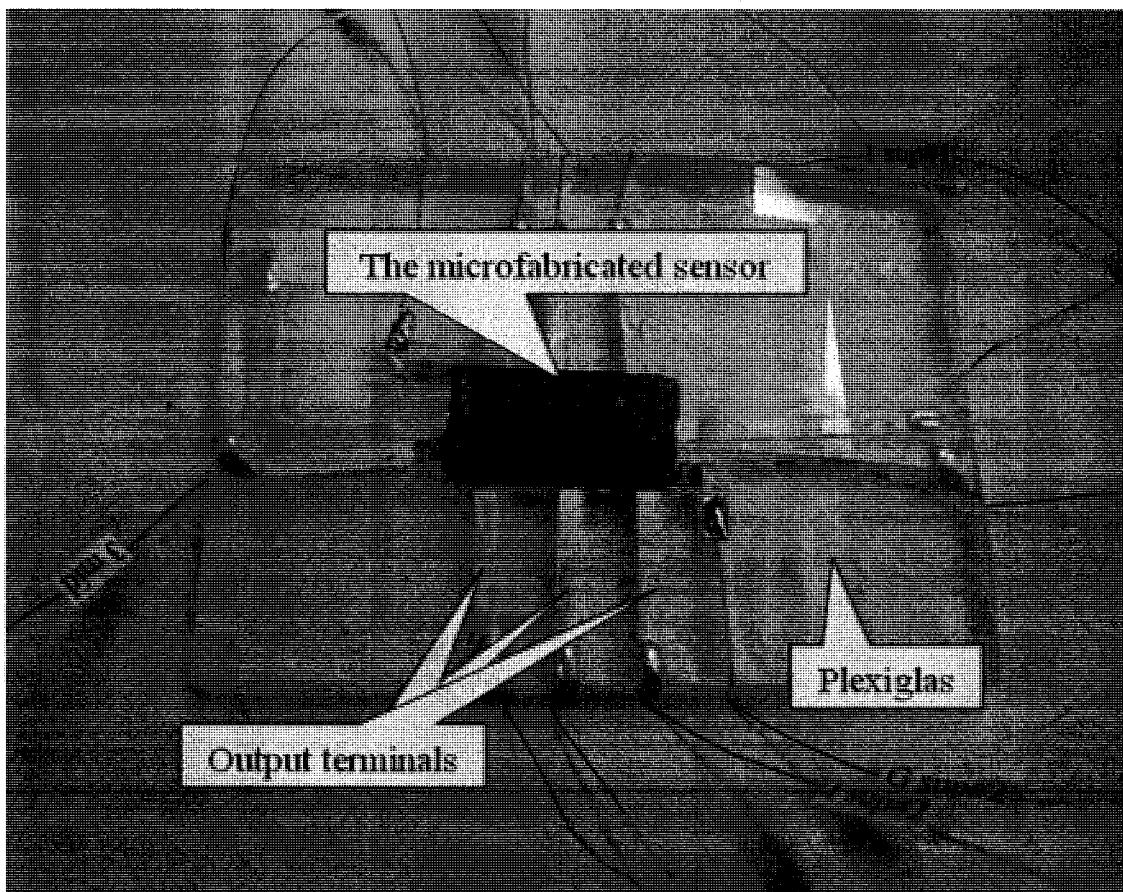


Figure 4.24 – Bottom view of the assembled patterned PVDF and microfabricated silicon



**Figure 4.25 – Side view of the complete sensor assembly**



**Figure 4.26 – Top view of the microfabricated sensor**

After assembling of the sensor, the output wires will be connected to conditioning circuit and finally to a computer for analysis. Experimental tests and characterization of the presented sensor are discussed on the next chapter in details.

#### **4.4 Summary**

In this chapter, microfabrications of the different sensor layers and the layers assembly are performed. Procedure of the silicon bulk etching on both sides are reported and explained. The convex corners which associated with the teeth shapes are compensated; the method which used and the light field mask are addressed. Microfabrications of the PVDF sensing elements by patterning aluminum coating using MEMS technology are discussed. Finally, the different layers assembly procedure and the output terminals preparations and integrations with the different sensing elements are addressed.

## **Chapter 5 – Experimental Results and Characterizations**

After fabrications and assembling of the tactile sensor, the output leads of the sensor are connected to a computer for analysis. Connections of the output ports to the computer are done via data acquisition card (DAQ) and supporting electronic system. Using the data acquisition card, the signals are amplified, filtered, digitized and finally processed by a computer.

Installed LabVIEW software is used for interface and graphical display of the output signals on the PVDF sensing elements of the sensor.

The sensor is tested for dynamic force inputs applied by the load cell to the object; the experimental setup for the sensor characterization is discussed with the following sections.

### **5.1 Experimental Set-up**

The schematic diagram of the experimental measurement setup, developed to analyze the performance of the sensor, is shown in Figure 5.1.

The sensor is positioned under a cylindrical probe, which is driven by a vibration unit (Ling dynamic model V203), and used to apply a sinusoidal force at frequency 5Hz. The vibration unit is activated by a signal generator (Agilent 33220A).

The magnitude of the applied force is determined by a force transducer (KISTLER, Type 9712B50), which inserted between the probe and the vibration unit and connected to a charge amplifier for amplifications, and then connected to a computer via data acquisition card and connectors to monitor the applied load.

Similarly, the PVDF sensing elements are connected via wires to the charge amplifiers, and then the output of the charge amplifiers are connected to the data acquisition card via some connectors to be measured on the computer. The 60 Hz line noise was filtered out using the Labview built-in Butterworth low pass filter.

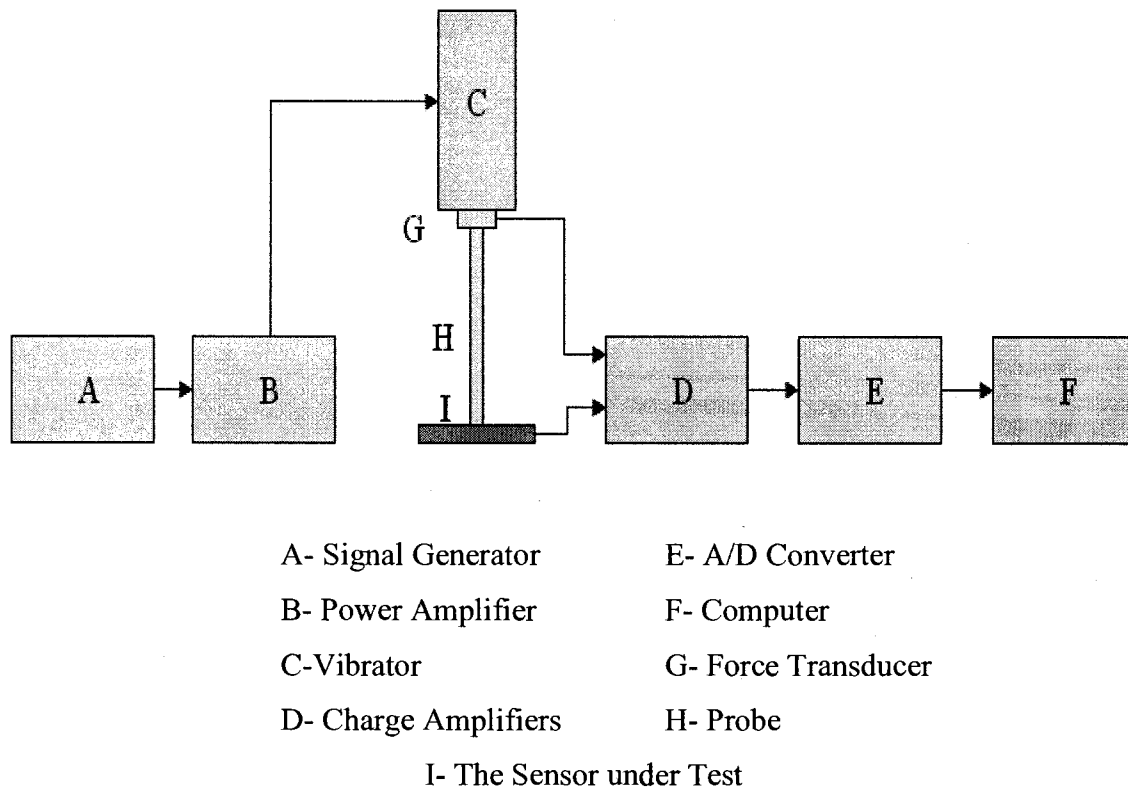


**Figure 5.1 - The experimental Set-up**

A list of all equipments and their specifications, used for running the experiments, are provided in Appendix A2.

The complete experimental set up with all the electronic components and the display unit is shown in the Figure 5.2. The equivalent electrical circuit of the PVDF film, and its connected experimental setup, is described in the Appendix A3.

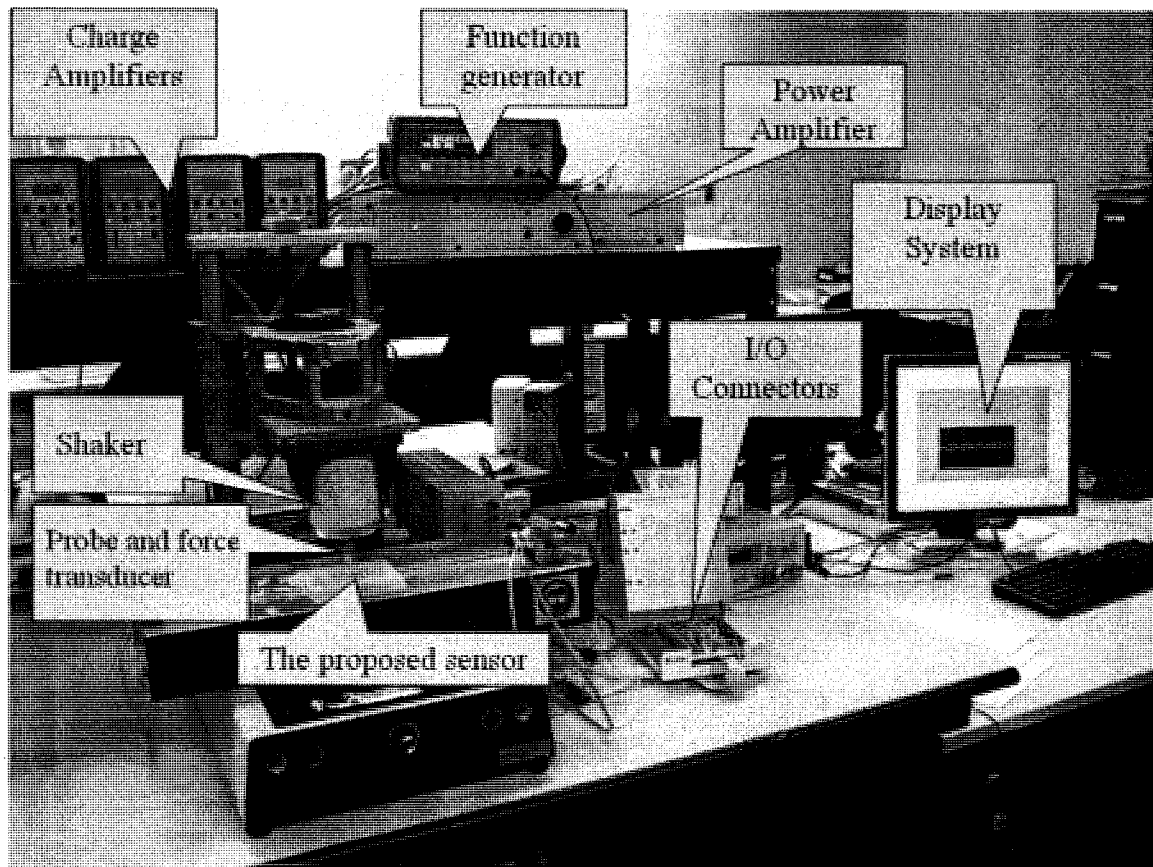


**Figure 5.2 - Photograph of the complete setup**

## **5.2 Experimental Tests**

After the proper connections of the sensor outputs, turning-on the set-up equipments, and running the graphical display software on the computer; different experiments are done and the results are recorded.

Analogous to the finite elements analysis and the simulations which carried out on the section 3.4; the experimental tests are carried with different loading conditions to verify the sensor functions. In the following sections the experimental procedures and the results are discussed.

### 5.2.1 Sensor Calibrations

Calibration is defined as the process of quantitatively defining the system response to a known and controlled signal inputs. A known force was applied to the sensor using the shaker and the outputs voltages from the sensor are measured.

The applied force is sinusoidal load of 5 Hz frequency. The loads are applied on the center point of the sensor, and the sensing elements outputs are recorded. The probe of 2 mm diameter and the proposed sensor under test is shown in Figure 5.3.

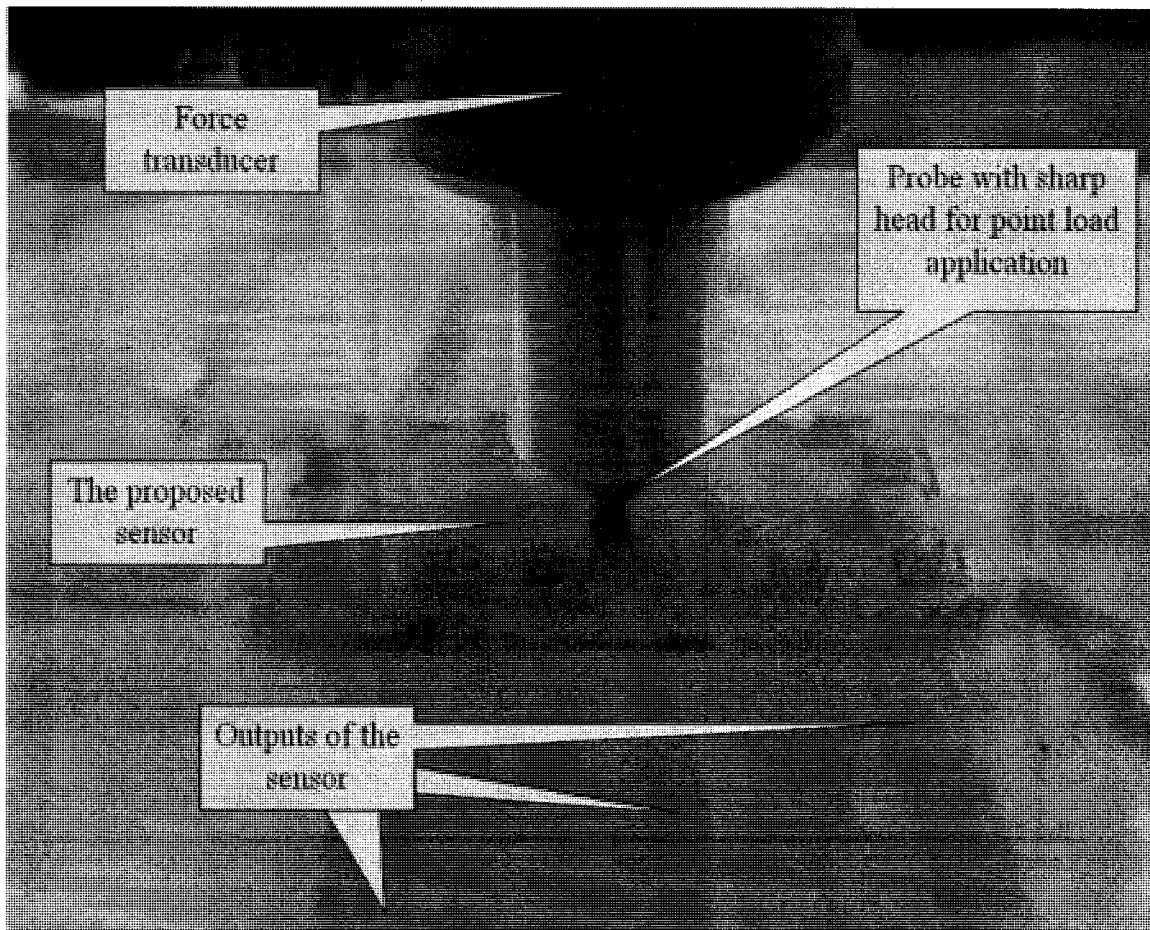


**Figure 5.3 - The probe while applying a concentric load at the center of the sensor**

The peak to peak applied force is monitored using the force transducer as the reference load cell. And the output peak to peak voltages from the sensing elements at supports and middle PVDF and in the middle are recorded. Corresponding to the sensing elements notations which shown in Figure 3.27, the considered sensing elements are Middle2, Support12, and Support22. These magnitudes of the peak to peak outputs with respect to the peak to peak input forces at the center of the sensor are shown in Figure 5.4.

Due to the experimental hardware limitations; such as low sensitivity of the force transducer, lack of the shaker to supply low magnitude forces, and because the high noise/signal ratio at low force inputs; smaller range of loading is applied and verified experimentally.

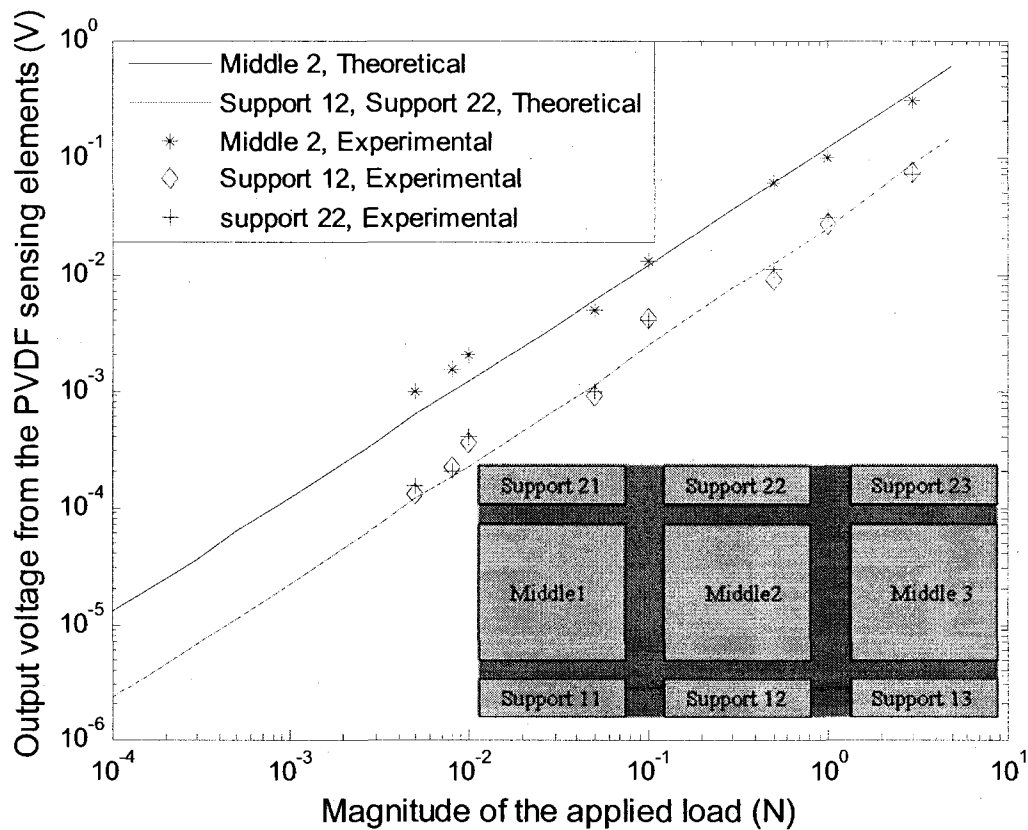


Figure 5.4 - The calibration curves

As shown on Figure 5.4, the experimental results are compared with the Finite element results obtained in Section 3.4.1.

It is clearly shown that the experimental results are analogous to the theoretical ones and it's fairly linear with respect to the applied load magnitude.

## **5.2.2 Position Detection of the Applied Concentric Load**

In this experiment, concentric load is applied via a probe of 2 mm diameter at different point, and the output voltage is recorded.

Similar to simulations, the load is applied at the center of the sensor in both horizontal and vertical (X-Y) directions. The following two sections describe these two experiments.

### **5.2.2.1 Concentric Load Moves Along Y – Direction**

The applied peak to peak concentric load of one Newtown is applied in different point along Y- Direction. The output voltages on the sensing elements Middle2, Support12, and Support22 versus the applied load location are shown Figure 5.5. (See also Figure 3.20 and Figure 3.24, which describes the sensing elements notations and the applied point locations respectively).

The results along with Finite element results are shown in Figure 5.5. It can be seen that the experimental results are closely matching the theoretical results.

The error is due to positioning of the probe on the intended point on the sensor. In addition, the experimental loading is dynamic while the theoretical analysis is based on static load

As it is shown in Figure 5.6, the difference between the output voltages on each pair of sensing elements at supports is linear with respect to location of the applied concentric load. Using this linear relation, the location of applied load in Y- Direction can be detected.

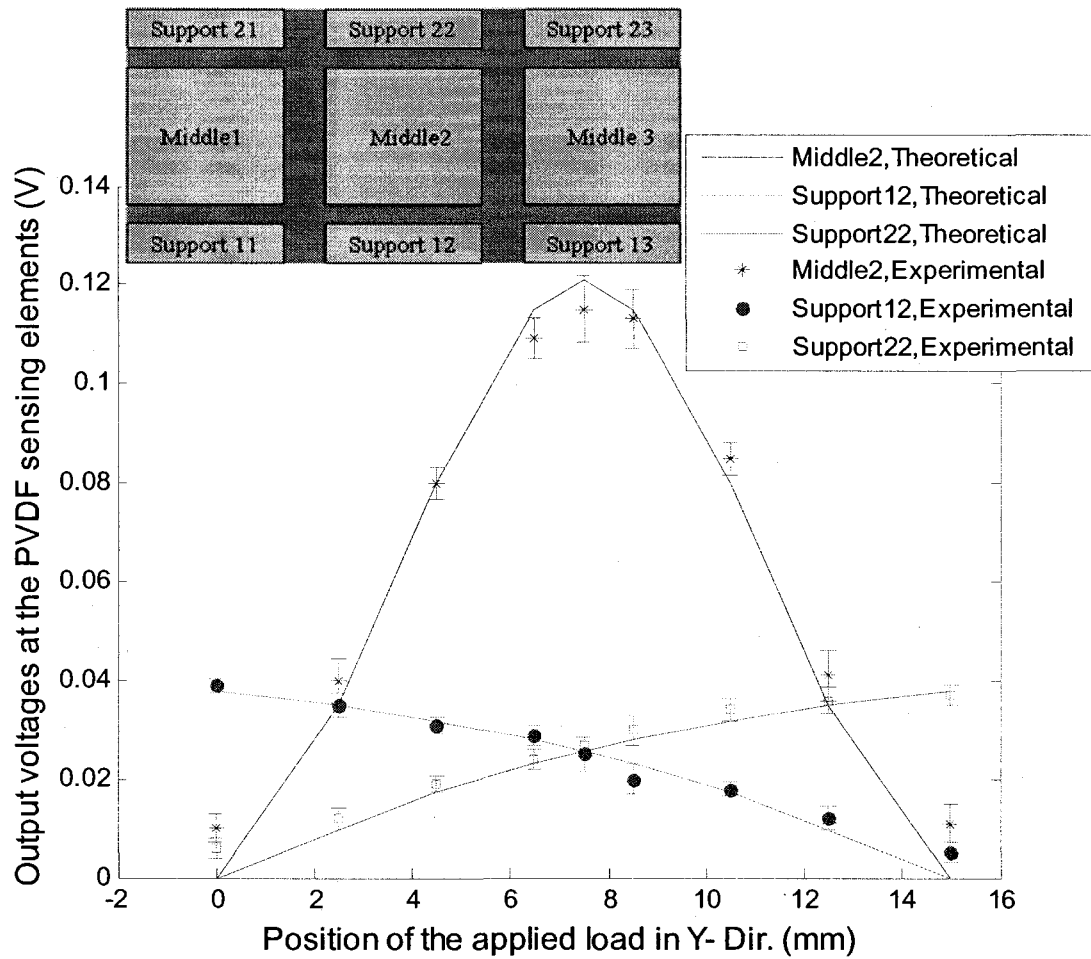
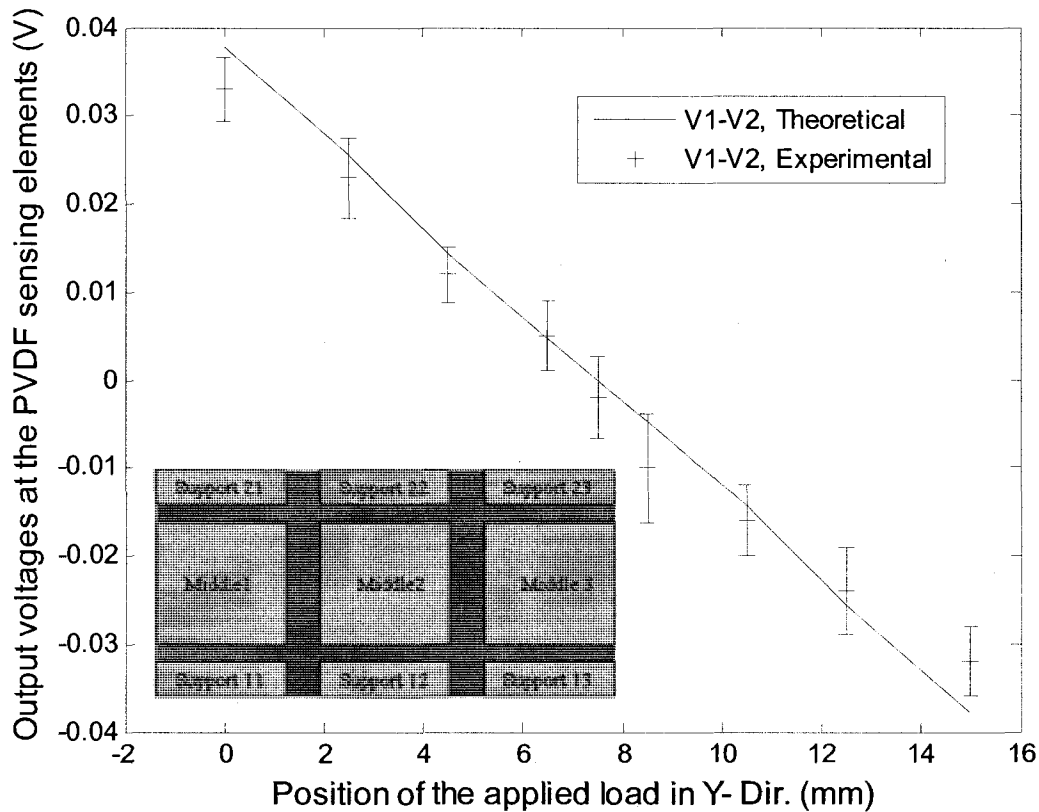


Figure 5.5 - Output voltages at the sensing elements when a concentric load is applied along Y- Direction

### 5.2.2.2 Load Moves Along the X-Direction

In this section, the experimental procedures were the same as the Section 5.2.2.1. But the applied peak to peak concentric load of one Newtown magnitude is applied in different point along X- Direction instead of Y- Direction.



**Figure 5.6 - The difference between output voltages at the sensing element Support12 (V1) and the sensing element Support22 (V2)**

Five points are chosen to be the location of the applied load; each point is the center of the top surface of each tooth in the middle array of teeth. The same notation's for the sensing elements which shown in Figure 3.20 are used. And the working line of the load points along X-axis can be shown in Figure 3.28.

Algebraic summations of the output voltages on each pair of sensing elements at supports versus the X- location of the applied load is shown in Figure 5.7; experimental and theoretical results are compared.

Experimental and theoretical results of output voltages at the middle sensing elements versus the X- location of the applied load are shown and compared in Figure 5.8.

As shown in Figure 5.7 and Figure 5.8; experimental results are similar to the theoretical ones with rational variations. Variations between theoretical and experimental results are due factors, such as the imprecise location of the applied load, and error due to reading of the peak to peak magnitude of the input force, and the cables noise.

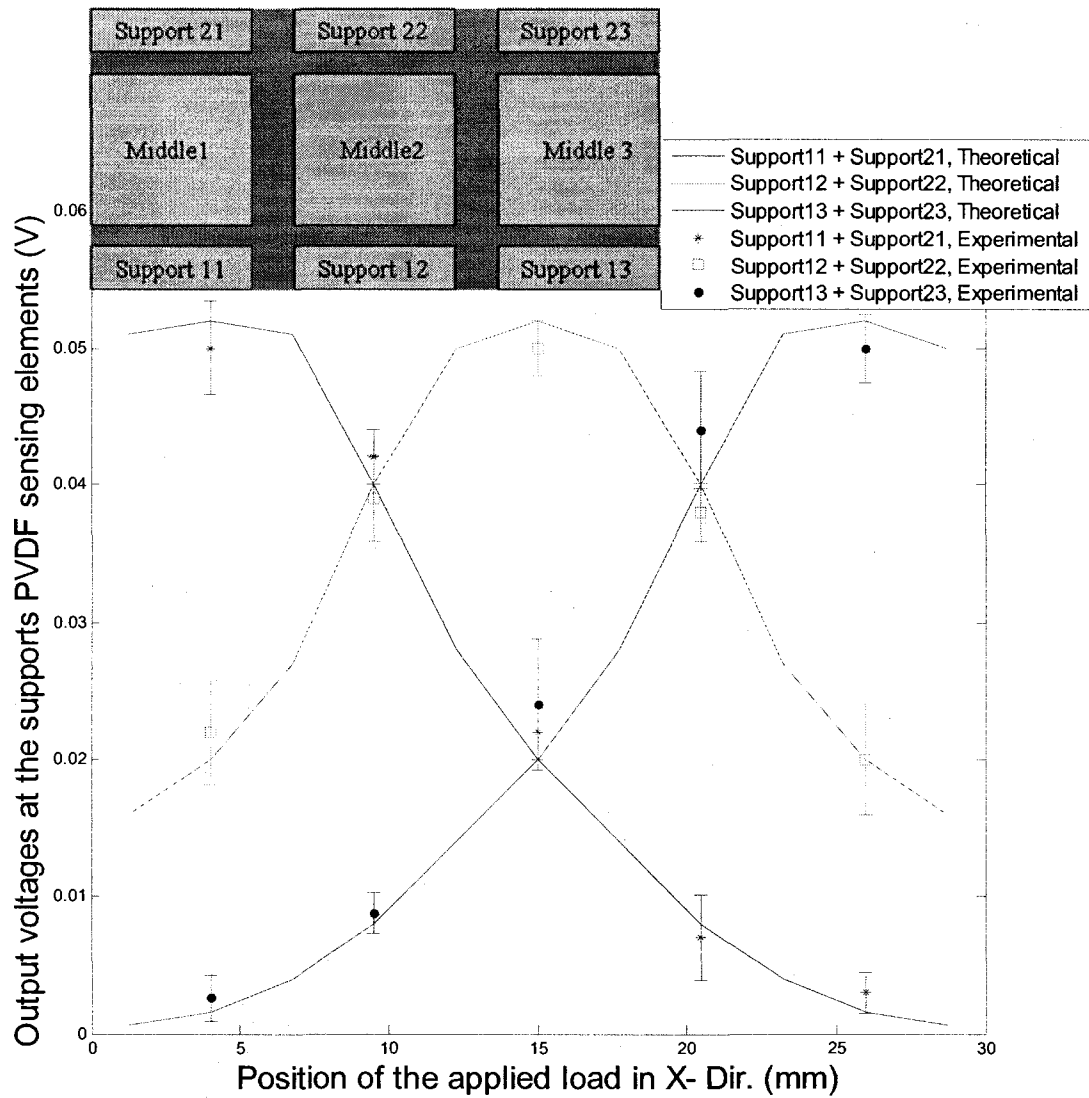
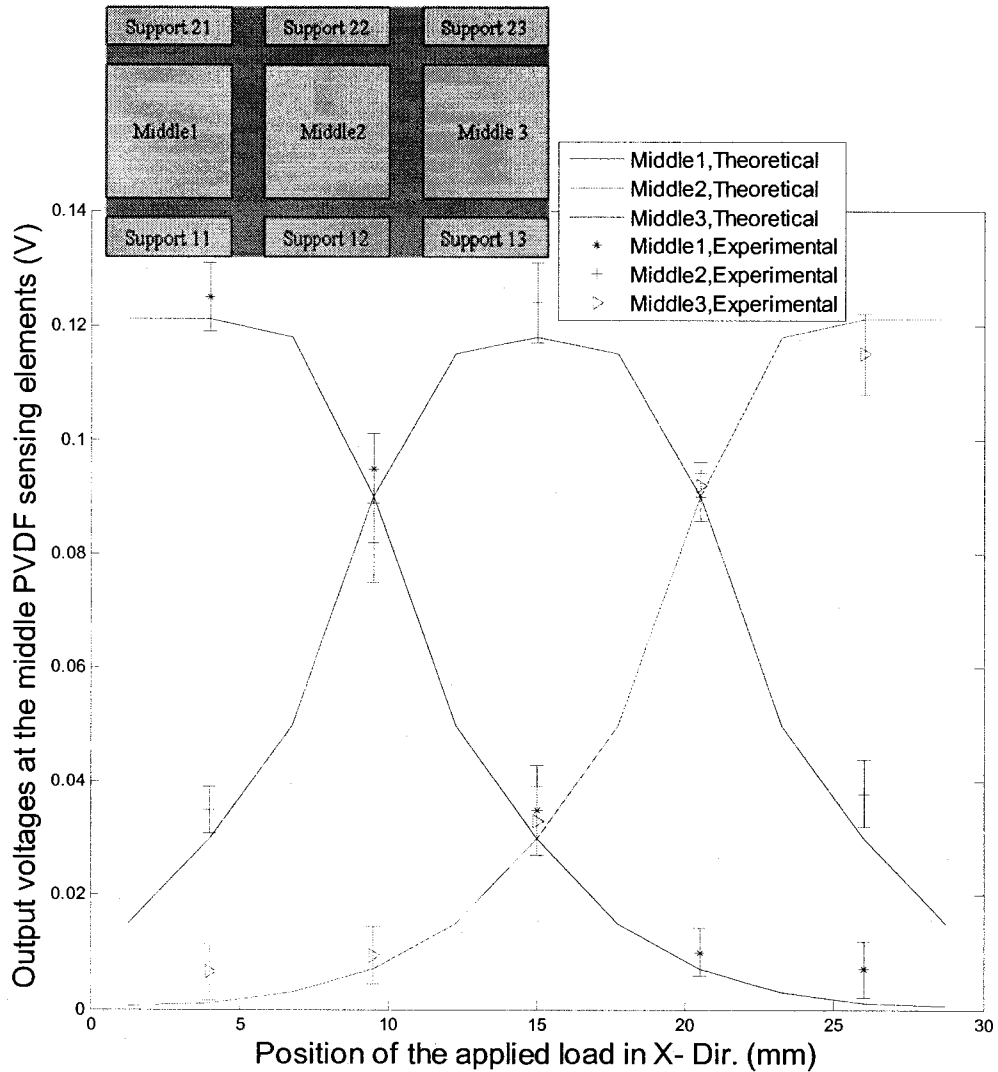


Figure 5.7 - Output voltages at the supports sensing elements versus X- location of the load



**Figure 5.8 - Output voltages at the middle sensing elements versus X- location of the load**

### 5.2.3 A Distributed Load Applied on the Contact Object

As previously mentioned, one of the main functions and features of the proposed sensor is its ability to measure compliance of contacting objects. These objects are grasped and compressed with the MIS tool. Thus, for this test a distributed load is considered, and soft objects are assumed to be isotropic with different Young's modulus.

Different elastomers with given stress-strain relations are examined, and the sensing elements outputs of the middle PVDF films are monitored. The stress-strain relations of the different elastomers are nonlinear for the high stress applications. However, those relations are fairly linear for low stresses applications which used in experiments.

For each object; the compressive load is calculated and the strain is picked from the given stress-strain relation, and then the object's modulus of elasticity is calculated. Six elastomers with different modulus of elasticity are used; the calculated moduli of elasticity for the different six elastomers are as the following;  $E_{\text{Sample\#1}} = 0.1 \text{ MPa}$ ,  $E_{\text{Sample\#2}} = 0.76 \text{ MPa}$ ,  $E_{\text{Sample\#3}} = 3 \text{ MPa}$ ,  $E_{\text{Sample\#4}} = 7.4 \text{ MPa}$ ,  $E_{\text{Sample\#5}} = 11.15 \text{ MPa}$ , and  $E_{\text{Sample\#6}} = 60 \text{ MPa}$ . The samples are shown in Figure 5.9. For each object the output voltages at the middle PVDF sensing elements are reported.

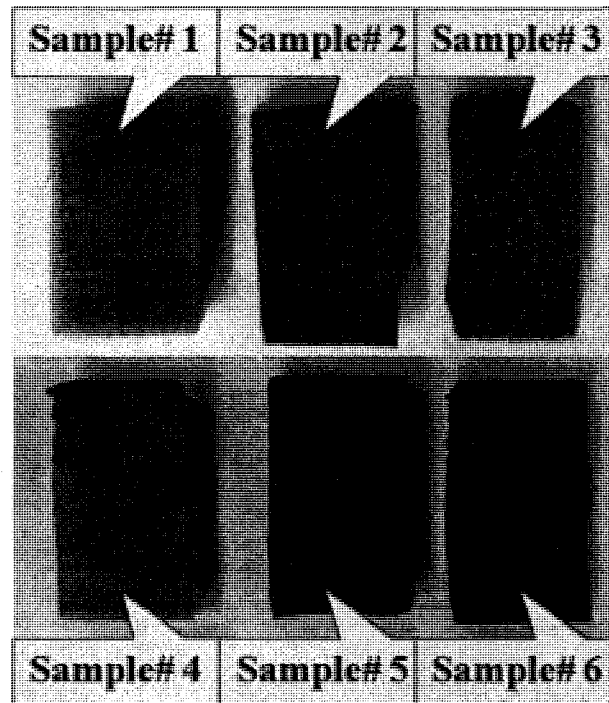


**Figure 5.9 - Elastomers with different stiffnesses which used on the experiment**

At each contacting elastomer, a distributed load of 5 N is applied on the top of the elastomer and then output voltages at sensing elements are recorded. The distributed load action on the top of the contacting elastomer is shown in Figure 5.10.

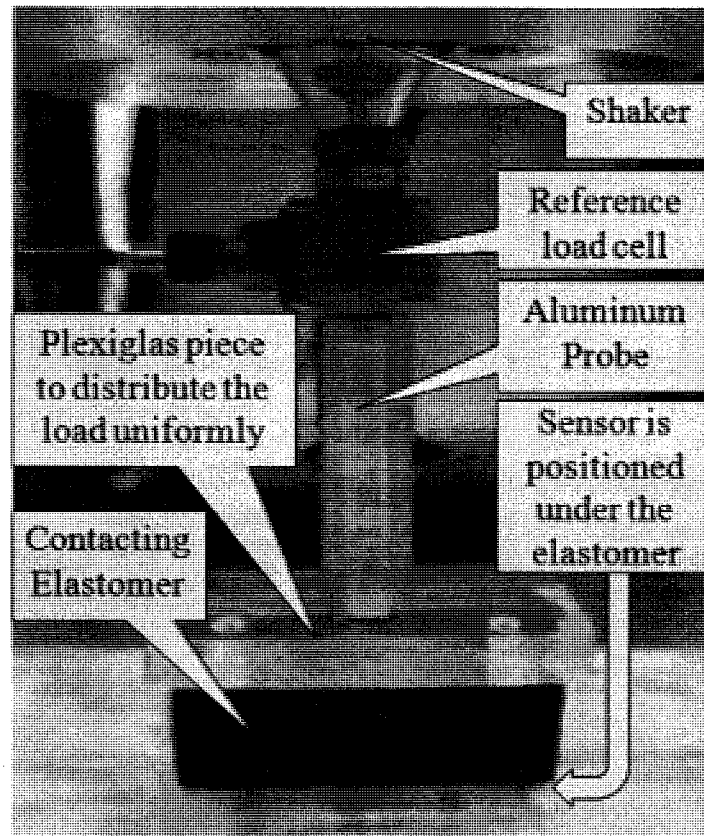


**Figure 5.10 - A uniform distributed load applied on the top of contacting tissue (elastomer)**

Output voltages at the middle PVDF sensing elements versus a different modulus of elasticity of the contacting tissues (elastomers) for 5 N distributed uniform load is shown in the Figure 5.11.

On the same way of theoretical analysis; a different grasping forces are considered in order to check the sensor sensitivity. At each grasping force, the modulus of elasticity of each object is recalculated. And the output voltages on the sensing elements at the

different contacting objects are recorded. The relation between the output voltage and the modulus of elasticity of the contacting tissue/ object at different grasping forces are shown in Figure 5.12.

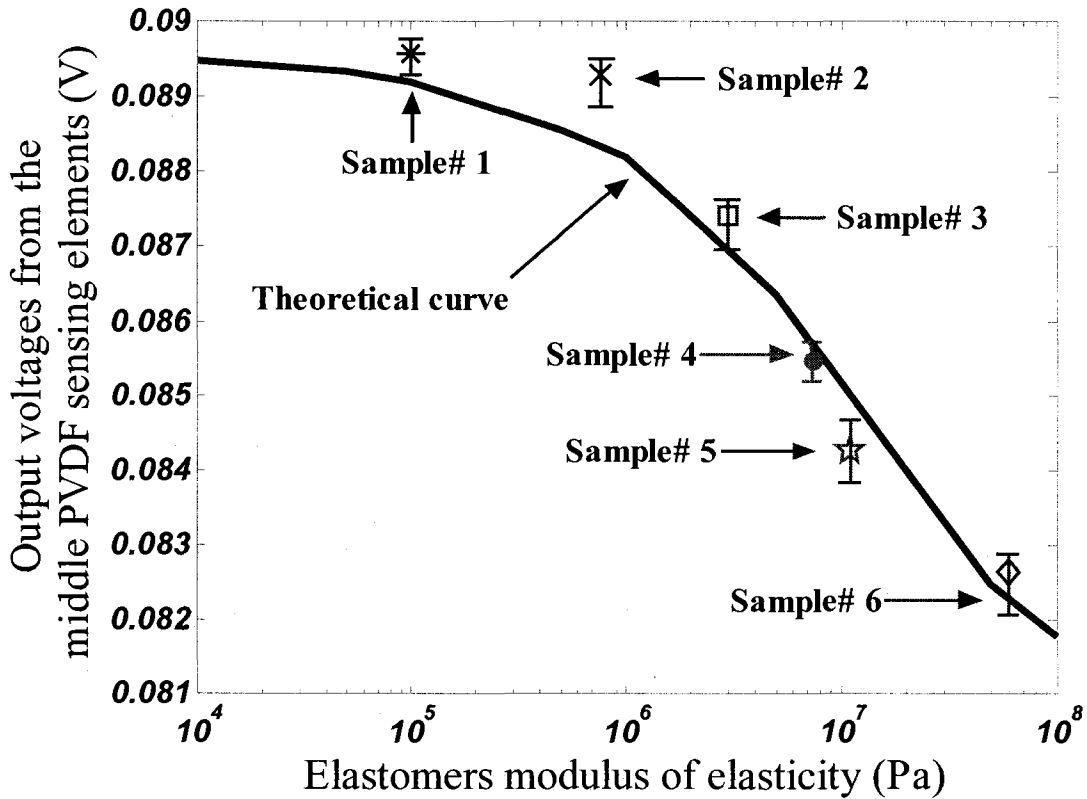


**Figure 5.11 - Output voltages at the middle PVDF sensing elements versus different tissues (elastomers) stiffnesses at 5 N grasping loads**

As it can be seen from Figure 5.11 and Figure 5.12; experimental and theoretical results are quite comparable for various applied forces. But they are matching with high grasping forces more than the low grasping forces.

As discussed on the previous sections, many factors affect the experimental results and cause discrepancy with the theoretical results. In addition, in the theoretical analysis we

considered pure linear elastic objects in contact with the proposed sensor. However, in the experimental analysis the elastomers exhibit some non-linearities.

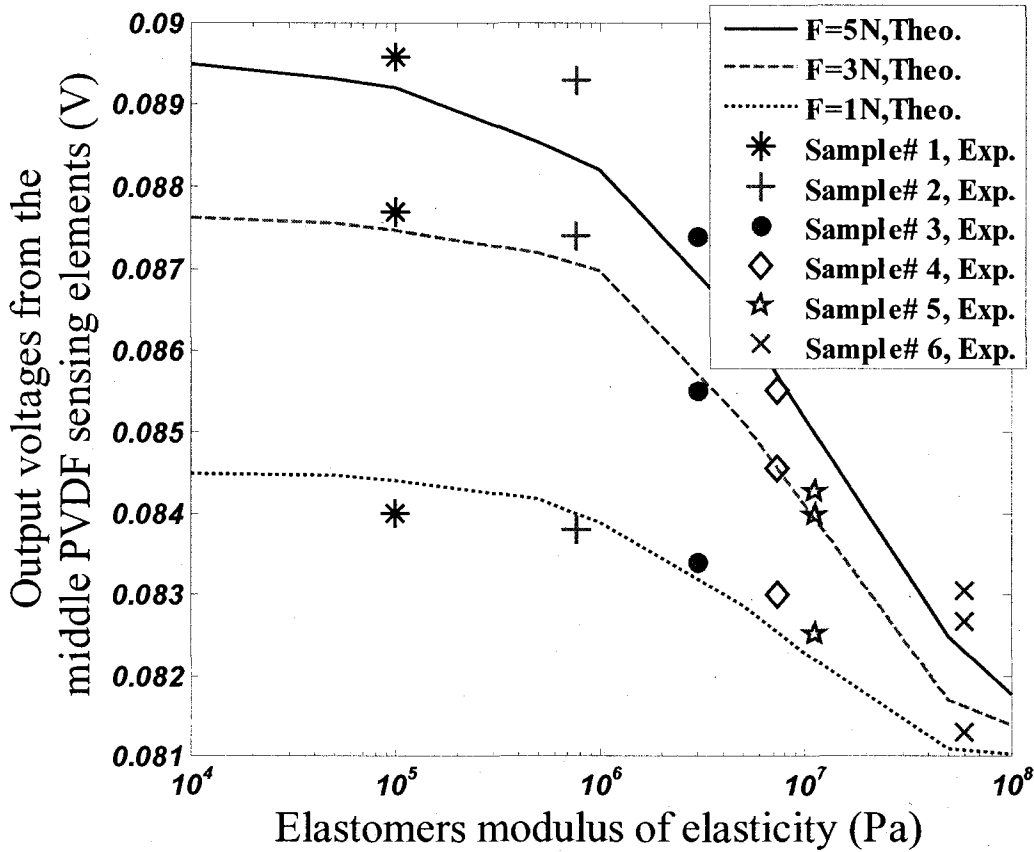


**Figure 5.12 - Output voltages at the middle PVDF sensing elements versus a different tissues (elastomers) stiffnesses at different grasping loads**

For best contacting tissues characterizations; a reasonable distributed grasping forces have to be applied on the contacting tissue. That is analogous to the human palpations by fingers; where humans apply enough sensible force to examine the touched object.

### **5.3 Summary**

In this chapter, the test setup is proposed, and the associated components are listed. Moreover, many of experimentations are carried to evaluate the sensor performance. At first, experimental calibration curves of the proposed sensor are conducted and compared to the Finite element results. Using experimental and theoretical analysis, it was shown that the sensor can measure the magnitude and the position of the applied load in the two directions (X and Y). Finally, the sensor performance in relation to objects softness detection is evaluated; different contacting objects (elastomers) with known modulus of elasticity are applied to the sensor surface, and the experimental and theoretical results are compared.

## **Chapter 6 – Discussion, Conclusions, and Future Work**

The major objective of the presented research is to design and microfabricate a tactile sensor which could be integrated with Minimal Invasive Surgery (MIS) tools and feedback the important tactile signals during surgery operations. To achieve cost effectiveness, the sensor consists of only piezoelectric material and a layer of silicon and is therefore easy to assemble and cheap to manufacture. The sensor is designed to satisfy the research objectives based on compression and tension forces transmitted to the sensing elements. The width and length of the sensor are chosen to justify theoretical and experimental results and its thickness is analyzed to cover the range of loading which include grasping forces as well as the low mechanical forces which could be comparable to the blood vessel pulsating.

The first section of this chapter discusses the sensor design and specification which was presented in Chapter 2, discussing the modeling, analysis and simulations of the proposed sensor as discussed in Chapter 3, discussing the sensor layers microfabrications and its assembling which explained in Chapter 4, and finally discussing the experimental setup and the experimental characterizations which detailed in Chapter 5. The summary is presented in the second section of this chapter together with conclusions. The last section of this chapter is introducing the possible expansions of the sensor and future work.

## 6.1 Discussion

This section presents a discussion on sensor design, modeling, microfabrication, and experimentation.

1. The designed sensor has a corrugated shape on both length and width, and contains an array of teeth for better grasping abilities. The teeth shapes are required for gentle loading on the tissues while grasping, and for appropriate handling ability of soft slippery tissues while grasping, lifting, and twisting. When grasping soft slippery tissues, high grasping forces are forbidden although there are instances in which twisting while grasping could be required, so it is preferable that both sides of the sensor are corrugated.
2. The proposed sensor comprises of silicon and PVDF. Silicon is a good choice for this application because it is simple to manufacture large batches using MEMS with resulting low costs. It is also biocompatible with internal organs and it is a very good material when under compression in which even the thinnest silicon layer is deformable with good strength. PVDF is a known sensing element in the tactile sensing field because of its cheapness compared to other piezoelectric materials and the ease of attaching electrodes for collecting charges.
3. The designed sensor will be integrated with one jaw of the endoscopic grasper. The second jaw is integrated with an additional etched silicon layer having the opposite shape of the teeth arrangement of the tactile sensor as shown in Figure 2.6. That helps for better grasping and gentle pressure distribution on the grasped tissues/object.

4. The prototype sensor is of 30 mm length and 15 mm width; these dimensions are comparable to the experimental set up ability.
5. The thickness of the silicon layer on the sensor is analyzed to cover the range of grasping forces as well as to be sensitive to the small mechanical forces which could be comparable to the pulse in blood vessels. After etching teeth and supports features on the silicon layer, the thickness of the base plate is 100  $\mu\text{m}$ .
6. The proposed sensor could have different dimensions other than the microfabricated prototype provided that they are compatible with different endoscope tools and sizes. For any combination of sensor dimensions, and to cover the same deformations sensitivity, a parametric study of the design is undertaken. By selecting dimensions which are restricted by the endoscope tool itself, the other dimensions can be picked up from the curve, shown in Figure 3.8, to have the same loading range as that of the tested prototype.
7. Geometrical analysis of the corrugated shape of the silicon layer is carried out. As shown in Figures 3.9 to 3.12, the best deformations occurred with the simple plate case. But since the designed sensor has to be integrated with a grasper where the teeth-shape is required, the simple plate is excluded. The case of irregular teeth arrangements shows better deformations than the regular arrangements and hence is chosen because of its teeth property and deformability.
8. Locations and distributions of the sensing elements on the PVDF layers are studied. A constant point load was applied on the center of the sensor and the output voltage on each PVDF layer is studied. The induced voltage profiles at each layer are distributed on the center region covering almost one third of each

PVDF layer area as shown in Figure 3.13 and 3.14. These are the useful regions of PVDF layers from which used to collect output voltages. They are located at the center area and considered as being one combination of the sensing elements. Because that combination covers almost one-third of the overall area, two other combinations of sensing elements are distributed on the PVDF layers to cover the whole area as shown in Figure 3.15.

9. When studying orientations of the PVDF layers, two possible cases are considered. The first case is the drawn direction ( $d_{31}$ ) of PVDF films oriented parallel to the sensor width (Y-direction). The second case is when the drawn direction of the PVDF layers is oriented parallel with the length of the sensor (X-direction). The results shown in Figures 3.13, 3.14, 3.16, and 3.17 indicates that, for higher sensitivity and less crosstalk, the  $d_{31}$  direction of the PVDF layer has to be oriented parallel to the sensor width (Y-direction). This is because the voltage in this case is more uniform and bounded on the force action region. In addition, the output voltage in that case is higher, consequent by higher sensitivity of the designed sensor. For that reasons, it is arranged that the drawn direction and width of the sensor are aligned together to be parallel with each other.
10. Homogenous grasped organs is acting as a uniform disturbed load in the grasper jaw while grasping, but existence of any hidden features inside grasped organ is acting as concentric loads and causing a disturbance on that uniform disturbed load. As shown in Figure 3.18, 3.19, embedded lumps or arteries are acting as point loads, and blood vessel is acting as both as a function of time, as shown in Figure 3.20.

11. The silicon layer is microfabricated using TMAH anisotropic etching to have teeth shapes on the top, and two supports at the bottom. The microfabricated teeth is of trapezoidal shapes with  $\{111\}$  planes on the side walls. The convex corners are compensated. As shown in Figure 4.14 and 4.15, the teeth edges are fairly straights and the convex corners are reasonably compensated.
12. All of the PVDF sensing elements are patterned on one PVDF sample using the conventional MEMS procedures with the supports of a glass slide. The glass slide is used to support the thin flexible PVDF film while the photolithography process and the aluminum etching. The sensing elements are microfabricated by patterning one of the metalized surfaces of the PVDF film, and other metalized surface is kept as a common electrode.
13. As shown in Figure 5.4, simulation and experimental results shows a good linearity between the output voltage at the PVDF sensing element and magnitudes of the applied load. The total grasping load could be measured by summing the output voltages of the supports sensing elements.
14. As shown in Figure 5.4, the middle PVDF layer is the most sensitive and its output voltage is the highest. It responds to low magnitude mechanical forces and can detect and sense the pulse in blood vessels while grasping internal organs.
15. In order to detect the precise location of concentric loads (embedded lumps) during surgery, a constant concentric load is applied on different locations in the XY plane. As shown in Figures 5.5, 5.7, and 5.8; simulations and experimental results are presented. By comparing the output voltages from the different sensing elements; location of the applied load in XY plane is detected. Any point on the

sensor surface is active and responsible for transferring a load to the corresponding sensing elements.

16. Results as shown in Figure 5.11, the output voltage at the middle PVDF sensing elements decreases when grasping a harder object/ tissue. The output voltages from middle PVDF sensing elements while grasping different objects softnesses are reasonably varied, and the grasped organ softness could be estimated.
17. As shown in Figure 5.12; with higher grasping forces the sensor has better ability to measure the snatched object/ tissue softness. However, at the lower grasping forces the sensor sensitivity to the softness estimations is less. This, however, is analogous to when the surgeon is palpating by his/her fingers, during the traditional open surgeries, which requires enough compression force to distinguish between the different object stiffness and any abnormality inside.
18. Due to hardware limitations such as the low sensitivity of the force transducer, and the high signal-to-noise ratio at low inputs, only a small range of loads could be applied and verified experimentally.
19. The theoretical analysis was based on a constant static load, and the experimental results were based on a low frequency sinusoidal load. Although these were compared, the peak-to-peak of the sinusoidal low frequency force response is compared to the static load response and the resulting voltages on sensing elements are compared in both cases. That's could be one of the reason which making a variations between simulation and experimental results.
20. Comparisons between theoretical and experimental results clearly indicates that experimental results are analogous to the theoretical and is a fair match as shown

in Figures 5.4-5.8, and 5.11-5.12. Variations between these results are due many factors in addition to comparing static loads in simulation with the dynamic loading in experiments. These factors include the imprecise location of the applied load and the inaccurate peak-to-peak magnitude of the input force. Also cable noise and the stand table vibrations were factors which, when improved, would yield more accurate experimental results approaching the theoretical ideally.

## **6.2 Conclusions**

1. The proposed sensor is of a tooth-like shape which is necessary when grasping and handling soft slippery tissues.
2. The proposed sensor is simple in structure and is relatively cheap to produce.
3. The sensor is designed based on silicon and PVDF both of which are biocompatible with internal organs and compatible with MEMS technology.
4. The proposed sensor shows good linearity with the magnitude of applied loads. By calibrating the sensor outputs, grasping loads during surgery can be calculated.
5. The proposed sensor is able to detect low magnitude mechanical forces, for around 1mN, which could be comparable to the pulsation in blood vessels. By grasping internal organs, any blood vessels inside can be sensed.
6. The proposed sensor is able to find the location of any concentric loads on the XY plane. By detection of the concentric loads and its location, any embedded lumps inside the grasped organ can be distinguished.

7. The proposed sensor can estimate the contacting object/ tissue softness. By calibrating the sensor outputs, contacting objects softness during surgery can be calculated.
8. The entire area of the proposed sensor surface is active. There are no null points in this design and any applied load at any location can be detected and measured.
9. The proposed sensor is simple, microfabricated using MEMS technology, could be manufactured in batches with low costs, and the possibly to be designed as a disposal part of the MIS tools.

### **6.3 Future work**

With the advent of each prototype, a great deal is learned and more improvement can be made. This thesis presented the design concept of a microfabricated prototype sensor. Theoretical and experimental tests were discussed and the results were satisfactory, although it is clear that a number of improvements can still be made. The following subsection outlines suggested improvements and addressing the possible future work.

1. A more accurate and reliable experimental setup is required that addresses the following:
  - a) Install a force transducer having better range and sensitivity.
  - b) Use connection cables with low-noise and low-capacitance properties.
  - c) Affix a low-pass filter with good performance to eliminate the noise signal.

- d) Ensure that the shaker stand has precise three-dimensional coordinates to distinguish the exact location of the applied load on the sensor surface.
  - e) Provide a manufactured object/ tissue samples with a known and accurate modulus of elasticity.
  - f) Interface the present sensor with graphical software to display the contacting forces and tissue softness or with a haptic interface to feel contacting forces and discriminate the tissue softness.
2. Future work can be extended to different directions. More work is required on the miniaturization aspect, fabrication methodology, and packaging of the sensor. Some possible development features are discussed in the following points:
- a) Proper packaging and protection from the environment is required for more effective functioning of the sensor.
  - b) Microfabrication of the sensor on electronic chip in order to eliminate electrode and wiring connections to the PVDF sensing elements and thereby obtain high-precision measurements.
  - c) Direct deposit of the PVDF on the silicon layer instead of PVDF film patterning and gluing, and also depositing aluminum nanoparticles on the PVDF layers to facilitate charge collecting to make it a much more precise and integrated sensor.
3. One of the aspects of the design is to consider the effect of leakage on the sensor from fluids inside the body. Such leakage on the PVDF and wires can adversely affect the performance of the sensor hence more thorough insulation and protection should be considered in any future work.

4. The effect of shear on the sensor should be considered in future analysis in order to determine the roughness and slip of tissues from the endoscopic grasper.
5. The addressed theoretical and experimental analysis considered a perpendicular loading on the sensor surface but, in reality, a different loading distribution with different angles could be applied on the sensor. For that, further analysis on different loading conditions is required.
6. One of the important issues is the study of contacting tissue-to-sensor interactions. Interaction of the sensor teeth with the contacting tissue at a different tooth-side inclined angle ( $54.74^\circ$  for this prototype) is important for any further studies to optimize the tooth shape for best grasping and gentle lifting. Moreover, study is required on the effect of friction between the contacting tissue and sensor surface. In addition, clinically, the associated tissue is viscoelastic instead of elastic, so analysis considering a viscoelastic contacting tissues is another proposed future work.
7. The designed sensor is able to detect the dynamic load because of the nature of piezoelectric materials. To have the ability of static loading detection, a simple thin aluminum layer could be deposited on the Plexiglas substrate and added to the sensor assembly to form capacitors. With such formed capacitors, the static loading can be detected in addition to the dynamic loading which is detected by the PVDF sensing elements.
8. For best results, the proposed sensor has to be optimized for a specific surgical procedure with a given range of loading and a given range of associated organ softness. Obviously, a wider range of associated loading and tissue stiffness lead

to less resolution and reduced sensitivity. Therefore, in order to achieve maximum sensitivity and optimum resolution, the range of loading and stiffness for the proposed sensor is necessarily limited.

9. After developing, microfabrication, assembling and integration with the surgical tools, the sensor could finally be clinically tested on animal tissues by a specialist surgeon.

## BIBLIOGRAPHY

1. Dargahi J, and Najarian S, "Human tactile perception as a standard for artificial tactile sensing—a review", *International Journal of Medical Robotics and Computer Assisted Surgery*, Vol. 1, No. 1, pp. 23–35, 2004.
2. Howe R., Peine W., Kontarinis D., and Son J., "Remote Palpation Technology for Surgical Applications", *IEEE Engineering in Medicine and Biology Magazine*, Vol.14, No. 3, pp. 318-323, 1995.
3. Tendick F., Sastry S.S., Fearing R.S. and Cohn M., "Applications of micromechatronics in minimal invasive surgery," *IEEE Transaction Mechatronics.*, Vol. 3, pp. 34-42, Mar. 1998.
4. Howe R., and Matsuoka Y., "Robotics for Surgery", *Annual Review of Biomedical Engineering*, Vol. 1, pp. 211-240, 1999.
5. Carrozza M., Dario P., and Jay L., "Micromechatronics in surgery", *Transactions of the Institute of Measurement and Control*, Vol. 25, pp. 309 – 327, 2003.
6. Picetti G., "Basic Introduction to Minimally Invasive spine Surgery", <http://www.spineuniverse.com/displayarticle.php/article240.html>, Retrieved in August 2007.
7. [http://iregt1.iai.fzk.de/KISMET/kis\\_apps\\_med.html](http://iregt1.iai.fzk.de/KISMET/kis_apps_med.html), Retrieved in July 2007.
8. Qasaimeh M.A., Stiharu I., and Dargahi J., "Design and analysis of a micromachined tactile sensor for Minimally Invasive Surgery", *International Conference on Dynamics, Instrumentation and Control*, Queretaro-Mexico, August 13-16, 2006.

9. Tholey G., Pillarisetti A., Green W., and Desai J., "Design, Development, and Testing of an Automated Laparoscopic Grasper with 3-D Force Measurement Capability", S. Cotin and D. Metaxas (Eds.): ISMS 2004, LNCS 3078, pp. 38–48, 2004.
10. Qasaimeh M.A., Dargahi M., Kahrizi M., and Packirisamy M., "Design and analysis of tactile optical sensor for endovascular surgery", Photonics North 2007 Conference, Ottawa- Canada, June 4-7, 2007.
11. Webster J.G., "Tactile sensors for robotics and medicine", A Wiley-Interscience Publication, New York, 1988.
12. Rebello K., "Applications of MEMS in Surgery", Proceedings of the IEEE, Vol. 92, No. 1, pp. 43-55, 2004.
13. Melzer A., Buess G., and Cuschieri A., "Instruments and Allied Technology for Endoscopic surgery", Operative Manual of Endoscopic surgery 2, Springer-Verlag, New York, pp. 1-69, 1994.
14. Ottermo M., Stavadahl O., and Johansen T., "Palpation Instrument for Augmented Minimally Invasive Surgery", 2004 IEEE/RSJ International Conference on Intelligent Robots and Systems, Japan, September 28, 2004.
15. Peine W., Son J., and Howe R., "A Palpation System for Artery Localization in Laparoscopic Surgery", First International Symposium on Medical Robotics and Computer-Assisted Surgery, Pittsburgh, Sept. 22-24, 1994.
16. Nahas F., Farah A., and Solia D., "Suspicious Node Found at the Time of Reduction Mammoplasty", Aesthetic Plastic Surgery, Vol.26, pp 54–56, 2002.

17. Kuroda Y., Nakaob M., Kurodac T., Oyamad H., and Komorie M., "Interaction model between elastic objects for haptic feedback considering collisions of soft tissue", *Computer Methods and Programs in Biomedicine*, Vol.80, pp. 216—224, 2005.
18. <http://www.wuimis.wustl.edu/PatientCare/PatientCareOverview.asp>, Retrieved in June 2007.
19. Nagarajan N.B., "Design, Fabrication and testing of a novel micromachined piezoelectric tactile sensor to measure softness of biological tissues", IRIS-Precarn conference, Ottawa, 2004.
20. Dargahi J., and Najarian S. "Analysis of a membrane type polymeric based tactile sensor for biomedical and medical robotic applications" *Journal of Sensors and Material*, Vol. 16, pp. 25-41, 2004.
21. Tai-Ran Hsu, "MEMS and MICROSYSTEMS Design and Manufacture", McGraw-hill, Inc, 2002.
22. <http://optics.org/cws/product/P000000389>, Retrieved in June 2007.
23. <http://radio.weblogs.com/0105910/2004/06/02.html>, Retrieved in June 2007.
24. Golpaygani A., Najarian S., and Emamieh G., "Design and Modeling of a New Tactile Sensor Based on Membrane Deflection", *American Journal of Applied Sciences*, Vol.4, No.10, pp. 813-819, 2007.
25. Liu Ch., "Foundations of MEMS", Upper Saddle River, NJ: Pearson Prentice Hall, c2006.
26. Hanson H., "MEMS — A Small World with Big Opportunities", <http://www.swri.org/3pubs/ttoday/Winter04/MEMS.htm>, 2004.

27. [http://www.ee.byu.edu/cleanroom/EW\\_orientation.phtml](http://www.ee.byu.edu/cleanroom/EW_orientation.phtml), Retrieved in April 2007.
28. Hsu T.R., "MEMS & Microsystems: design and manufacture", Boston: McGraw-Hill, c2002.
29. Madou M., "Fundamentals of microfabrication: the science of miniaturization", Boca Raton, FL: CRC Press, 2002.
30. Moseley P.T., and Crocker A.J., "Sensor materials", Bristol; Philadelphia: Institute of Physics Pub., c1996.
31. Crowder R.M., "Sensors: Touch, force, and torque", Handbook of Industrial Automation, New York, NY, Marcel Dekker, pp. 377–392, 2000.
32. Beeby S., Ensel G., and Kraft M., "MEMS Mechanical Sensors", Artech House Publishers, May 2004.
33. Window A.L. and Holister G.S., "Strain gauge technology", London: Applied Science Publishers, c1982.
34. <http://www.sensorland.com/HowPage002.html>, Retrieved in September 2007.
35. Morris A., "Measurement and instrumentation principles", Oxford, England: Butterworth-Heinemann, 2001.
36. Northrop R., "Introduction to instrumentation and measurements", Boca Raton, FL: CRC Press, 1997.
37. Uchino K., and Giniewicz J., "Micromechatronics", New York: Marcel Dekker, c2003.

38. Bicchi A., Canepa G., DeRossi D., Iaconi P., and Scilingo E.P., "A sensorized minimally invasive surgery tool for detecting tissutal elastic properties", IEEE International Conference on Robotics and Automation, Minneapolis, MN, pp. 884–888, 22–28 April 1996.
39. Cohn M.B., Crawford L.S. and Wendlandt J.M., "Surgical application of Milli-Robots", Journal of Robotics Systems, Vol. 6, pp. 401–416, 1995.
40. Fischer H., Heilig R., Trapp R., and Brhel K., "Tactile optical sensor for use in minimally invasive surgery", Langenbecks Archiv Fur Chirurgie, pp. 1290, 1996.
41. Josivaldo G.S., Carvalho A.A. and Silva D.D., "A strain gauge tactile sensor for finger mounted applications", IEEE Transaction on Instrumentation and Measurement, Vol.51, No.1, February 2002.
42. Dargahi J., "A three sensing element piezoelectric tactile sensor for robotic and prosthetic applications", J. Sensors Actuators A Phys, vol. 80, pp.23-30, 2004.
43. Gray BL, and Fearing RS., "A surface micromachined microtactile sensor array", IEEE Int. Conf. on Robotics and Automation, Minneapolis, Mn, 22–28 April 1996. IEEE, Robot and Automat Soc, 1996. pp. 1–6.
44. Metha M., "A Micromachined Capacitive Pressure Sensor for Use in Endoscopic Surgery", M.S.c thesis, School of Engineering Science, Simon Fraser University, BC, Canada, 1996.
45. Dargahi J., Parameswaran M., and Payandeh S.M., "A micromachined piezoelectric tactile sensor for an endoscopic grasper-theory, fabrication and

- experiments”, *Journal of Micro-Electro-Mechanical Systems*, Vol. 9, Issue 3, pp.329-335, Sep 2000.
46. Reston R. R., and Kolesar E. S., “Robotic tactile sensory array fabricated from a piezoelectric polyvinylidene fluoride film”, *Proc. IEE NAECON*, Vol. 3, pp. 1139-44, 1990.
  47. Beebe D., Denton D., Radwin R., and Webster J., “A silicon-based tactile sensor for finger-mounted applications,” *IEEE Transaction of Biomedical Engineering*, Vol. 45, pp. 151-159, 1998.
  48. Narayanan N., Bonakdar A., Dargahi J., Packirisamy M., and Bhat R., "Design and analysis of a micromachined piezoelectric sensor for measuring the viscoelastic properties of tissues in minimally invasive surgery", *Journal of Smart Materials and Structures*, Vol. 15, pp 1684–1690, 2006.
  49. Dizaji M., and Dizaji R. M., “Detection of internal displacement of tissues in ultrasound images using image registration technique”, *IEEE CCECE*, Canadian conference, 2002.
  50. Obana F.Y., Carvalho A.A., and Silva G.J.,”A Semiconductor strain gauge tactile transducer”, *IEEE Instrumentation and Measurement technology Conf*, Budapest, Hungary, pp.429-432, May 21-23, 2001.
  51. Shinoda H., and Ando S., “A tactile sensor with 5-D deformation sensing element” *IEEE International Conference on Robotics and Automation*, Minneapolis, MN, pp. 7–12, 22–28 Apr 1996.

52. Ohka M., Mitsuya Y., Takeuchi S., Kamaekawa O., and Ishihara H., "A 3-axis optical tactile sensor—(FEM contact analysis and sensing experiments using a large-sized tactile sensor)", IEEE International Conference on Robotics and Automation, Nagoya, Japan, pp. 817–824, 21–27 May, 1995.
53. Sokhanvar S., Packirisamy M., and Dargahi J., "A multifunctional PVDF-based tactile sensor for minimally invasive surgery", Journal of Smart Materials and Structures, Vol. 16, pp 989–998, 2007.
54. Sokhanvar S., Packirisamy M., and Dargahi J., " Tactile sensor acts as a human finger in minimally invasive surgery", PhysOrg.com, June 2007.
55. Howe, R. D., "Tactile sensing and control of robotic manipulation", Journal of Advanced Robotics, Vol.8, No. 3, pp. 245-261, 1994.
56. Fearing, R. S., "Tactile sensing mechanisms", International Journal of Robotics Research, Vol.9, No. 3, pp. 3-23, 1990.
57. Faraz, S. Payandeh, and A. Salvarinov, "Design of haptic interface through stiffness modulation for endosurgery: Theory and experiments," IEEE International Conf. Robotics and Automation, Leuven, Belgium, May 1998.
58. Petter E., Biehl M., and Meyer J., "Vibrotactile palpation instrument for use in Minimal invasive surgery", Engineering in Medicine and Biology society, Bridging Disciplines for Biomedicine. Proc. of the 18<sup>th</sup> Annual International Conf. of IEEE, 1996.

59. Ryan, A., Beasley, T., and Robert, D., "Tactile Tracking of Arteries in Robotic Surgery" International Conference on Robotic & Automation, proc. of IEEE. Washington, DC, May2002.
60. Youngping Z., Arthur F., and Mak T., "Effective Elastic properties for Lower Limb Soft Tissues from Manual Indentation Experiment", IEEE Transactions on rehabilitation Engineering, Vol. 7, No. 3, September 1999.
61. Dargahi J., Najarian S., Ramezanifard R., and Ghomshe F., "Fabrication and Testing of a Medical Surgical Instrument Capable of Detecting Simulated Embedded Lumps", American Journal of Applied Sciences, Vol.4, No.5, pp 957-964, 2007.
62. Maria C. C., Eisinberg A., Menciassi A., Campolo D., Micer S. and Dario P., "Towards a force-controlled microgripper for assembling biomedical microdevices", Journal of Micromechanics and Microengineering, Vol. 10, pp. 271-276, 2000.
63. Atkinson G.M., Pearson R.E., Ounaies Z., Park C., Harrison J.S., and Midkiff J.A., "Piezoelectric polyimide tactile sensors", Proceedings of the 15th Biennial University/Government/Industry Microelectronics Symposium, pp. 308-311, 2003.
64. Mei T., Li W. J., Ge Y., Chen Y., Ni L. and Chan M. H., "An integrated MEMS three-dimensional tactile sensor with large force range" Journal of Sensors and Actuator A, Vol. 80, pp. 155-162, 2000.

65. Sugiyama S., Kawahata K., Yoneda M., and Igarashi I., "Tactile image detection using a 1K-element silicon pressure sensor array" *Journal of Sensors and Actuators A*, Vol. 22, pp. 397-400, 1989.
66. Beebe D. J., Hsiesh A. S., Denton D., and Radwin G., "A Silicon force sensor for robotics medicine", *Sensors and Actuator A*, Vol. 50, pp. 55-56, 1995.
67. Gray B. L., and Fearing R. S., "A Surface micromachined microtactile sensor array", *Proc.1996 IEEE Int. Conf. On Robotics and Automation*, pp 1-6, 1996.
68. Leineweber M., Pelz G., Schmidt M., Kappert H., and Zimmer, G., "New Tactile Sensor chip with silicone rubber cover", *Journal of Sensors and Actuators A*, Vol. 84, pp. 36-45, 2000.
69. Kolesar E. S., and Dyson C. S., "Object imaging with a piezoelectric robotic tactile sensor", *Journal of Micro-Electro-Mechanical Systems.*, Vol. 4, pp. 87-96, 1995.
70. Kim S.H., Engel J., Liu Ch., and Jones D., "Texture classification using a polymer-based MEMS tactile sensor", *Journal of Micromechanics and Microengineering*, Vol. 15, pp 912-920, 2005.
71. Shinoda H., and Ando S., "Ultrasonic emission tactile sensor for contact localization and characterization", *IEEE International conference on Robotic and Automation*, proc. 1994.
72. Lord Industrial Automation, "Tactile Sensing System", ser. Lord Series 210 Covy, NC, 1987.

73. Suzuki K., Najafi K., and Wise K. D., "A 1024-element high-performance silicon tactile imager", IEEE Trans. Electron Devices, Vol. 37, pp. 1852-1859, 1990.
74. Samaun., Wise K. D, and Angell J. B., "An IC piezoresistive pressure sensor for biomedical instrumentation", IEEE Transaction of Biomedical Engineering, Vol. BME-20, pp. 101-109, 1973.
75. Lee Y. S., and Wise K. D., "A batch-fabricated silicon capacitive pressure transducer with low temperature sensitivity", IEEE Trans. Electron Devices, Vol. ED-29, pp. 42-48, 1982.
76. Tanigawa H., Ishihara T., Hirata M., and Suzuki K., "MOS integrated silicon pressure sensor", IEEE Trans. Electron Devices, Vol. ED-32, pp. 1191-1195, 1985.
77. Hosseini M., Najarian S., Motaghinasab S., and Dargahi J., "Detection of tumors using a computational tactile sensing approach", International Journal of Medical Robotics and Computer Assisted Surgery, Vol.1, No.2, pp. 333–340, 2006.
78. Good Fellow Corporation, US, A Pennsylvania Corporation, Materials Properties, <http://www.goodfellow.com/csp/active/gfHome.csp>, retrieved in March 2006.
79. Beer F., Johnston E., and DeWolf J., "Mechanics of materials", Boston: McGraw-Hill Higher Education, c2006.
80. ANSYS Inc., "ANSYS Basic Analysis Guide, ANSYS Release 10.0", August 2005.

81. ANSYS Inc., "ANSYS Release 8.0 Documentation", <http://www1.ansys.com/customer/content/documentation/80/ansys/index.html>, retrieved in January 2007.
82. S. Sokhanvar, "Micromachined Multifunctional Polyvinylidene Fluoride Tactile Sensor for Minimally Invasive Surgery Graspers", PhD thesis, Mechanical and Industrial Engineering Department, Concordia University, Montreal, Canada, August 2007.
83. ANSYS Inc., "Coupled- Field Analysis Guide, ANSYS Release 10.0", August 2005.
84. S. Naseh, "Experimental investigation of anisotropic etching of silicon in tetramethyl ammonium hydroxide," M.S.thesis, Electrical and Computer Engineering Department, Concordia University, Montreal, Canada, Sept 1995.
85. A. Pandey, L.M. Landsberger, and M. Kahrizi, "Mask-Under-Etch Experiments of Si {110} in TMAH", Proceedings of the 1999 IEEE Canadian Conference on Electrical and Computer Engineering Shaw Conference Center, Edmonton, Alberta, Canada, May 9-12 1999.
86. A. Pandey, L.M. Landsberger, and M. Kahrizi, "Mask-under-etch characterization of Si {110} in TMAH", Canadian Journal of Electrical and Computer Engineering, Vol.25, No.1, pp. 19-24, January 2000.
87. Irina Stateikina, Leslie M. Landsberger, Mojtaba Kahrizi, Nazmul Hoque and Victor Rossokhaty, "Silicon Wet Etch Anisotropy: Analysis of the Impact of

- {111}-, {110}-, {100} - Terrace Widths”, *Sensors and Materials*, Vol. 17, No. 4, pp. 201– 213, 2005.
88. B. Nikpour, L.M. Landsberger, T.J. Hubbard, M. Kahrizi, and A. Iftimie, "Concave corner compensation between vertical (010)-(001) planes anisotropically etched in Si (100)", *Sensors and Actuators A*, Vol. 66, pp. 299-307, 1998.
  89. S. Naseh, L.M. Landsberger, M. Paranjape, and M. Kahrizi, "Experimental investigations of anisotropic etching of Si in tetramethyl ammonium hydroxide", *Canadian Journal of Physics (Suppl.)*, Vol. 74, pp. 79-84, 1996.
  90. Landsberger L., Naseh S., Kahrizi M., and Paranjape M., "On Hillocks Generated During Anisotropic Etching of Si in TMAH", *Journal of Micro-Electro-Mechanical Systems*, Vol. 5, No. 2, pp. 106-116, 1996.
  91. Sonphao W., and Chaisirikul S., "Silicon Anisotropic Etching of TMAH Solution" 2001 IEEE International Symposium on Industrial Electronics, pp. 2049-2052, 2001.
  92. Kirt R. Williams, Kishan Gupta, and Matthew Wasilik, "Etch Rates for Micromachining Processing—Part II", *Journal of Micro-Electro-Mechanical Systems*, Vol. 12, No. 6, 2003.
  93. Cady W.G., "Piezoelectricity", 1<sup>st</sup> ed., McGraw-Hill Inc., New York, 1946.
  94. Toupin R.A., "A Dynamical theory of elastic dielectrics," *International Journal of Engineering Science*, Vol. 1, pp. 101-126, 1963.

95. Toupin R.A., "The Elastic dielectric," *Journal of Rational Mechanical Analysis*, Vol. 5, No. 6, pp. 849-915, June 1956.
96. Peelamedu S., Naganathan G., Barnett, A., and Rao, D. "Finite element approach to model and analyze piezoelectric actuators", *American Institute of Aeronautics and Astronautics (AIAA) Journal*, Feb 1999.
97. Allik H., and Hughes T.J.R., "Finite element method for piezoelectric vibration", *Int. Journal for Numerical Methods in Engineering*, Vol. 2, pp. 151-157, 1970.
98. Mohamed N.S. and Arof A.K., "Investigation of electrical and electromechanical properties of PVDF-based polymer electrolytes", *Journal of Power Sources*, Vol.132, pp.229-234, 2004.
99. Measurement Specialties Inc., "Piezo Film Sensors – Technical Manual", 1999.
100. Measurement Specialties Inc., "Interfacing Piezo Film to Electronics – Application Note", 2006.

## **A1. APPENDIX – 1**

### **PIEZPELECTRIC EFFECT**

Piezoelectric substances are new materials used for sensor and actuators with the help of Micro-Electro-Mechanical Systems (MEMS) technology. When external force is applied to piezoelectric materials it generates charge on the surface, which is proportional to applied mechanical stress. The converse effect is also there, applied voltage generates deformation in the materials. Similarly ferroelectric type of material is one which exhibits a spontaneous polarization in one or more direction of the crystal over a definite temperature range. Piezoelectric must not be confused with the Ferro-electricity, which is the property of a spontaneous or induced electric dipole moment. All ferroelectric materials are piezoelectric, but the contrary is not always true. Piezoelectricity relates to the crystalline ionic structure. Ferro-electricity instead relates with electron spin.

A simplified model of piezoelectricity entails the motion of anions (-) and cations (+) moving opposite directions under the influence of an electric field and mechanical force. The force generated by this motion cause lattice deformation for non-Centro symmetric crystals due to presence of both high and low stiffness ionic bonds. As results, all piezoelectric materials are anisotropic, in case of central symmetry; an applied force does not yield an electric polarization. The effect for quartz is shown below in Figure A1.1, positive and negative charges are formed. It is important to remember that the piezoelectric materials are function of the continuously changing mechanical deformation. Therefore dynamic forces are used in practical situations.

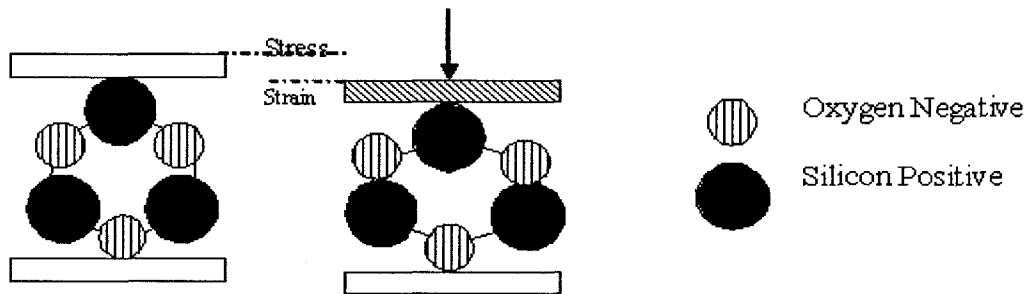


**Figure A1.1 - Piezoelectric in ionic crystals such as quartz, ion position in quartz lattice with and without applied stress**

### **A1.1 Piezoelectric Materials**

The most extensively used natural piezoelectric materials are crystals (quartz and tourmaline). In synthetic piezoelectric, ceramics formed by many tightly compacted monocrystals ( $1\mu$  in size) are most popular. These Ceramics, such as Lead Zirconate titanate (PZT), barium titanate is ferroelectrics. To align the dipoles to monocrystals in same direction, they are subjected to strong electric field during their manufacturing process. The applied electric field to crystal is above the Curie temperature to align the dipoles. Then cool the crystal while maintaining the field. This process makes crystal permanent electric polarized. When electric field is removed, the crystalline cannot reorder in random form because of mechanical stresses accumulated, resulting in permanent electric polarization. The problem with these materials relates to their temperature sensitivity and aging when approaching the Curie temperature.

Polymers such as polyvinylidene fluoride (PVDF) also display piezoelectric properties and have pyroelectric features (change the electrical charge with change in temperature).

PVDF are not central symmetry, so it displays piezoelectric properties. Compared to quartz and ceramics, Piezo-film is more pliant and lighter in weight. In addition to this it is rugged, inert and low cost. Urethane and epoxy adhesive are used for gluing PVDF; the use of epoxy and urethane adhesives depends upon the strength requirement of the structure.

In smart structures, Piezo-ceramics are typically used as actuators. On the other hand; polymeric piezoelectric materials are typically used as tactile sensor, temperature and strain sensors. It is common practice to embed piezoelectric sensors into prototypes because these sensors can be manufactured with strength and dimensional characteristics that do not degrade the structural integrity of the material from which the prototype device is made. Piezoelectric ultrasonic motors and Piezo-ceramic sensors are currently being built into commercial products such as camera lens drives and automotive engine control systems. In many cases, thin layers of Piezo-ceramic composites are bonded to other structural material surfaces. When thermal effects are generated through either friction or direct exposure to significant temperature gradients, the reliability of the electrode layer in these Piezo-ceramics can completely dominate the performance of the device.

Many efforts have been done for mathematical modeling of piezoelectric phenomenon. Cady [93], gave comprehensive description of development in the theory of piezoelectricity. Toupin [94, 95] involved in development of the governing equation using energy methods and dynamics theory. Tiersten [96], made several approximations and developed linear equation of piezoelectricity using Hamiltonian mechanics and variation techniques. Allik and Hughes [97] developed the general equation of motion for

piezoelectric materials in a matrix form. Authors on [96, 97] combined the work together to formulate finite element solution for piezoelectric structure.

Basic Constitutive Equations [96] are expressed in matrix notation as

$$\begin{aligned} [T] &= [c]\{S\} - [e]^T \{E\} \\ [D] &= [e]\{S\} + [\varepsilon]\{E\} \end{aligned} \tag{A1.1}$$

The first and second equation represents structural and electrical constitutive of piezoelectric material, respectively. Where as the entire matrix are given as

$\{T\}$  = Stress vector (N/m<sup>2</sup>)

$\{D\}$  = Electric flux density (C/m<sup>2</sup>)

$\{E\}$  = Electric Field Vector (V/m)

$\{S\}$  = Strain vector (dimensionless)

$[c]$  = Elasticity Matrix (N/m<sup>2</sup>)

$[e]$  = Piezoelectric matrix at constant stress (C/m<sup>2</sup>)

$[\varepsilon]$  = Dielectric Matrix

## A1.2 Piezoelectric Coefficients

Most of piezoelectric coefficients have double subscript that links electrical and mechanical quantities. The first subscript gives the direction of the electrical field associated with voltage applied and second subscript gives the direction of the mechanical stress or strain.

### A1.2.1 D – Coefficients

The piezoelectric constant relating the mechanical strain produced by an applied electric field are termed the strain constant or 'd' coefficients or piezoelectric strain matrix. Conversely the coefficient may be viewed as relating the charge collected on the electrodes, to the applied mechanical stress. The unit of 'd' coefficient is C/N.

$$d = \text{charge density/applied mechanical stress.}$$

### A1.2.2 E – Coefficients

The piezoelectric constant relating the electrical field produced by applied mechanical stress at constant strain is known as stress constant or 'e' coefficient or piezoelectric stress matrix. The unit of 'e' coefficient is C/m<sup>2</sup>. There is relationship between [e] and [d] matrix and it is given as

$$[e] = [d] [c] \tag{A1.2}$$

For 3D analysis Z-axis are considered as polarized axis and size of array [e] and [d] is 6x3. If we are considering the 2D analysis then we use Y- axis as polarized axis and order of array [e] and [d] is 4x2. Similarly for [ε] matrix size are different for 3x3 and 2x2 for 3D and 2D model respectively.

### A1.2.3 G – Coefficients

The piezoelectric constants relating the electric field produced by a mechanical stress are termed the voltage constants, or the "g" coefficients. The units are then expressed as volts/meter per Newton/square meter.

$$g = \frac{\text{ElectricField}}{\text{Applied Mechanical Stress}} \quad (\text{A1.3})$$

High  $g_{ij}$  constants favor large voltage output, and are sought after for sensors. The relationship between the [d] and [g] matrix is given as

$$[d] = [K]^T[g] \quad (\text{A1.4})$$

#### A1.2.4 Dielectric Constants

The relative dielectric constant is ratio of the permittivity of material,  $\epsilon$ , to the permittivity of free space,  $\epsilon_0$ , in the unconstrained condition. ( $\epsilon_0 = 8.9 \times 10^{-12}$  farad/meter).

$$K = \frac{\text{Permittivity of Material}}{\text{Permittivity of Free Space}} = \frac{\epsilon}{\epsilon_0} \quad (\text{A1.5})$$

#### A1.2.5 Capacitance

Capacitance is a quantity dependent on the type of materials and its dimensions. Unit of capacitance is Farad. Capacitance is expressed by following formula:

$$C = \frac{K\epsilon_0 A}{t} \quad (\text{A1.6})$$

Whereas “A” area of electrode, “t” is gap between the electrodes.

#### A1.2.6 Young’s Modulus

Young’s Modulus is ratio of stress (force per unit area) to strain (change in length per unit length). Unit of young Modulus is  $\text{N/m}^2$ .

$$Y = \frac{\text{Stress}}{\text{Strain}} \quad (\text{A1.7})$$

### A1.2.7 Density

The ratio of the mass to volume in the material, expresses in Kg/m<sup>3</sup>

$$\rho = \frac{\text{mass}}{\text{volume}} \quad (\text{A1.8})$$

### A1.2.8 Curie temperature

The Temperature at which the crystal structure changes from a non-symmetrical (piezoelectric) to a symmetrical (non- Piezoelectric) form, expresses in degrees Celsius.

### A1.2.9 Pyroelectricity

Piezoelectric materials are also Pyroelectric materials. They produce electric charge as they undergo a temperature change. When their temperature is increased, a voltage develops having the same orientation as polarization voltage. The change in electric field due to a temperature change is given as.

$$E_{\text{pyro}} = \frac{\alpha \Delta T}{K_3 \epsilon_0} \quad (\text{A1.9})$$

Whereas, E is the induced electrical field (volts/meter),  $\alpha$  is the pyroelectric coefficient in Coulomb/Cm<sup>2</sup>,  $\Delta T$  is temperature difference in C<sup>0</sup>.

### A1.3 Analytical Approach

The analytical method is demonstrated in this section. In this section relation between the voltage generation and force applied are discussed. The force  $F$  is applied to the rectangular piezoelectric plate of size  $L \times T \times W$ . The Figure A1.2 demonstrates the working of the rectangular piezoelectric plate. The voltage and charge develop by this force is given as

$$Q = F d_{33} \quad (A1.10)$$

$$\frac{V}{T} = \frac{F g_{33}}{LW} \quad (A1.11)$$

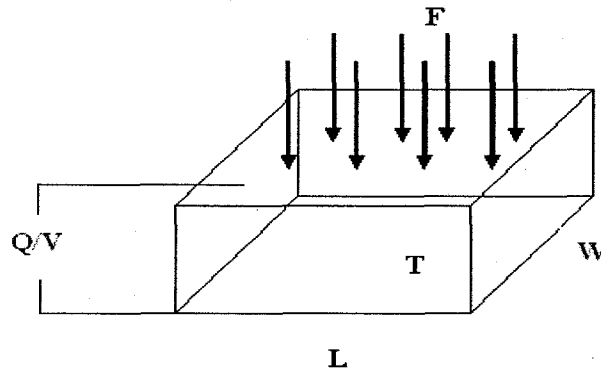


Figure A1.2 - Voltage generation by piezoelectric substance

For ordinary solids, a stress  $\sigma$  merely causes a proportional strain  $\epsilon$ , related by an elastic modulus,  $\sigma = \epsilon E$ . Piezoelectricity is the additional creation of an electric charge by the applied stress. This is the direct piezoelectric effect. The charge is proportional to the force, and it is therefore of opposite sign for compression and tension. In terms of dielectric displacement  $D$  (charge  $Q$  per unit area) and stress  $\sigma$ , we may write:

$$D = Q/A = d \sigma \text{ (d expressed in coulombs/Newton)} \quad (A1.12)$$

There is also a converse effect. An applied electric field produces a proportional strain  $\epsilon$ , expansion or contraction depending on polarity.

$$\epsilon = d V \text{ (d expressed in meters/Volt)} \quad (A1.13)$$

For both effects, the proportionality constant is the piezoelectric constant  $d$ , which is numerically identical for both direct and converse effects.

$$d = D/\sigma = \epsilon/V \quad (A1.14)$$

High  $d$  constant is desirable for materials intended to develop motion or vibration, such as sonar or ultrasonic cleaner transducers. Another frequently used piezoelectric constant is  $g$  which gives the voltage produced by a stress. Its usual units are meter volts/Newton, simplified from (Volt/meter) / (Newton/square meter).

The  $g$  constant is related to the  $d$  constant by the permittivity  $g = d/\epsilon' = d/K\epsilon_0$  ( $K = \epsilon'/\epsilon_0$ ), the relative dielectric constant, is the ratio between the charge stored on a electroded slab of material brought to a given voltage and the charge stored on a set of identical electrodes separated by vacuum. It is usually referred as dielectric constant, and is dimensionless)

High  $g$  constant is desirable in materials intended to generate voltages in response to a mechanical stress, as in a phonograph pickup. On the other hand we have from hook's law:  $\sigma = \epsilon E$  then we can write:  $\sigma = d V E$ , so  $V = \sigma /d E$  where  $E$  is the Young's modulus of the piezoelectric material. The piezoelectric coefficient  $d$  depends on piezoelectric crystals will be given by the manufacturer.

## A2. APPENDIX – 2

### LIST AND SPECIFICATIONS OF THE EQUIPMENT USED FOR RUNNING THE EXPERIMENTS

- Dual Mode Power Amplifier: Model 504E, KISTLER Instrument Corporation.

Useful Amplifier factor: 1V/lbf.

- Signal Generator: Agilent 33220A, 20MHz Function/Arbitrary Waveform Generator
- V203 Vibrator: made by Ling Dynamic Systems LTD.

The main specifications are as the following:

Sine force peak: 17.8N;

Useful frequency Range: 1 ~ 13000Hz;

Velocity sine peak: 1.49 m/s;

Amplifier rating: 0.048kVA;

Displacements pk-pk: 5.0mm.

- Charge Amplifiers: Type 2634.

Amplifier factor: 10mv/lbf

- Oscilloscope: Agilent 54624A Oscilloscope, 100MHz 200MSa/s;

Controller interface: RS-232

- Force Transducer: Type 9712B50, KISTLER Instrument Corp.

The main specifications are as the following:

Sensitivity: 92.9mv/lbf;

Measuring range: 50lbf;

Temperature: -50~120°C.

- Probe: Aluminum bar, connected with force transducer, passing force to sensor.  
Different probes with different head diameters are used, some of them are shown in Figure A2.1.
- The Data Acquisition Card (DAQ): Type NI PCI-6225 from National Instrument Company.
- Personal Computer with installed LabVIEW software (Version 7.1).

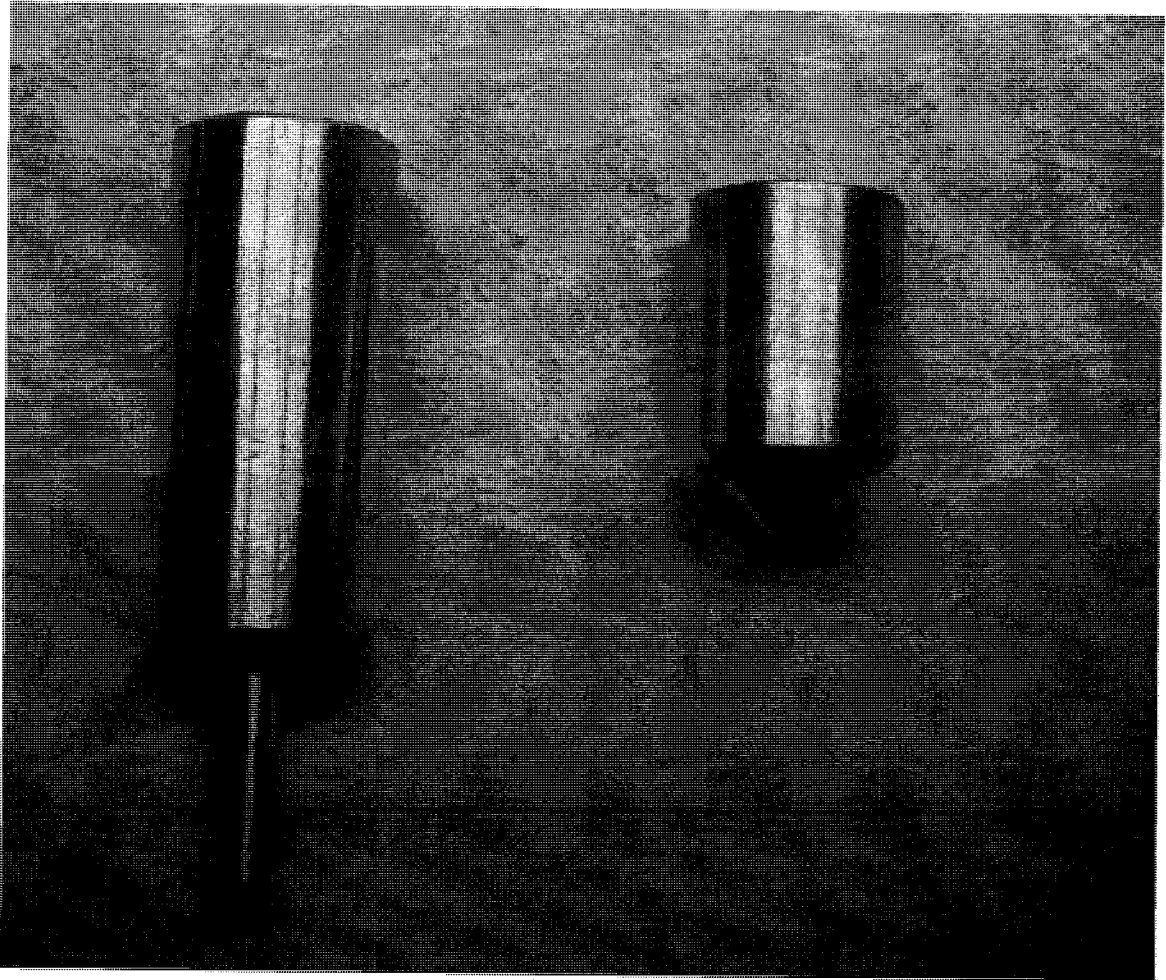


**Figure A2.1 – Some of the used probes in experiments**

## **A3. APPENDIX – 3**

### **EQUIVALENT CIRCUIT OF THE MEASUREMENT SETUP**

The behavior of a piezoelectric film at low frequencies is fairly straightforward to describe in electronic terms. PVDF has a high dielectric constant in contrast to most of the other polymers. PVDF manufacturers typically measure this property at high frequencies, to say not smaller than 1 KHz, and report it in the specifications sheet. For the uniaxial PVDF film used in this study, which was manufactured by the GoodFellow Company of the U.S.A., the value of this property is reported as 11 at a frequency of 1 KHz. Since the excitation frequency of experiments is kept at 5 Hz, it could be suggested that the dielectric constant at this frequency might have a very different value, which translates into a different capacitance value for each sensing element. However, according to some earlier studies, for a pure PVDF film the dielectric constant remains literally constant at a wide range of frequencies [98], even down to 20 Hz.

#### **A3.1 Equivalent Circuit of a Piezo-film**

There are two equally valid models for a piezo film (or each sensing element of the sensor in this sensor). The first one is a “voltage” source in series with a capacitor; the other is a charge generator in parallel with a capacitor. The former is more popular so it will be used in this study to build the electric circuit equivalent of the PVDF film [99, 100].

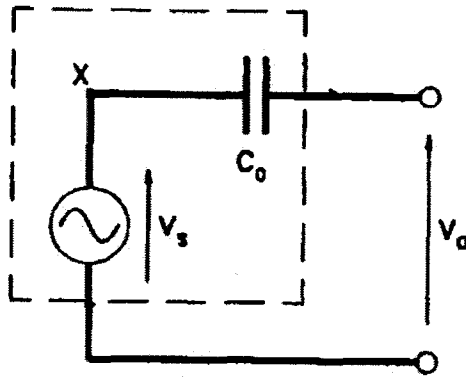


**Figure A3.1 - Piezo-film element as a simple voltage generator**

The capacitance of each sensing element, denoted by  $C_o$ , can be calculated based on the values of its elements. The voltage source amplitude, denoted by  $V_o$ , is equal to the open circuit voltage of a sensing element that can range from micro-volts to a couple of volts, depending on the excitation magnitude. This simplified equivalent circuit is of limited value at very high frequencies such as applications in ultrasound transducers. Nevertheless, for low frequency applications, as in this study, it is suitable enough [99, 100].

### **A3.1.1 Effect of Input Resistance**

The most critical part of an interface circuit is its input resistance (in this case the op-amp buffer or data acquisition card). The input resistance not only affects low frequency measurement but also the amplitude of the output signal. This is referred to as the “loading effect”. The capacitance of each sensing element transforms into impedance, the magnitude of which depends on the frequency of operation and the capacitance measured

at a DC circuit [99, 100]. The combination of all these elements produces a voltage divider as shown in Figure A3.2.

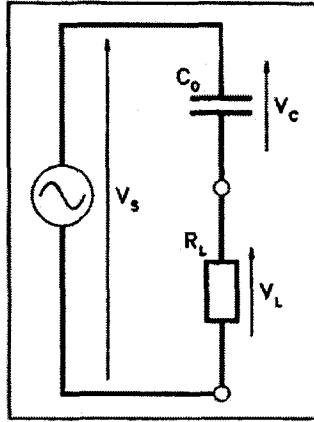


**Figure A3.2 - The measurement circuit modeled as a voltage divider**

$V_C$  is that proportion of the source voltage  $V_S$  which is monitored and measured on the computer. The following set of relations and equations helps in determining its magnitude [99, 100]:

$$C = \epsilon_0 \epsilon_r \frac{A}{d} \tag{A3.1}$$

$$X_C = \frac{1}{2\pi fC} \tag{A3.2}$$

$$V_C = \frac{X_C \cdot V_S}{\sqrt{X_C^2 + R_L^2}} = \frac{X_C \cdot V_S}{X_C \sqrt{1 + \left(\frac{R_L}{X_C}\right)^2}} = \frac{1}{\sqrt{1 + \left(\frac{R_L}{X_C}\right)^2}} V_S \tag{A3.3}$$

### A3.1.2 Effect of Input Capacitance

In addition to input resistance, the input capacitance of an interface circuit can also influence the output electrical charge of sensing elements [99, 100]. This is shown in Figure A3.3.

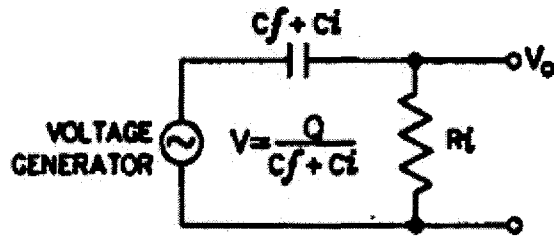


**Figure A3.3 - Equivalent circuit of a sensing element considering the input capacitance**

The input capacitance  $C_i$  can be contributed, for instance, by an oscilloscope or a long cable. Since none of these elements exist in the measurement setup, the input capacitance can be ignored. So the circuit shown in Figure A3.2 suffices for the purposes of this study [99, 100].

### **A3.1.3 Equivalent Circuit of the Measurement Setup**

Referring to Figure A3.3, the impedance of each sensing element is computed as:

$$X_c = \frac{1}{2\pi fC} = \frac{1}{2\pi(20 \text{ Hz})(35.062 \text{ pF})} = 302.6176 \text{ M}\Omega$$

Unfortunately the precise value of  $R_L$  is unavailable. However, it is estimated to be around 500 M $\Omega$ . Based on this value, the measured voltage  $V_c$  and the developed voltage

$V_s$  are related to each other as:

$$V_c = \frac{1}{\sqrt{1 + \left(\frac{R_L}{X_c}\right)^2}} V_s = \frac{1}{\sqrt{1 + \left(\frac{500}{302.618}\right)^2}} = 0.518 V_s$$

Here  $R_L$  is the total resistance of the circuit that includes the op-amp buffer, other connections such as solder, copper electrodes and photo resist material in between the faces of each sensing element. It is interesting to observe how the elements of the electronic circuit can attenuate the outputs of the sensing elements. Even if the  $R_L$  is taken as being equivalent to  $X_C$ , there will be almost 30% drop in voltage at each sensing element. This equivalent circuit is for each of the four sensing elements so there are four circuits in the measurement setup of which each has about the same elements and almost the same amount of parameters [99, 100].